



HAL
open science

Characterization and optimization of the Evanescent Wave Coronagraph

Mary Angelie Alagao

► **To cite this version:**

Mary Angelie Alagao. Characterization and optimization of the Evanescent Wave Coronagraph. Optics / Photonics. Université Jean Monnet - Saint-Etienne; Chiang Mai University, 2023. English. NNT : 2023STET0060 . tel-04538434

HAL Id: tel-04538434

<https://theses.hal.science/tel-04538434>

Submitted on 9 Apr 2024

HAL is a multi-disciplinary open access archive for the deposit and dissemination of scientific research documents, whether they are published or not. The documents may come from teaching and research institutions in France or abroad, or from public or private research centers.

L'archive ouverte pluridisciplinaire **HAL**, est destinée au dépôt et à la diffusion de documents scientifiques de niveau recherche, publiés ou non, émanant des établissements d'enseignement et de recherche français ou étrangers, des laboratoires publics ou privés.



N° d'ordre NNT: 2023STET060

**THÈSE de DOCTORAT
DE L'UNIVERSITÉ DE JEAN MONNET SAINT-ÉTIENNE**

Membre l'Université de Lyon

**Ecole Doctorale N°488
Sciences Ingénierie, Santé**

**Spécialité/ discipline de doctorat : Optique, Photonique,
Hyperfréquences**

Soutenue publiquement/à huis clos le 18/12/2023, par :

Mary Angelie Alagao

**Characterization and Optimization of the
Evanescent Wave Coronagraph**

Devant le jury composé de :

Wiphu Rujopakarn Deputy Director, National Astronomical Research Institute of Thailand	Président
Marc Ollivier Astronome HDR, Directeur de l'Institut d'Astrophysique Spatiale	Rapporteur
Siramas Komojinda Assistant Professor, Chairman of Astronomy/Chiang Mai University	Rapportrice
Supachai Awiphan Acting Director, Center for Optics and Photonics/NARIT	Examineur
Thierry Lépine Associate Professor, Institute d'Optique Graduate School	Directeur de thèse
Suwicha Wannawichian Assistant Professor, Chiang Mai University	Co-Directrice de thèse
Yves Rabbia Astronome Honoraire, Observatoire de la Côte d'Azur, Université de Nice	Invité
Michel Tallon Chargé de recherche, Centre de Recherche Astrophysique de Lyon	Invité

To you who believed I will make it this far.

ACKNOWLEDGEMENT

This milestone wouldn't have been possible without the help and support of the many amazing people I met on this journey.

My mentors

This journey started with *Christophe and Thierry* believing in me. Through them, I had the privilege of learning more about Technical Optics and accessing the resources and education I could only dream of.

My perspective of how difficult subjects are taught changed when I started learning from *Yves Rabbia*. His view graphs taught me how to learn Fourier Optics visually, which is more suited to my kind of learning. Yves put a lot of effort into giving detailed comments that allowed me to see the gaps in my knowledge.

I learned to be more open to others when my CMU supervisor, *Suwicha*, insisted on meeting me weekly whether I had any results to show or not. I appreciate her patience and understanding of my circumstances, especially when I was struggling.

Members of the Jury

My PhD journey has been filled with so many twists and turns that I wasn't even sure if I would make it at some point. I am thankful to the members of the jury: Wiphu, Marc, Siramas, Supachai, Yves, Michel, Thierry, and Suwicha, who braved several administrative issues so I could eventually earn this degree. I also appreciate the generous comments and questions that pushed me to learn more.

EvWaCo Team

I have had the opportunity to work with amazing people in the EvWaCo team who continue to inspire me and challenge me simultaneously.

First members of the EvWaCo team: Adithep, Anthony, Boris, Matthew, and Puttiwat

I thank their patience for simplifying concepts in their field so I could understand better. I would like to especially mention Anthony, who generously spent hours discussing with me concepts I need help visualizing.

Current members of the EvWaCo team: Pimnipa, Milk, Fern, and Cheer
Thank you for the honor of serving as your team manager. I learned a lot from working with you.

Our collaborators from CRAL: Michel, Eric, and Maud I always feel a warm welcome every time I visit them in Lyon, and I learned a lot from their different approach of solving problems.

NARIT

I am very fortunate to work at NARIT whose vision aligns with my advocacy of making science available to everyone. It has given me many opportunities for growth, allowing me to be closer to Astronomy than I could ever imagine. I would like to thank *Saran and Boonrucksar*, who have supported me since the beginning. I am very grateful to *Supachai* for providing me with the support I needed during his reign as our team leader and acting Director. Although most of my time is spent working in the lab, I find it relaxing to spend time with the Center for Optics and Photonics team, like my second family. I would like to express my gratitude to Toon, the other Ph.D. warrior, who helped me a lot in debugging my Latex codes and for being my go-to person when I have questions about optical design. I also would like to thank the administrative and technical staff at NARIT for their kindness, especially those at the Mechatronics department, who made me feel like part of their team when I was new at NARIT.

Family and friends

The journey has been long and very difficult. I am thankful to my neurologist, Dr. Sasiwimol, and her assistant nurse, Ae, who worked with me in coming up with a strategy to finish this journey despite my chronic migraines. Finally, I don't think I would have made it through without the strong support system provided by *my family in the Philippines and friends here and abroad* throughout all these years. Thank you for being my refuge, especially during the tough times.

Mary Angelie Alagao

Thesis Title	Characterization and Optimization of the Evanescent Wave Coronagraph	
Author	Mary Angelie Alagao	
Degree	Doctor of Philosophy (Optics)	
Advisory Committee	Assoc. Prof. Thierry Lepine	Advisor
	Asst. Prof. Suwicha Wannawichian	Co-advisor
	Asst. Prof. Siramas Komojinda	Co-advisor

Abstract

Direct imaging of exoplanets remains challenging due to its high contrast between planet and star brightness and the very close angular separation between the star and the planet. It requires suppressing the blinding glare from the star and ensuring that the planet's faint light is not buried deep in various noises. Successful detection depends on the technological readiness and maturity of techniques and algorithms employed while considering the significant trade-offs on raw contrast, inner working angle, and throughput. One of its key components is the use of coronagraphs – instruments with the sole purpose of blocking/reducing the light from the star. This work presents a new type of Lyot coronagraph that relies on the frustrated total internal reflection (FTIR) principle to suppress the starlight. This coronagraph is aptly called the Evanescent Wave Coronagraph (EvWaCo) owing to its nature that its focal plane mask, comprising of a lens and a prism, reflects the off-axis source (planet) and transmits the on-axis source (star) by capturing evanescent waves. This thesis aims to provide the reader with the groundwork that highlights EvWaCo's three main advantages: i) the mask is inherently achromatic, ii) the size of the mask is adjustable by changing the pressure between the lens and the prism, and iii) both the stellar light and the planet light can be collected simultaneously for low-order wavefront sensing, and proper stellar light centering. The performance of EvWaCo is assessed through experiments in a laboratory and then compared to numerical simulations.

The experimental results show a raw contrast equal to a few 10^{-4} at $3 \lambda/D$ over the full I-band ($\lambda_c = 800 \text{ nm}$, $\Delta\lambda/\lambda \approx 20\%$) and at $4 \lambda/D$ over the full R-band ($\lambda_c = 650 \text{ nm}$, $\Delta\lambda/\lambda \approx 23\%$). The simulations confirm the achromatic rejection capability of EvWaCo as it showed a raw contrast of 10^{-4} at the same radial distance over both bandpasses. This thesis concludes with the status of its testbed and future perspectives.

CONTENTS

	Page
Acknowledgement	3
Abstract	6
List of Tables	10
List of Figures	16
Chapter 1 Introduction	2
1.1 The Challenges of Direct Imaging	6
1.2 Key Drivers for a Successful Direct Imaging	8
1.3 Current Status and Future of High Contrast Imaging Instrumentation	12
1.4 Summary	15
1.5 About this Research	15
Chapter 2 Coronagraphs	17
2.1 Various Coronagraph Designs	19
2.2 State-of-the-Art	23
2.3 Technological Gaps in Coronagraphy	26
2.4 Summary	26
Chapter 3 The Evanescent Wave Coronagraph	28
3.1 Frustrated Total Internal Reflection	29
3.2 The Focal Plane Mask	33
3.3 Early Beginnings	34
3.4 Context of the PhD Research	37
3.5 Scope of this PhD Research	38

Chapter 4	Experimental Validation and Characterization	40
4.1	The Setup	40
4.2	Raw contrast performance	47
4.3	Companion Detection	52
4.4	Repeatability and stability	52
4.5	Sensitivity Measurements	58
4.6	Raw Contrast at different mask pressure	63
4.7	Summary	67
Chapter 5	Optimization	68
5.1	Improving the estimation of the air gap	68
5.2	Optimizing the performance using a Gaussian apodizer	70
5.3	Summary	75
Chapter 6	Discussion	78
6.1	Limitations of the proposed approach	78
6.2	Considerations for the focal plane mask design	83
6.3	Combining the coronagraph and wavefront control - setup upgrade	84
6.4	Summary	90
Chapter 7	Conclusion and Perspectives	93
7.1	Comparison to existing coronagraphs	95
7.2	Adaptation to big telescopes	96
7.3	Wavefront control and coupling to high-resolution spectrograph	97
Bibliography		100
Appendices		108
Appendix A	Aligning the EvWaCo	108
Appendix B	Data Acquisition Procedure	114
Appendix C	Numerical Modelling in Broadband Light	116
Curriculum Vitae		118

LIST OF TABLES

		Page
Table 3.1	Optical Specifications of the EvWaCo Prototype.	39
Table 4.1	Parameters in the EvWaCo Testbed.	42
Table 6.1	Statistics to Test the Linearity of the Mask and PSF FWHM at different angles of incidence: $f(x) = p_1x + p_2$ for an air gap at $d = r^2/2R$	80
Table 6.2	Parameters of the new EvWaCo Testbed	86
Table 6.3	Statistics to Test the Linearity of the Mask and PSF FWHM at different angles of incidence: $f(x) = p_1x + p_2$ for an air gap at $d = \max\left(\sum_{n=0}^3 a_n \left(\frac{x}{x_o}\right)^n, 0\right)$	86

LIST OF FIGURES

	Page
Figure 1.1 Concept of Parsecs	3
Figure 1.2 Illustration of transit and radial velocity	4
Figure 1.3 Exoplanet Detection per year and Mass-Period distribution of the detected exoplanets	4
Figure 1.4 Biosignatures present in the atmosphere	5
Figure 1.5 Image of the star 2MASS1207 and its planet	6
Figure 1.6 Image of the HR8799 planetary system and its four young giant planets	6
Figure 1.7 Image of the Beta Pictoris System	7
Figure 1.8 Our Solar system analog at 10 parsecs	8
Figure 1.9 Reflected planet flux in the visible and the emitted flux in the near-IR	9
Figure 1.10 Coronagraphic image at the Hubble Space Telescope	9
Figure 1.11 Illustration of the principle of nulling interferometry	10
Figure 1.12 Illustration of an External Occulter (Starshade)	11
Figure 1.13 Illustration of a typical adaptive optics system	12
Figure 1.14 Demonstration of the Extreme AO Correction	13
Figure 1.15 Typical coronagraph system for exoplanet detection imaging.	13
Figure 1.16 Four processes involved in successful direct imaging.	13
Figure 1.17 Performance of ground-based and space-based telescopes.	14
Figure 2.1 Light Propagation in a stellar coronagraph.	18
Figure 2.2 Irradiance distributions at the different planes in a typical Lyot coronagraph.	18
Figure 2.3 Example of a shaped pupil	21
Figure 2.4 Point spread function of an azimuthally symmetric generalized prolate spheroidal apodized circular aperture	22

Figure 2.5	Illustration of the band-limited mask.	22
Figure 2.6	Basic principle of an achromatic interfero-coronagraph (left) and phase mask coronagraph (right)	23
Figure 2.7	Light propagation inside three different coronagraph designs	24
Figure 3.1	EvWaCo Focal Plane Mask	28
Figure 3.2	Reflection and transmission at a thin, homogeneous film	29
Figure 3.3	Newton's rings setup in reflected light	34
Figure 3.4	Beam footprint at the focal plane mask plane	35
Figure 3.5	Optical setup used to demonstrate the preliminary studies in EvWaCo (Buisset et al., 2017)	36
Figure 3.6	Conceptual design of the EvWaCo coronagraphic mask.	37
Figure 3.7	First version of the EvWaCo Prototype Design on the Thai National Telescope installed vertically	38
Figure 4.1	Schematic diagram of the EvWaCo testbed used to characterize the coronagraph performance at small IWA ($\leq 3\lambda/D$).	41
Figure 4.2	Irradiance at the Exit Pupil Plane.	43
Figure 4.3	Schematic diagram of the setup to obtain the flat field (mask) images.	43
Figure 4.4	Flat-field (mask) images showing the mask response to increasing pressure on the prism.	44
Figure 4.5	Reflection profiles of the mask.	44
Figure 4.6	Playing with different polynomials coefficients to approximate the air gap	45
Figure 4.7	Air gap approximation of the current mask	46
Figure 4.8	Comparison between the theoretical and measured mask response along the major axis of the mask (x-axis) and the minor axis (y-axis)	47
Figure 4.9	Experimental and theoretical mask profiles along the x- and the y-axis at different central wavelengths	48
Figure 4.10	Illustration of the raw contrast calculation.	49
Figure 4.11	Normalized irradiance distribution of the on-axis star over the full I-band	50

Figure 4.12 Normalized irradiance distribution of the on-axis star over the full R-band	50
Figure 4.13 Profiles of the spectral flux incident on the detector at $\lambda_c \approx 800$ nm (left) and $\lambda_c \approx 650$ nm (right).	51
Figure 4.14 Calculated raw contrast for each passband obtained experimentally and numerically.	54
Figure 4.15 Irradiance distribution of the star with a companion, 25000 times fainter than the star, located at $5.5 \lambda/D$ from the star center with and without a coronagraph	55
Figure 4.16 Normalized irradiance measurements done over 8 months	56
Figure 4.17 Radial average of the normalized irradiance and the corresponding standard deviation of the 10 contrast measurements	57
Figure 4.18 Setup for measuring the tilt introduced in the setup	58
Figure 4.19 On-axis performance of EvWaCo after introducing tilt along the x-axis	59
Figure 4.20 On-axis performance of EvWaCo after introducing tilt along the y-axis	60
Figure 4.21 Wavefront map calculating Zemax for a setup without introducing a defocus and after displacing the star source by $200 \mu\text{m}$.	61
Figure 4.22 Normalized irradiance at specific radial locations after introducing defocus.	62
Figure 4.23 Normalized irradiance for each corresponding LS (black circle) misalignment along the x-axis	64
Figure 4.24 Normalized irradiance for each corresponding LS (black circle) misalignment along the y-axis	65
Figure 4.25 Raw contrast performance at varying mask size.	66

Figure 5.1	Comparison between the theoretical and measured mask response along the major axis of the mask (x-axis) and the minor axis (y-axis) using the new air gap approximation. The error bars along the horizontal axis equal ± 1 pixel. Meanwhile, the error bars along the vertical axis are the standard deviation of the irradiance value from the 101 flat-field images obtained at the time of the acquisition of the experimental data. Unlike the previous estimation of the air gap, this time, the experiment and simulation perfectly match, especially close to the contact area.	69
Figure 5.2	Updated mask fitting	70
Figure 5.3	Irradiance distribution transmitted by a Gaussian apodizer.	71
Figure 5.4	2D Irradiance Distribution at the entrance pupil plane (Plane A), focal plane after the mask (Plane B), exit pupil plane (Plane C), and detector plane (Plane D) before (left column) and after adding a Gaussian apodizer (right column) in the model.	72
Figure 5.5	Normalized irradiance distribution at the CCD plane with and without a Gaussian apodizer.	73
Figure 5.6	Comparison of the Radial Average Calculation	74
Figure 5.7	Calculated raw contrast with a better fitting of the air gap.	74
Figure 5.8	Calculated raw contrasts in both the R-band (blue curve) and the I-band (Pink).	75
Figure 5.9	Transmission in unpolarized light at different θ_i	76
Figure 5.10	Normalized irradiance distribution over the full I-band at different θ_i and mask IWA	77
Figure 5.11	Raw contrast in the I-band at 48° angle of incidence and an IWA of $2\lambda/D$ along the minor axis.	77
Figure 6.1	FWHM of the Mask and the PSF at various angles of incidence	79
Figure 6.2	Appearance of possible Newton's rings in the companion channel flat field image due to an angle of incidence less than the critical angle.	80
Figure 6.3	Setup drawing for obtaining the pupil images used to determine the angle of incidence	81

Figure 6.4	Investigation on the presence of fringes in the flat-field images.	82
Figure 6.5	Mask profile using the mask pressure tool	83
Figure 6.6	Closer look at the boundary between the lens and the prism	84
Figure 6.7	Schematic and image of the upgraded EvWaCo testbed	85
Figure 6.8	Qualitative comparison of the non-coronagraphic PSFs using the flat mirror and the DM	89
Figure 6.9	Fraction of encircled energy of the non-coronagraphic PSF before and after correction	90
Figure 6.10	On-axis PSFs at the companion channel and star channel	91
Figure 6.11	Cross-section of the transmitted star PSF for an $IWA_y \approx 2\lambda/D$ in the I-band. The results indicate that the number of rings visible at the star channel highly depends on the size of the mask used.	92
Figure 7.1	Preliminary results of the EvWaCo prototype alignment in the lab.	97
Figure 7.2	Image of the EvWaCo star channel	99
Figure 7.3	First image of the diffraction lines from EXOhSPEC	99
Figure A.1	Schematic diagram of the PSF imaging mode.	108
Figure A.2	Reference setting using the laser.	108
Figure A.3	The laser beam must pass through the hole of the FPM mask.	109
Figure A.4	If the beam is properly centered, the shape of the beam transmitted through the aperture stop must also be circular.	109
Figure A.5	The beam passing through the lens L1 must be collimated: uniformly illuminated and consistent size along the optical path	110
Figure A.6	The beam passing through the lens L1 must be collimated: uniformly illuminated and consistent size along the optical path	110
Figure A.7	Adjust the orientation of the FPM so that the angle of incidence is approximately 42° .	111
Figure A.8	Adjust the position of L3 along the optical axis until a collimated beam is observed passing through the lens.	111
Figure A.9	The position of the Lyot stop must be at f_3 after L3.	112

Figure A.10 Adjust the position of the detector along the optical axis to obtain a sharp image of the focused spot.	112
Figure A.11 Schematic diagram of the pupil imaging mode.	113
Figure A.12 Check the proper location of the LS by placing an optical fiber at the location of the aperture stop.	113

Acronyms

AS	Aperture stop
BS	Beamsplitter
CCD	Charged Coupled Device
DM	Deformable Mirror
FPM	Focal Plane Mask
FTIR	Frustrated Total Internal Reflection
LS	Lyot stop
MMF	Multimode fiber
PSF	Point Spread Function
SMF	Single Mode Fiber
SNR	Signal-to-Noise Ratio
WFS	Wavefront sensor

CHAPTER 1

Introduction

What do you need to find life outside the solar system?

At four light years away, it will take four years for the light coming from the nearest star, Proxima Centauri, to reach us. To find life outside the solar system would entail the ability to measure the planet's physical characteristics remotely.

The life we know relies on water to survive. A potentially habitable planet must be located far from the star, where it is neither too hot nor too cold for liquid water to survive on the surface; such a zone is called the habitable zone. In our own Solar System, this is where Earth is. It must also have a mass that is large enough to hold an atmosphere but low enough that it does not become a gaseous giant planet (Seager, 2010).

The smallest feature that a telescope with a diameter D , observing at a wavelength λ , can resolve is given by the Rayleigh criterion expressed as $\theta = 1.22 \lambda/D$. Observing another solar system at a distance of 10 parsecs or 32.6 light years, the distance between the star and another Earth-like planet equals $0.1''$ (1 radian = 206265 arcseconds). Viewing such a very small angular separation on Earth (see Figure 1.1) requires a telescope with a diameter of at least 1 meter to observe in the visible $\lambda = 500$ nm. This is within reach with our ground-based telescopes (8-meter class telescopes) and our space-based telescope (2.4 m telescope).

The first exoplanet detected by Mayor and Queloz (both received the Nobel Peace Prize in Physics) in 1995 was called hot Jupiter (Mayor and Queloz, 1995). These planets are as big as Jupiter but orbit its host star in four days, faster than how much Earth orbits our Sun (ours takes 365 days). It was detected by a technique called the radial velocity method. The star and its planet/s orbit a common center of mass. By observing the behavior of the star through spectroscopy, one can notice a Doppler shift in its spectrum. If the

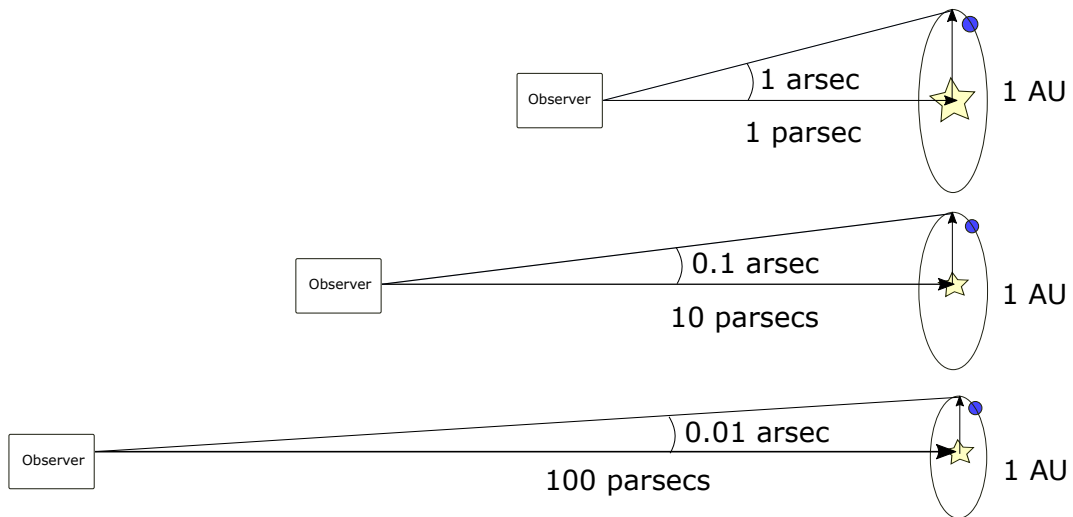


Figure 1.1: For an observer at 10 parsecs away, the angular separation between the Sun and the Earth is $0.1''$. The farther the observer, the smaller the angular separation. Image credit: Yves Rabbia

planet moves farther than the star, it will register as a redshift, while moving closer results in a blue shift. How much the star “wobbles” or shifts depends on the mass of its orbiting planet. In the case of a hot Jupiter, the shift was large enough to be detected by the resolution of the spectroscope of that time due to the planet’s mass (Traub and Oppenheimer, 2010).

Radial velocity is just one of the indirect detection methods used to detect exoplanets. The most common is the transit method – recording the change in the star’s brightness as the planet passes in front of it along the observer’s sight line. This allows us to infer the orbital radius of the planet. Currently, there are more than 5,000 exoplanets detected, and a majority of them were discovered through transit methods, owing largely to the growing number of transit surveys such as Kepler, K2, TESS (Batalha, 2014; Ricker et al., 2015; Howell et al., 2014). Figure 1.3 shows the distribution of exoplanets detected by the detection methods. There are several other indirect methods, such as astrometry, microlensing, etc., but they are unpopular due to the extreme precision and conditions they require (Fischer et al., 2014). These indirect methods only allow us to deduce the presence of a planet by studying how it affects its host star (Guyon, 2017). Radial velocity gives us information on the planet’s mass, while transit gives us information on the planet’s orbital radius, as illustrated in Figure 1.2. But how do we know if it can harbor life?

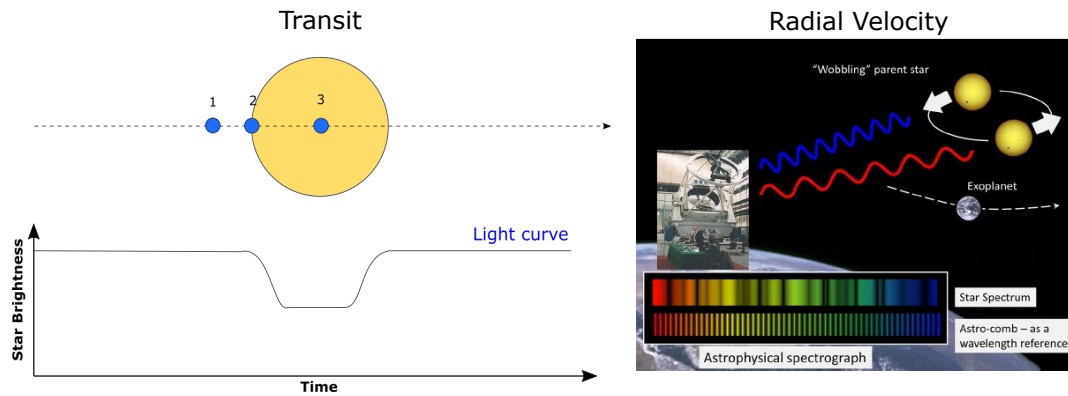


Figure 1.2: Pictorial representation of the transit method (left) and the radial velocity method (right). By observing the dimming of the stellar brightness, the planet’s orbital radius can be calculated, while the mass of the orbiting planet can be inferred from the Doppler shift of the star spectrum. Image credit for radial velocity Chih-Hao Li (SPIE Newsroom).

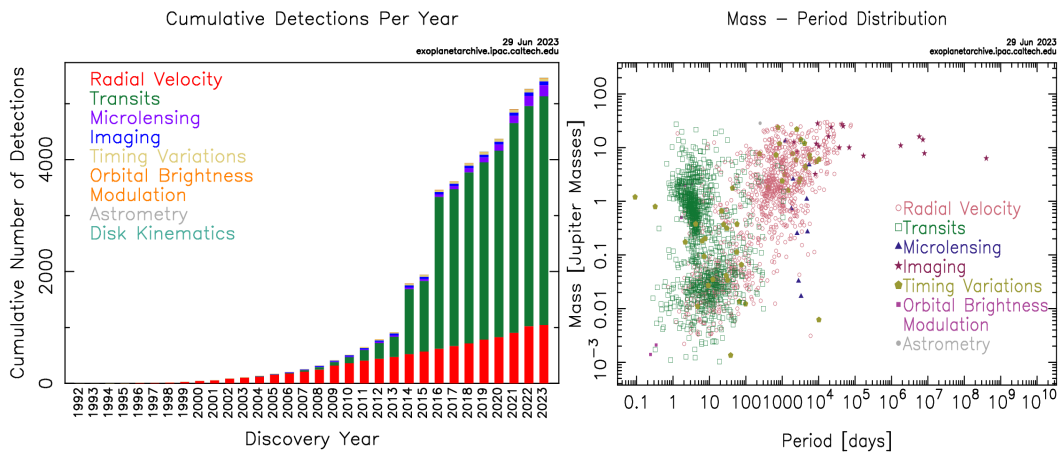


Figure 1.3: Exoplanet Detection per year and Mass-Period distribution of the detected exoplanets. Left: The number of exoplanets detected is increasing yearly, most of which are detected by transit. Right: At shorter orbital periods, the transit method detected exoplanets of varying sizes, while more massive planets in short- to medium-orbital periods were detected by radial velocity. Exoplanets detected by imaging are both massive and have larger orbits. Source: <https://exoplanetarchive.ipac.caltech.edu/>

Spectroscopy allows us to measure the physical properties of an object. Figure 1.4 is a graphical representation of the essential molecules in the Earth’s atmosphere that indicate the presence of biological activity. Although indirect methods such as transit and radial

velocity enable atmospheric characterization through transmission spectroscopy and high-resolution Doppler spectroscopy, respectively, direct detection - accessing the planet's photons only - also offers information about its surface properties, broadening the range of information that can be learned about the planet's composition and formation (Morley et al., 2015; Biller and Bonnefoy, 2018).

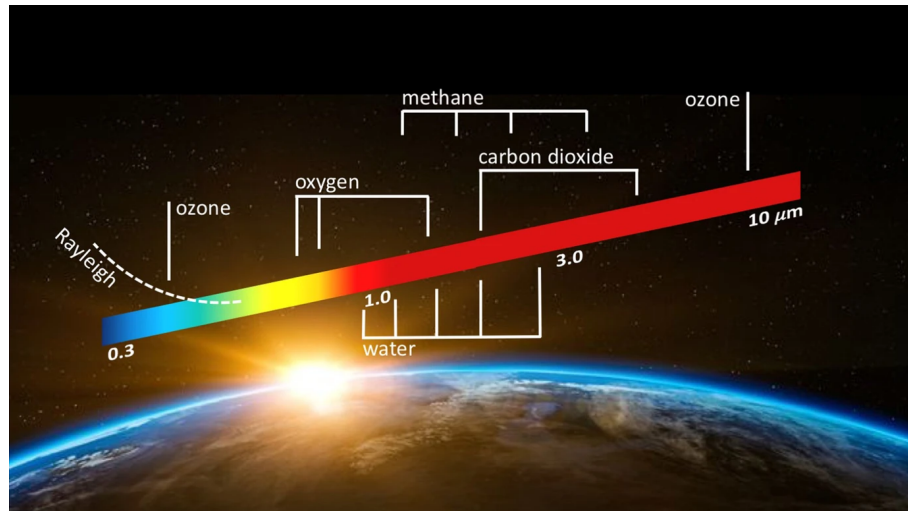


Figure 1.4: Main molecular features present at the Earth's atmosphere from the visible to infrared wavelengths: ozone (0.6 μm , 3.3 μm , 4.74 μm), oxygen (0.76 μm , 1.27 μm), water (1.1 μm , 1.4 μm , 1.9 μm , 2.5 μm - 3.2 μm , 4.3 μm), methane (1.66 μm , 2.2 μm , 3.3 μm), carbon dioxide (2 μm , 2.8 μm , 4.3 μm) (Snellen et al., 2015; Guyon, 2018)

It took a decade to get direct images of exoplanets. On the ground, the discovery of a giant planet orbiting a young brown dwarf 2M1207 (see Figure 1.5) was the first direct image obtained using the European Very Large Telescope's NACO, which stands for the Nasmyth Adaptive Optics System (NAOS) - Near-Infrared Imager and Spectrograph (CONICA) (Chauvin et al., 2004, 2005). Around this time, Marois et al. detected the HR 8799 planetary system (Marois et al., 2008). Figure 1.6 shows an image of the HR8799 where three planets were discovered first, and the fourth was discovered in 2010 (Marois et al., 2010). Even today, another interesting discovery that remains a subject of investigation is the discovery of Beta Pictoris (Figure 1.7) by (Lagrange et al., 2008). The presence of its debris disk opens up exciting discoveries on planet formation.

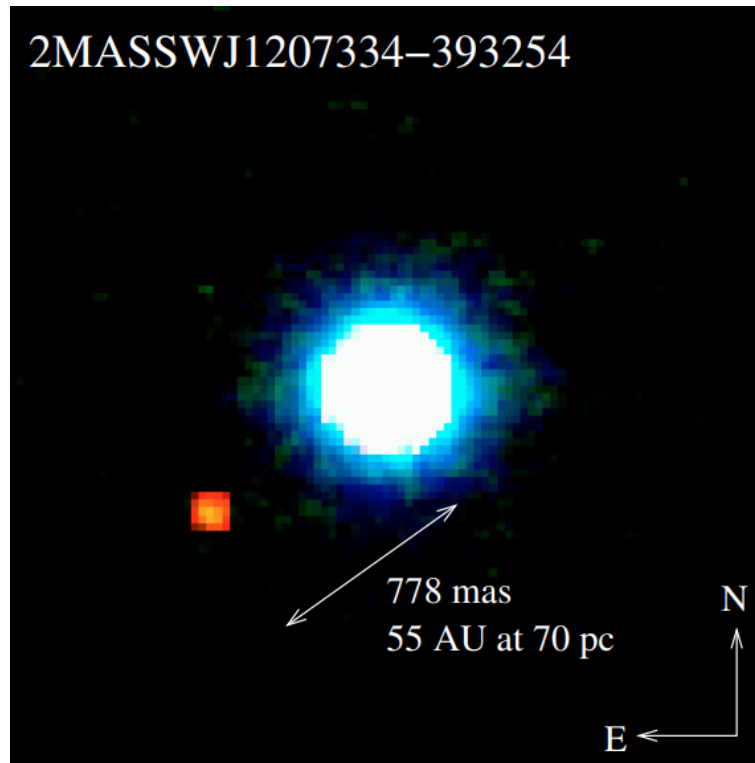


Figure 1.5: Image of the giant planet orbiting the young brown dwarf 2MASS1207 at a close separation of ~ 780 mas (~ 55 AU). It is the first direct image obtained using the VLT/NACO in 2004. (Chauvin et al., 2004, 2005).

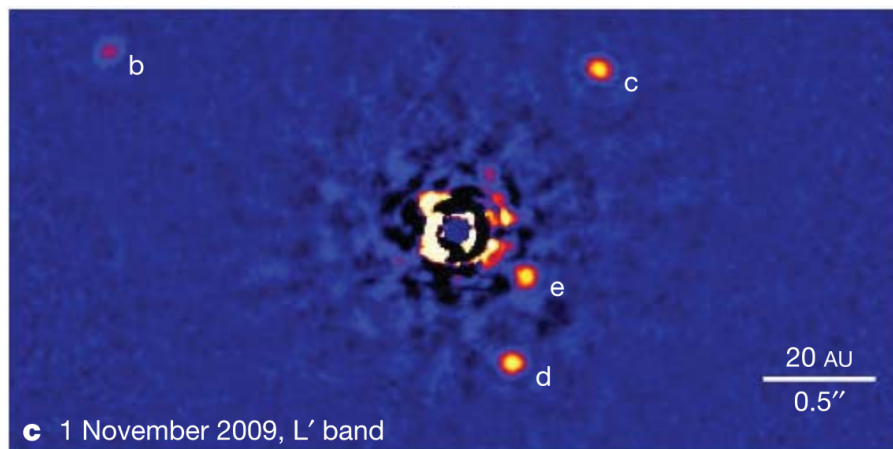


Figure 1.6: The HR8799 planetary system, composed of four young giant planets, was detected at the Keck II telescope during the 2009-2010 observing period. The image is in L-band imaging centered at the wavelength, $\lambda = 3.76 \mu\text{m}$. Planets b, c, and are located at a distance of $1.7''$, $1.0''$, and $0.6''$ from the star with a flux ratio of 10^{-5} while planet e is closer to the star at $0.4''$ (Marois et al., 2010).

1.1 The Challenges of Direct Imaging

Direct imaging remains technically and technologically challenging. Directly detecting exoplanets requires isolating the planet's light from the starlight. Viewed from a

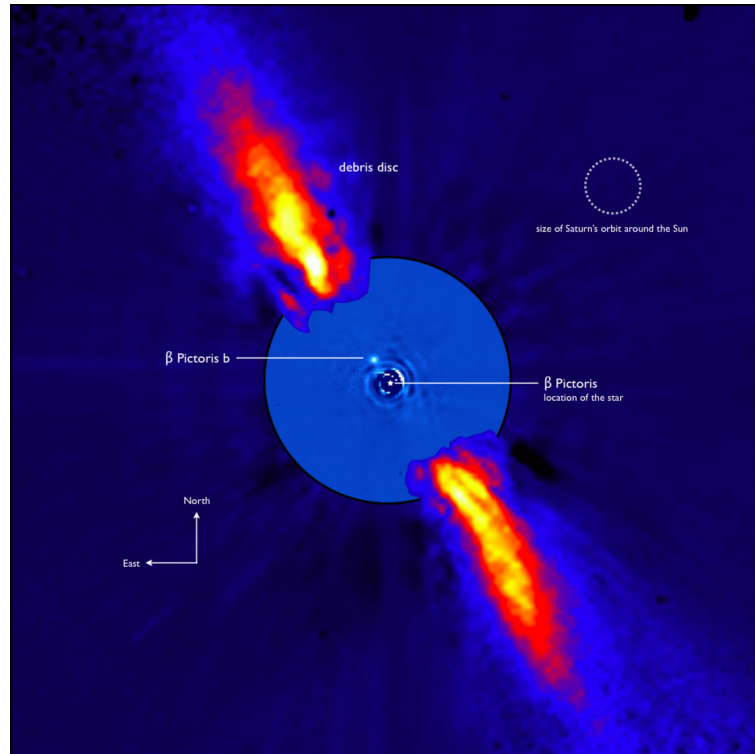


Figure 1.7: The Beta Pictoris System has a well-resolved disk and two massive planets at $\simeq 2.7$ AU and $\simeq 9$ AU. Physical properties and characteristics were obtained through various detection methods such as radial velocity, high contrast imaging, and long baseline interferometry. Image credit: ESO/A-M. Lagrange (Lagrange et al., 2008).

distance of 10 parsecs, the angular separation of a Jupiter-like planet is $0.5''$, and an Earth-like exoplanet is at $0.1''$. In terms of resolution, these separations can already be resolved by a telescope with a diameter as small as 1 meter observing in the visible wavelength, $\lambda \approx 500$ nm, without the presence of atmosphere. However, the high contrast (planet flux/star flux) poses the greatest challenge. Planets reflect the light from the star they orbit, and early in their formation, younger planets are hotter and, therefore, brighter. There are two ways to detect an exoplanet directly: 1) by the reflected light from its host star and 2) by its proper thermal emission as black body radiation. Figure 1.8 shows the normalized flux of an Earth-like and Jupiter-like planet viewed through a 4-m unobstructed telescope. At visible wavelengths ($0.3 \mu\text{m} - 1.0 \mu\text{m}$), the Earth-like planet is 10^{-10} fainter than the Sun - 1 photon from the planet versus a billion photons from the star. Even at the planet's location, the light due to the star is still a million times brighter. For a Jupiter-like planet, the contrast is more relaxed, $C \approx 10^{-9}$, since the planet is only a thousand times compared to the flux coming from the star at this location. Observing in the near-infrared

to mid-infrared is more favorable because the contrast is lower such that at $\lambda = 10 \mu\text{m}$, $C \approx 8.10^{-8}$ for an Earth-like planet and $C \approx 3.10^{-8}$ for a Jupiter-like planet (Kasting et al., 2010; Traub and Oppenheimer, 2010). Figure 1.9 compares the reflected (visible) and emitted (near-infrared) fluxes of Earth and Jupiter to the stellar flux. Most directly imaged planets are young Jovian planets due to their peak emission at the near-infrared. They are also brighter by two orders of magnitude, making their detection less challenging (Currie et al., 2022).

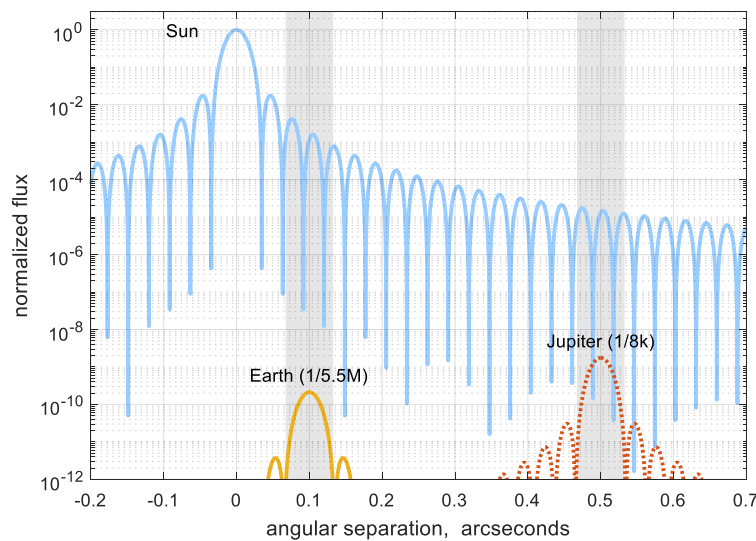


Figure 1.8: Cross-sections of the Sun, Earth, and Jupiter when viewed at 10 parsecs through an unobstructed 4-m telescope in the diffraction-limited regime. The Earth is 5 million times fainter than the Sun compared to Jupiter, which is only a few thousand times fainter. Image credit: Nemati et al. (2020).

1.2 Key Drivers for a Successful Direct Imaging

The first step towards this goal is overcoming the huge contrast between the star and the planet. This can be done by suppressing the light from the star to enable detection of its surrounding environment. Three main starlight suppression architectures exist: internal coronagraph, nulling interferometry, and starshades. All these architectures aim to remove or strongly attenuate the contribution of the stellar light at the telescope focus. Internal coronagraphs are instruments installed in a single telescope designed to block the on-axis starlight using amplitude or phase masks in the pupil or image plane (see Figure 1.10).

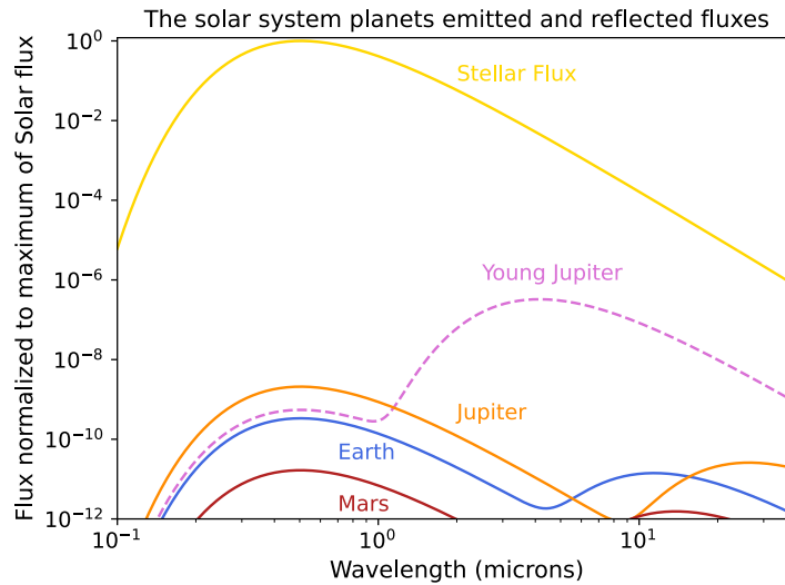


Figure 1.9: Reflected planet flux in the visible wavelengths and its corresponding emitted flux in the near-IR wavelengths (Galicher and Mazoyer, 2023; Encrenaz et al., 2013). Due to its distance from the star, Jupiter-like planets are easier to detect, especially in the near-infrared spectrum. The graph also shows the young Jupiter flux of the discovered 51 Eridani system. Young Jupiters are planets more massive than Jupiter but are self-luminous due to their age, making detection easier in the near-infrared wavelength (Macintosh et al., 2015).

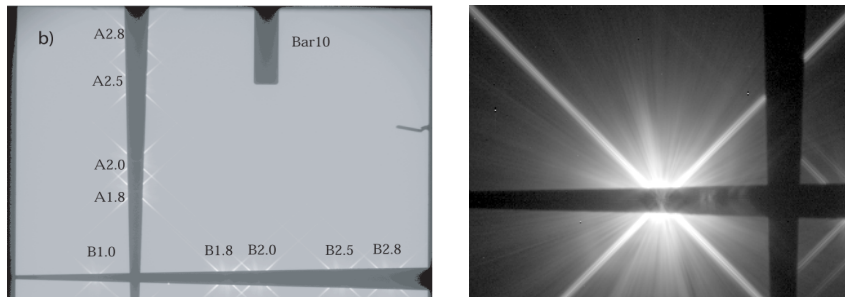


Figure 1.10: Focal plane wedges (left) in the Space Telescope Imaging Spectrograph (STIS) aboard the Hubble Space Telescope (Grady et al., 2003) and the image of the HD141569 under the coronagraphic wedge position, B1.0. The wedges block the light coming from the star at the focal plane (Mouillet et al., 2001).

Nulling interferometry utilizes at least two telescopes looking at the same star, centered along its optical axis. The light beam from one of the telescopes is delayed by half a wavelength such that when they are recombined, destructive interference occurs, leaving no starlight. Light coming from an off-axis source is reinforced rather than nulled, thus

allowing the detection of the star's surrounding environment (see Figure 1.11) (Bracewell, 1978).

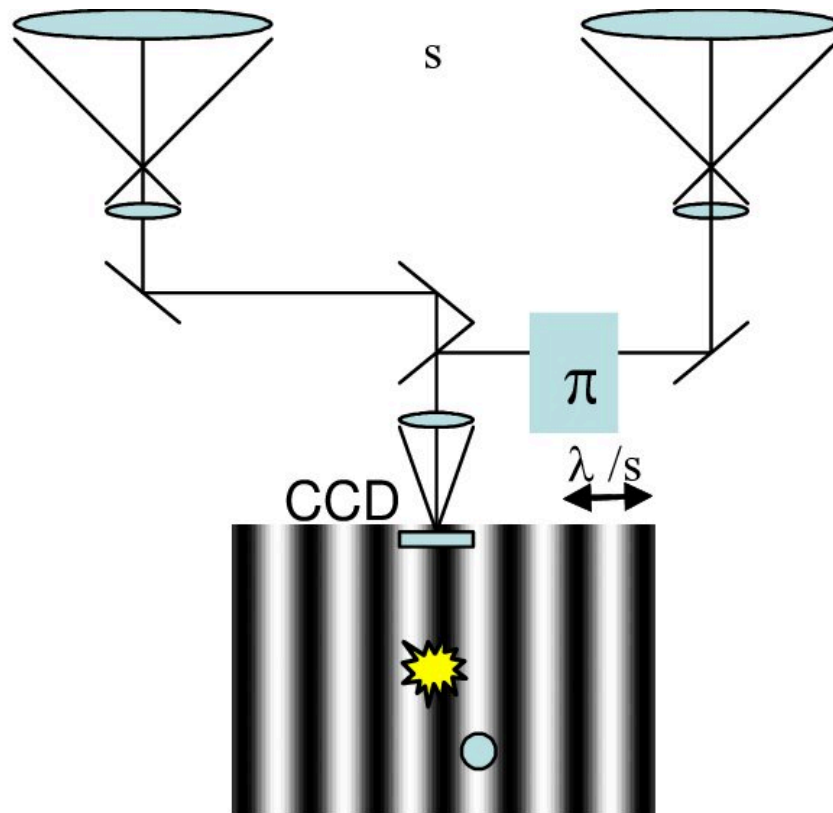


Figure 1.11: Illustration of the principle of nulling interferometry - the on-axis star signal is nulled by delaying the signal coming from one of the telescopes by π while amplifying the off-axis signal such as that of a planet (Leger et al., 1996). Image credit: (Shao et al., 2006) .

The starshade is a star-occluding concept where a petal-shaped occulter is placed between the star and the line of sight of the telescope to prevent the starlight from entering the telescope - an equivalent to blocking the contribution of the on-axis star (Cash, 2006; Cash et al., 2005). This one requires that this occulter be flown in space and placed at the correct position (see Figure 1.12). Unlike the first two architectures, this concept is still waiting to be demonstrated in space.

All these techniques are complex, requiring advanced engineering skills. Of the three, the most mature technology is coronagraphy. In ground-based imaging, the star's image at the telescope focal plane is limited by the seeing, given by λ/r_o , where r_o is the telescope's diameter, resulting in the seeing disk's size. In our best astronomical sites,

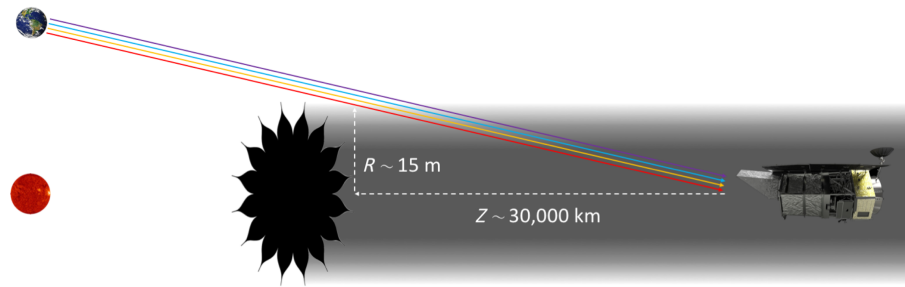


Figure 1.12: Principle of Starshades: A petal-shaped occulter is unfurled in space and positions itself between the star and the telescope to block the light coming from the star Image credit: (Arenberg and Harness, 2011).

such as Chile or Hawaii, the seeing is approximately $0.4''$, corresponding to using a telescope with a diameter of 20 cm. This is due to the atmospheric turbulence distorting the wavefront that arrives at the telescope. This is solved using an adaptive optics system comprising a wavefront sensor, wavefront corrector, and real-time control, as shown in Figure 1.13. In the case of detecting faint signals, wavefront control is used to maintain a dark hole or a region where light from the star is minimized throughout the entire integration time. Diffraction is not the only thing that limits the detection of the faint planet signal; so is scattered light from misalignment, stray light, and imperfect optics. Both coronagraphy and wavefront control work together to minimize stellar light from reaching the detector, as shown in Figure 1.14.

Figure 1.15 illustrates the full coronagraph system. Starlight suppression is just one of the key drivers for the success of direct imaging. The detector must be able to detect the signal with a high signal-to-noise ratio ($\text{SNR} > 5$). One of the most common astronomical detectors is the charge-coupled device (CCD). The detector must have very low noise and a fast frame rate to attain a sufficient SNR to relay the image to the adaptive optics control. Detectors such as an EMCCD (Electron Multiplying Charge-Coupled Device) allow us to tweak the detector's gain to detect faint objects with a sufficiently high signal-to-noise ratio. Finally, raw images obtained from the instruments are further processed to ensure the detection of a planet. The first direct images of planetary systems, HR8799 (Figure 1.6), and β Pictoris (Figure 1.7) were obtained using angular differential imaging (ADI). ADI relies on the fact that the field of view (FOV) rotates as you track the stars throughout the night. Other faint signals, such as the planet's, can be detected by subtracting the

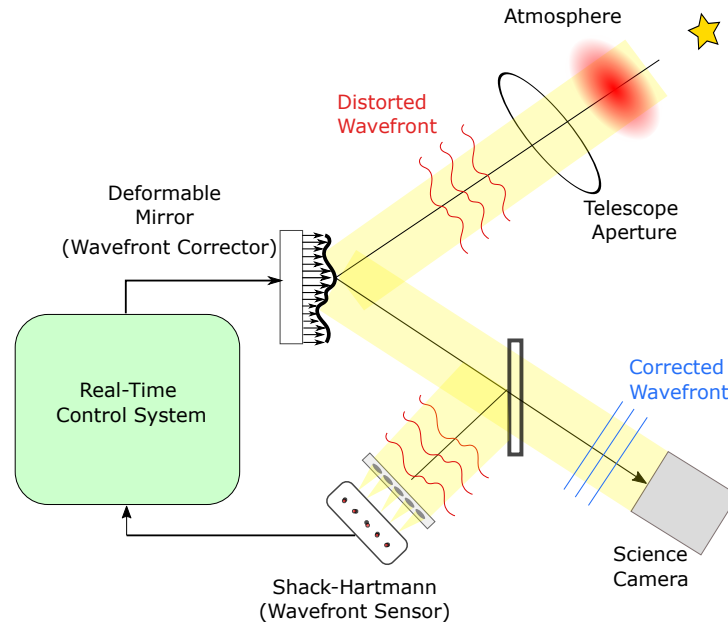


Figure 1.13: An adaptive optics system has three main components: a wavefront sensor, a wavefront corrector, and a real-time control system. Due to atmospheric turbulence, wavefronts entering the telescope are distorted. These wavefronts will be reflected by the deformable mirror towards the wavefront sensor (to measure the aberrations present) and the science camera (to assess the quality of the image). After measuring the incoming wavefront, the real-time control system calculates the appropriate command that will be sent to the DM to compensate for these aberrations.

reference star from the images.

Figure 1.16 shows that there are four key drivers to successfully detect an exoplanet: coronagraphy (starlight suppression), wavefront control through adaptive optics, detectors, post-processing techniques such as differential imaging algorithms, and PSF subtraction algorithms.

1.3 Current Status and Future of High Contrast Imaging Instrumentation

Efficient suppression of the star’s blinding light allows faint signals to be detected. As in the case of β Pictoris, circumstellar disks, dust, and other structures in the close environment of the host star can suddenly come into view, and information on such objects is valuable for understanding planet formation. Figure 1.17 shows an overview of where we are in our advancements in this field and the upcoming projects dedicated to

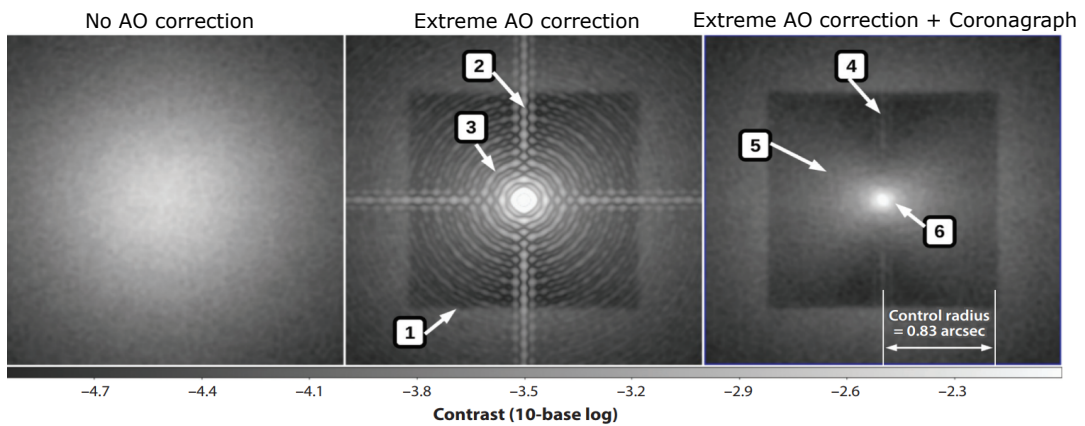


Figure 1.14: Without AO correction, the image of the star is just a huge blob of light. It would make the detection of faint signals impossible. Once the AO correction is activated, the Extreme AO (ExAO) control radius (denoted by number 1) is determined by the number of actuators of the deformable mirrors. Numbers 2 and 3 represent the diffraction rings and the telescope spiders, respectively. Once the coronagraph is in place, the diffraction rings are gone. However, there is still some residual light left due to ghost spider diffraction (4), the "butterfly" wind effect (5), and the presence of low-order aberrations (6). Image credit: (Guyon, 2018).

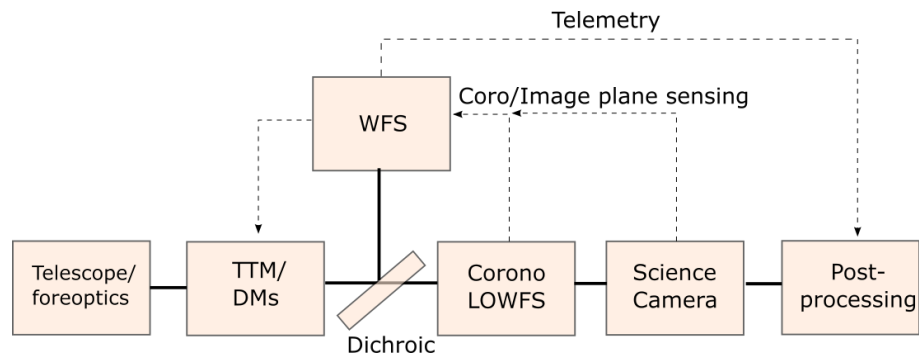


Figure 1.15: Typical coronagraph system for exoplanet detection imaging.

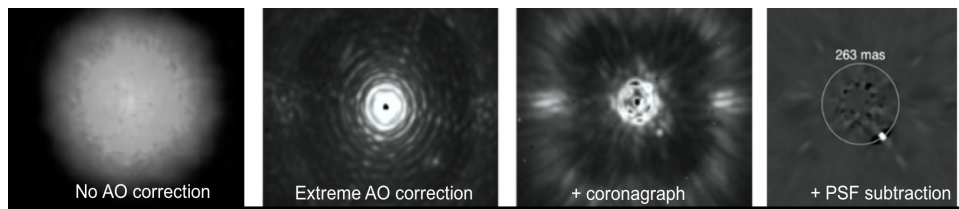


Figure 1.16: Images of the different processes needed to obtain a direct image: extreme AO, coronagraph, post-processing techniques, detector sensitivity. These images are obtained from the VLT-SPHERE. Image credit: (Currie et al., 2022)

detecting Earth-like planets. Since the first direct image in 2008, high-contrast imaging has remained challenging due to the high contrast between the star and the planet and their very small angular separation. So far, ground-based instruments were limited to a contrast ranging from 10^{-3} to 10^{-6} on the detection of young massive planets in the near-infrared (their thermal emission peaks at these wavelengths), and they have wider orbits.

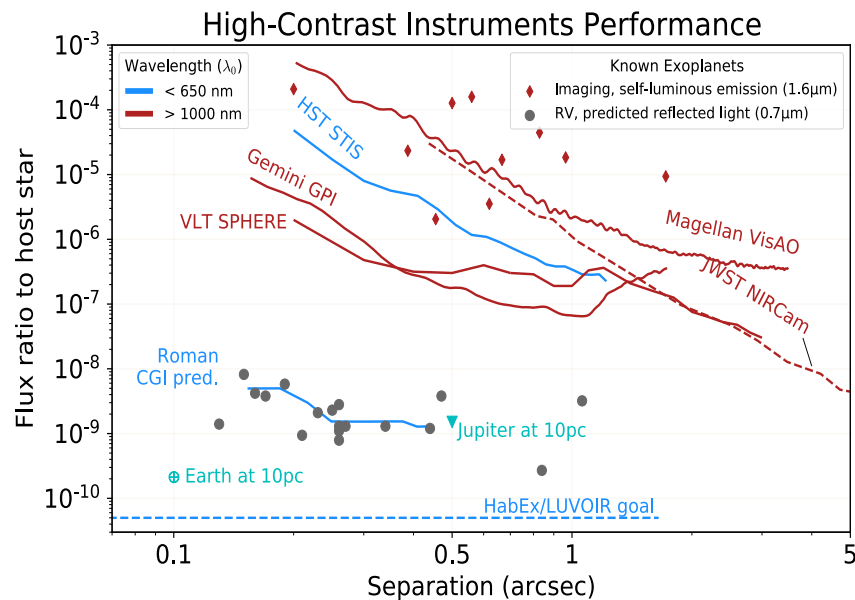


Figure 1.17: Ground-based instruments have only directly imaged young self-luminous exoplanets in the near-infrared because they are brighter and, thus, more easily detected. Closer to the star ($\geq 0.2''$), the faintest that we can detect from the ground has a flux ratio between 10^{-5} and 10^{-7} . Direct imaging in the visible wavelengths was done in space using the Hubble Space Telescope Space Telescope Imaging Spectrograph (HST STIS). The next generation of space telescopes (Roman, HabEx, LUVOIR) will attempt to image fainter planets between 10^{-8} and 10^{-9} between $0.1''$ to $0.5''$ and, ultimately, detect an Earth-like exoplanet at 10^{-10} . Source: github.com/nasavbailey/DI-flux-ratio-plot/

The atmospheric turbulence limits observations on the ground. To detect Earth-like planets in reflected light where they are fainter, high-contrast imaging needs to be done in space. The next space missions, such as the Habitable Exoplanet Observatory (Habex) and the Large UV/Optical/IR Surveyor (LUVOIR), are designed to directly image Earth-like exoplanets and, hopefully, answer mankind's long-standing curiosity, "Is there life out there?"

1.4 Summary

Detecting life outside our solar system requires accessing the light coming from the planet through direct detection to enable characterization of the planet's atmosphere for the presence of biomarkers. However, the high contrast between the parent star and its planet and their small angular separation makes this scientific endeavor challenging. At a separation of $0.1''$ from a distance of 10 pc, Earth-like planets are the most difficult to detect due to their 10^{-9} contrast in the infrared wavelengths and 10^{-10} contrast in the visible.

Successful direct detection relies on four key drivers: starlight suppression, wave-front control, post-processing, and detectors. Starlight suppression aims to block or strongly attenuate the signal from the star at the telescope image plane. One of its architecture is an internal coronagraph that consists of masks in the pupil and/or image plane so that the light coming from the star and the planet could be isolated.

1.5 About this Research

This research explores a new type of coronagraph called the Evanescent Wave Coronagraph through experiments and simulations. This coronagraph type uses the frustrated total internal reflection principle to suppress the stellar light at the telescope focal plane. This thesis is organized as follows. The next chapter provides information on coronagraphy in general, including various coronagraph designs, state-of-the-art, and technological needs. Chapter 3 focuses on the principle behind the Evanescent Wave Coronagraph, preliminary theoretical calculations, and the context and scope of my research. Chapter 4 presents the experimental results on the following investigations: raw contrast performance, inner working angle, repeatability and stability of the focal plane mask over an 8-month study, sensitivity to misalignment, and finally, detection of a simulated companion. The experimental results were then compared to numerical simulations. Chapter 5 shows the performance of the coronagraph at different inner working angles and a preliminary discussion on apodization to optimize the coronagraph performance. Chapter 6 discusses the implications of the coronagraph's current performance to the technological

gaps in coronagraphy. Finally, the thesis concludes with a general discussion of the contents and perspectives in the context of high dispersion coronagraphy, and the ongoing development for the installation of an EvWaCo prototype at the Thai National Telescope.

CHAPTER 2

Coronagraphs

In 1939, French astronomer Bernard Lyot used the coronagraph to image the faint corona of the sun without waiting for a total solar eclipse (Lyot, 1939). He placed an opaque disk, with a diameter a bit larger than the image of the solar disk, at the telescope focus, thus mimicking a total solar eclipse. This allows the light from the sun's corona to be recorded on a photographic plate. The principle of Lyot's solar coronagraph has been extended and adapted to the case of a star set on-axis where its contribution is removed at the focal plane image to hopefully detect any nearby orbiting planet, commonly known as stellar coronagraphs or coronagraphs.

Following the path of light in a typical stellar coronagraph setup (Figure 2.1), the first lens focuses the incoming stellar light on-axis and its companion off-axis at the focal plane (Plane B). By Fraunhofer diffraction (Goodman, 2005), the irradiance distribution at Plane B is the squared modulus of the Fourier transform of the aperture stop at Plane A. For a circular aperture, it is an Airy pattern (star image). At the location of the star's image, an occulting mask blocks the on-axis light from reaching the detector while allowing the off-axis source to be transmitted. Since it is in frequency space, the occulting mask acts as a high pass filter. In the spatial domain, the higher frequencies transmitted belong to sharp features in an image, such as the edge of the aperture stop. Thus, when the second lens performs another Fourier transform, it shows the pupil's image at Plane A, except that light is concentrated around the pupil's edges. The exit pupil (Plane C) shows the diffracted stellar light. Another physical stop called the Lyot stop, usually smaller than the aperture stop, is installed on this plane to block residual stellar light from reaching the detector. The last lens makes a final Fourier transform of Plane C onto the image plane at Plane D, showing the surrounding environment of the star.

Using Fourier Optics (Goodman, 2005), the propagation of light in a coronagraph

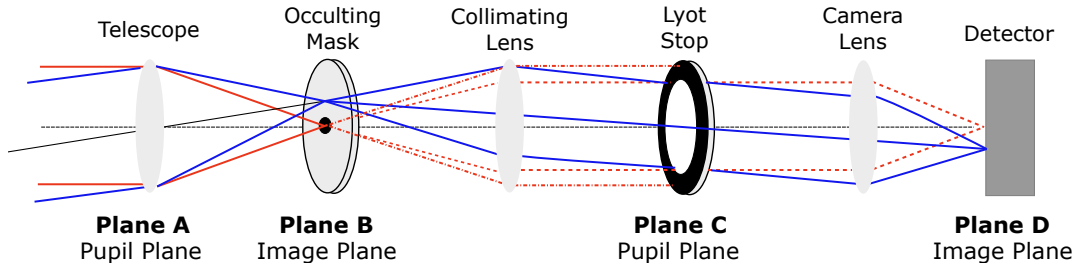


Figure 2.1: Plane A represents the location of the entrance pupil where an aperture stop is placed. Plane B represents the focal plane, where a mask blocks the on-axis starlight. Plane C re-images the aperture stop, where another diaphragm called the Lyot stop is installed to block the residual stellar light. The beam transmitted by the Lyot stop is focused on a detector located at Plane D. The broken red lines represent the path of the blocked stellar light.

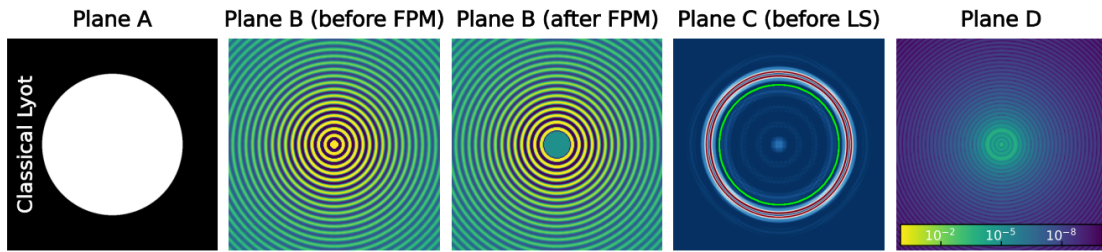


Figure 2.2: Irradiance distributions at the different planes in a typical Lyot coronagraph. Plane A Uniformly illuminated beam on a clear circular aperture. Plane B before the focal plane mask shows the star image as an Airy pattern. The central part is blocked after passing through the mask, and the rest of the rings are transmitted. After another Fourier transform, the exit pupil (Plane C) shows the diffracted stellar light, and a Lyot stop marked by the green circle blocks this light from reaching the detector. Finally, a final focusing lens images the surrounding environment of the star at the detector. Image credit: Galicher and Mazoyer (2023).

can also be described by the following formalism. Let the pupil plane complex amplitude be denoted by $P(\xi, \eta)$ while the image plane complex amplitude be denoted by $F(x, y)$ where the expression relates the pupil and image plane coordinated: $x = \xi/\lambda f, y = \eta/\lambda f$. A more rigorous derivation can be found in (Sivaramakrishnan et al., 2001).

- Entrance Pupil (**Plane A**): $P_1(\xi, \eta)$
- Complex Amplitude at the focal plane right before the occulting mask (**Plane B**): $F_1(x, y) = \text{FT}(P_1(\xi, \eta))$

- Focal plane mask amplitude transmission (**Plane B**): $M(x,y)$
- Complex amplitude after the focal plane mask (**Plane B**):

$$F_2(x,y) = F_1(x,y) \times M(x,y)$$
- Complex amplitude at the exit pupil plane (**Plane C**):

$$P_2(\xi, \eta) = FT^{-1} (FT(x,y)) = P_1(\xi, \eta) * FT^{-1} (M(x,y))$$
- Complex amplitude after passing through the Lyot stop (**Plane C**):

$$P_3(\xi, \eta) = L(\xi, \eta) \times (P_1(\xi, \eta) * FT^{-1} (M(x,y)))$$
- Complex amplitude at the detector (**Plane D**):

$$F_3(x,y) = FT(L(\xi, \eta)) * (F_1(x,y) \times M(x,y))$$

The asterisk denotes a convolution. The irradiance distribution on each plane is obtained by taking the squared modulus of the complex amplitude $|P(\xi, \eta)|^2$ in the pupil plane or $|F(x, y)|^2$ in the image plane. The coronagraph must be able to minimize the residual starlight at the exit pupil plane $P_2(\xi, \eta)$ while allowing the off-axis companion light to pass through.

2.1 Various Coronagraph Designs

The performance of a coronagraph is measured according to the following metrics:

- **Contrast** is the ratio between the residual energy behind the coronagraphic mask and the incident energy. This parameter depends on where it is measured in the focal plane, and the distance is either expressed in units of Airy width (λ/D), where λ is the observing wavelength, and D is the aperture of the telescope, or in arcseconds.
- **Inner Working Angle (IWA)** is the distance from the on-axis star that allows a 50% transmission of the off-axis source. To detect Earth-like planets, we need to probe as close to the center of the star as possible; thus, the smaller the IWA, the better.

- **Throughput** refers to how much planet light is transmitted through the system after all the masks
- **Bandwidth** is a range of wavelengths where the reported contrast applies

A stellar coronagraph has three important masks: the aperture stop (Plane A), the focal plane mask (Plane B), and a Lyot stop (Plane C) at the exit pupil. These masks are related to each other by Fourier transform. Recall that the size of the star image at the telescope's focus is given by the following:

$$\Phi_{star} = 2.44\lambda \frac{f}{D}, \quad (2.1)$$

where f and D are the telescope's focal length and diameter, respectively. This implies that the star image's size at the telescope's focus changes depending on the wavelength. Moreover, since we are dealing with capturing very faint signals, the instrument must have a high signal-to-noise ratio (SNR) given by

$$SNR \propto \sqrt{A \cdot t \cdot \tau \cdot \Delta\lambda C} \quad (2.2)$$

where A is the collector's transmission, t is the energy transmission, τ is the integration time, $\Delta\lambda$ is the range wavelengths used during the observation or the bandpass, and C is the planet-to-star-flux ratio. Hence, a coronagraph must achieve an achromatic rejection over a large spectral bandwidth, not only for flexibility of choosing the spectral channel during observations but also to achieve a good SNR (Rabbia, 2003).

The first Lyot coronagraphs used an amplitude mask, such as a hard-edged mask, to block the on-axis starlight, while the Lyot stop is an undersized aperture stop to block the residual light. This design is simple, yet this type of mask is prone to significant starlight leaks. The diameter of such an opaque mask is well-matched only at a given wavelength, making it chromatic. Furthermore, the Lyot stop's size determines the system's final throughput (collector's transmission). Since it is smaller than the aperture stop, less light is transmitted into the system.

Apodization was initially proposed as an alternative to traditional Lyot coronagraphs because it is easier to manufacture (for the case of binary masks) and does not require precise alignment. The term apodization is a Greek word that means “cutting off the feet”. For a circular aperture, the wings of the Airy pattern are due to the sharp discontinuity at the edge of the aperture. The beam transmitted through the aperture must be apodized to remove these rings. With the secondary maxima cut off, fainter objects surrounding the on-axis star may be detected.

A simple apodization function is that of a Gaussian (Spergel, 2001)(Debes et al., 2002). The techniques proposed for apodization can be classified into two families: shaped pupils with binary transmission values and apodized pupils transmission functions that are spatially varying (Kasdin et al., 2003). Examples of these are shown in Figure 2.3 and 2.4, respectively.

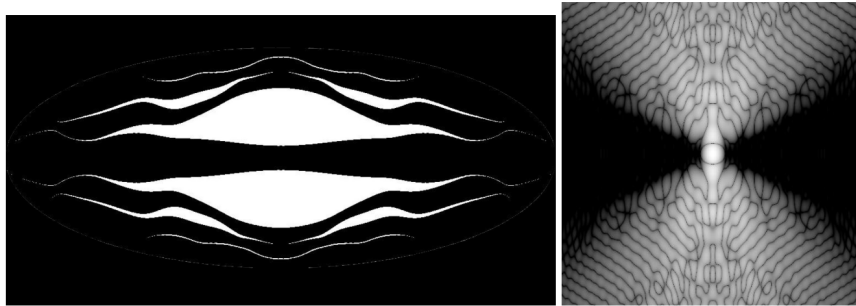


Figure 2.3: An example of a shaped pupil with multiple openings designed for an elliptical aperture. A contrast of 10^{-10} along the x-axis can be achieved up to a distance of $4 \lambda/D$ (Kasdin et al., 2005).

Coronagraph designs can be divided into three categories depending on whether they optimize only the pupil plane, the image plane, or both planes, called hybrids. Improvements on the traditional Lyot coronagraph optimize the focal plane masks by amplitude or phase. An example of the amplitude focal plane mask is the band-limited mask wherein the occulting mask is designed such that the diffracted stellar light after the occulting mask is contained within narrow zones at the exit pupil so that a Lyot stop can easily block the residual stellar light (Kuchner and Traub, 2002), as shown in Figure 2.5.

Phase masks, on the other hand, come in different varieties. Phase masks that rely on interferometric concepts are based on the coherence of light and rely either on the

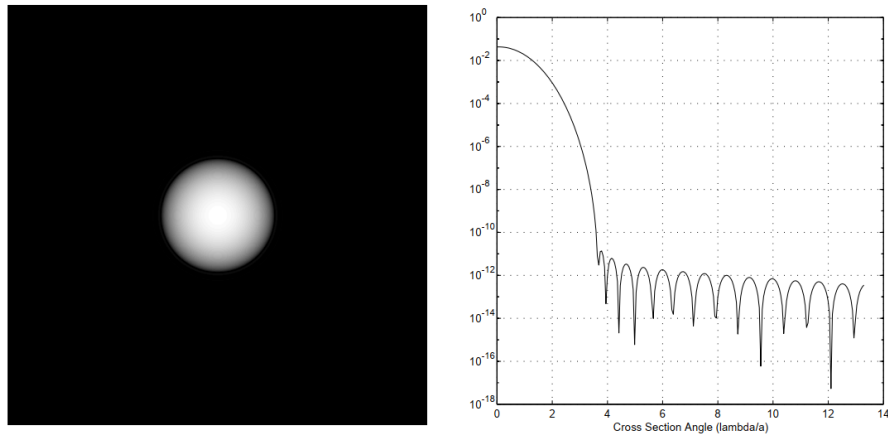


Figure 2.4: Point spread function of an azimuthally symmetric generalized prolate spheroidal apodized circular aperture and its cross-section showing an inner working angle of $3.5 \lambda/D$. A prolate spheroidal aperture is a function that where the maximum energy is contained in the central lobe. This is the basis for many of the apodization-based coronagraphs (Slepian, 1965; Kasdin et al., 2003)

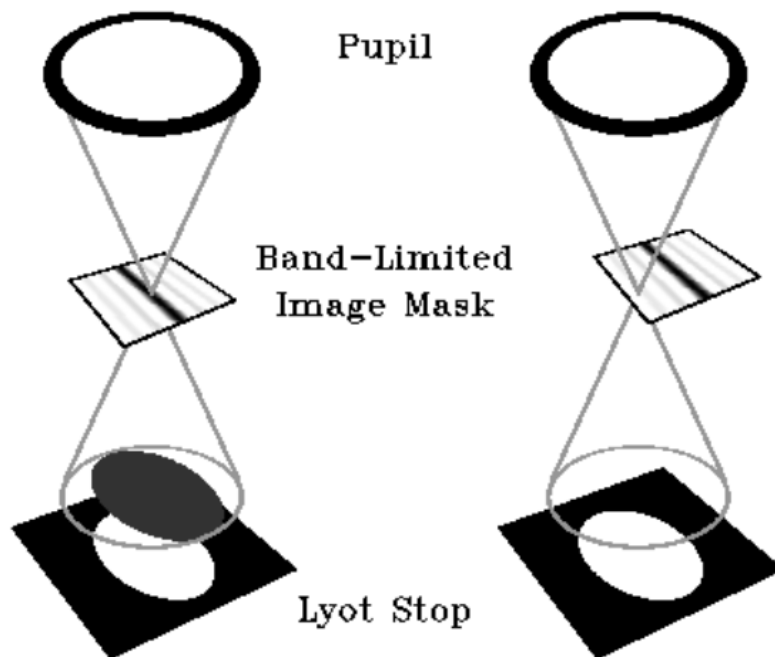


Figure 2.5: Illustration of the band-limited mask. The residual on-axis starlight is concentrated around a region near the edge of a pupil and then blocked by the Lyot stop, while the off-axis light passes through (Kuchner and Traub, 2002).

division of amplitude using a specific dephasing mask or the division of wavefront using a beamsplitter yielding two sub-waves. One sub-wave is dephased by π , which causes them to interfere destructively only on the on-axis but not the off-axis. Figure 2.6 shows

an illustration of how an achromatic interfero coronagraph (AIC) (Gay and Rabbia, 1996) and the phase mask coronagraph (PMC) work (Roddier and Roddier, 1997).

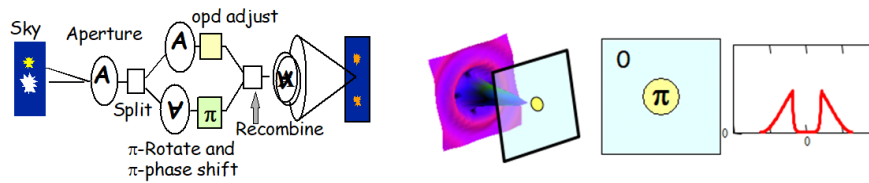


Figure 2.6: Basic principle of an interfero-coronagraph (left) and the phase mask coronagraph (right). The achromatic interfero coronagraph is based on the Michelson-Fourier interferometer, where another arm is shifted by 180 degrees, and the pupil is rotated, completely canceling the on-axis starlight. Meanwhile, the phase mask coronagraph replaces the opaque disk on the traditional Lyot coronagraph with a small phase mask that produces a 180° phase shift at the PSF core. Image credit: Gay and Rabbia (1996).

Other types of phase masks installed at the focal plane (Plane B) use a transmissive phase mask divided into four quadrants: two quadrants along the diagonal are π -shifted, and the other half is without a shift. The rejected stellar light is concentrated outside the pupil area, where a Lyot stop can further block this residual light. This mask is called the Four-Quadrant Phase-Mask (4QPM) (Rouan et al., 2000a). Another type of transmissive phase mask is the vector vortex coronagraph, which has a space-varying birefringent focal plane mask that nulls the on-axis star (Mawet et al., 2010). Figure 2.7 shows examples of how these two phase masks work.

Other coronagraph families combine a specially shaped pupil with a hard-edge focal plane mask. Coronagraphs such as the Hybrid Lyot Coronagraph (Ge et al., 2004) and the Apodized Pupil Lyot coronagraph (Aime, 2005) have optimized both the shape of the pupil and the mask to optimize the starlight suppression (see Figure 2.7). Another type of coronagraph known as the Phase-Induced Amplitude Apodization (PIAA) rearranges the incoming rays using aspheric optics to produce an output beam that resembles a prolate spheroidal amplitude distribution (see Figure 2.4), theoretically allowing detection of a faint signal close to the diffraction limit (Guyon, 2003).

2.2 State-of-the-Art

Coronagraphs are designed depending on the telescope used and the scientific objectives. High contrast observations on large telescopes combine the capabilities of a

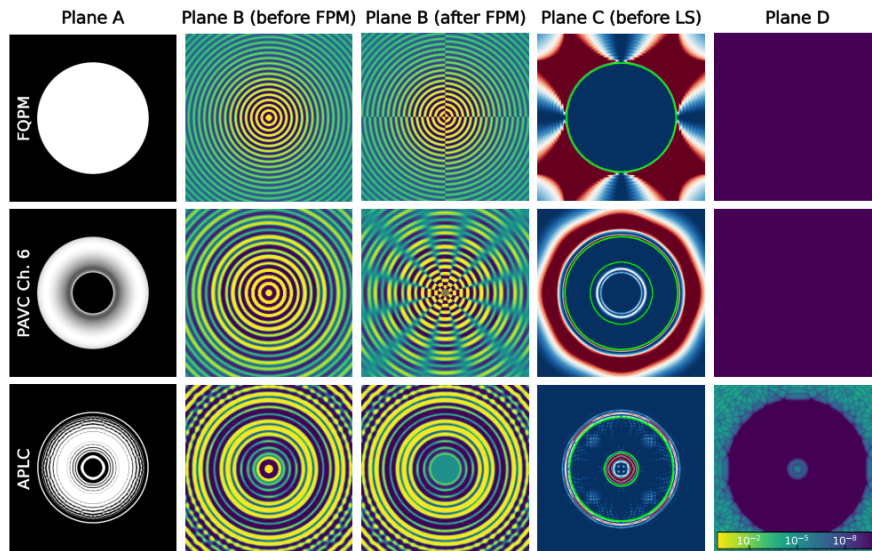


Figure 2.7: Light propagation inside three different coronagraph designs at the pupil and image planes: Four Quadrant Phase Mask (Row 1), Vortex Coronagraph Row 2, and Apodized Lyot Coronagraph (Row 3) Image credit: Galicher and Mazoyer (2023).

coronagraph and adaptive optics to suppress the starlight and control the scattered light.

Both the Spectro-Polarimetric High-Contrast Exoplanet Research (SPHERE) installed on the 8-m European Southern Observatory Very Large Telescope (ESO-VLT) and the Gemini Planet Imager (GPI) installed on the 8-m Gemini South Telescope share almost the same research objectives: detect and characterize signals of gaseous planets in the near-IR (0.95 to 1.8 microns).

However, they differ in their chosen coronagraph designs. The near-infrared channel in SPHERE is equipped with two different types of coronagraphs: the apodized pupil Lyot coronagraph (APLC) (Soummer, 2005) and the four-quadrant half-wave plate HW-4QPM (Rouan et al., 2000b; Mawet et al., 2006). These two designs are chromatic. However, they are optimized for their chosen observing wavelengths. The apodizers in the APLC were optimized with a mask diameter of $4 \lambda/D$ (IWA = $2 \lambda/D$) for APO1 and at $5.2 \lambda/D$ (IWA = $2.6 \lambda/D$) for APO2. Meanwhile, the HW-4QPM achieved a contrast of 10^{-4} at $2-3 \lambda/D$ and 10^{-5} at $6-8 \lambda/D$ on the test bench (Beuzit et al., 2019). The best contrast achieved during its first light is 10^{-6} as close as $0.2''$ from Sirius A using the integral field spectrograph with wavelength coverage from $0.95 \mu m$ to $1.65 \mu m$ (Y-H Bands) (Vigan et al., 2015).

The APLC is the chosen coronagraph for the GPI. It uses a hard-edged focal plane stop with a radius of $2.8 \lambda/D$ (Macintosh et al., 2014). The first light of the Gemini Planet Imager (GPI), which is installed on the Gemini South Telescope in Chile, showed 5σ contrasts of 10^{-6} at $0.75''$ and 10^{-5} at $0.35''$ in the H-band ($\lambda_{mid} = 1.6 \mu\text{m}$, $\lambda/\Delta\lambda = 4\%$).

Another instrument called the Subaru Coronagraphic Extreme Adaptive Optics System (SCEXAO) is installed at the 8-m Subaru Telescope. Unlike the SPHERE and GPI, SCEXAO focuses on detecting and characterizing exoplanetary systems and provides a high-contrast imaging platform for various coronagraph designs with inner working angles less than $3\lambda/D$. The instrument works on a broad wavelength range from 600 nm to 2500 nm. Its two key coronagraphs are the phase-induced amplitude apodization complex mask coronagraph and the vector vortex coronagraph. Both coronagraphs offer the lowest IWA (as close as $1 \lambda/D$) and the highest throughput but are also very sensitive to wavefront errors (Jovanovic et al., 2015).

To ease the stringent constraints in exoplanet detection, another technique proposed is to combine a high contrast imager with a high-resolution spectrograph commonly known as the High Dispersion Coronagraph (HDC) (Riaud and Schneider, 2015; Mawet et al., 2017). The high contrast imager serves as a spatial filter that would separate the light from the star and the planet. On the other hand, the high-resolution spectrograph acts as the spectral filter that would differentiate the star from the planet.

The star/planet contrast sensitivity in a high-resolution spectrograph has already been demonstrated at 10^{-4} . Coupling it with a high contrast imager with a raw suppression level that is better than 10^{-3} , the contrast sensitivity of the high dispersion coronagraph can be as deep as 10^{-7} . Simulation results show that using a High Dispersion Coronagraph on ground-based telescopes an Earth-like exoplanet around M-dwarf stars may be detected as long the coronagraph has a 10^{-4} suppression level (Wang et al., 2017). The Keck Planet Imager and Characterizer (KPIC) utilizes this technique by implementing a fiber injection unit that connects the light from the Keck adaptive optics to the NIRSPEC, its infrared echelle spectrograph, via single-mode fibers (Morris et al., 2020).

2.3 Technological Gaps in Coronagraphy

Ideally, the goal is to design a coronagraph with a small inner working angle, high contrast over a large spectral bandwidth, and a high throughput. Unfortunately, serious technological challenges must be overcome to achieve this goal. For example, while phase masks such as the vector vortex and four-quadrant phase mask work well at small inner working angles, they are chromatic. Making them achromatic to a certain spectral bandwidth comes at the cost of manufacturing complexity. The same issue is faced in the PIAA despite reaching an IWA close to the diffraction limit - the optics are challenging to manufacture. Coronagraphs with small IWA are also sensitive to low-order aberrations and stellar angular diameter. A mask with a larger IWA, such as the APLC, may be less sensitive to these aberrations, but at the cost of the mask size. A comparison of the different coronagraph performances can be found in (Guyon et al., 2006). Finally, wavefront control imposes a hard limit on the contrast that can be achieved. The wavefront error must be at most ten picometers to achieve a 10^{-10} contrast.

While there is already so much to look forward to with all the advancements in coronagraphy, the required technology for Earth-like planet detection needs to be attained. So far, according to NASA's Exoplanet Exploration Program Technological Plan, the required raw contrast is only obtained in the lab using a hybrid Lyot coronagraph at 4×10^{-10} for a pupil with no obscuration/segmentation and at inner working angles $3-9\lambda/D$ at 10% bandwidth at 550 nm while the raw contrast for obscured pupils is at 1.6×10^{-9} for the same bandwidth but farther from the center - between 6 and $10 \lambda/D$ obtained from Roman Coronagraph Lab demos (Crill, 2022). There is still a need to reach a raw contrast of 10^{-10} with a throughput greater than 10% at an IWA $\leq 3 \lambda/D$ in an obscured/segmented pupil.

2.4 Summary

There are different kinds of stellar coronagraphs, and they are grouped into families depending on which plane they modify, either the pupil plane or the image plane. The performance of each coronagraph is measured by its contrast, inner working angle (IWA),

throughput, and bandwidth. Probing into the close environment of the star requires a coronagraph that works at smaller inner working angles. Unfortunately, there are significant trade-offs: phase masks that work well at small inner working angles are chromatic, while shaped pupils or binary apodized pupils can offer achromaticity at the expense of larger inner working angles. Coronagraphs, such as Vector Vortex and Phase Induced Amplitude Apodization (PIAA), can achieve good contrast, achromaticity, and high throughput. However, the manufacturability of the off-axis mirrors for PIAA and phase mask for Vortex is complex. Thus, there is still a need for a coronagraph that offers deep contrasts ($< 10^{-7}$) at smaller inner working angles and an achromatic rejection of a large bandwidth with a sufficient planet throughput.

CHAPTER 3

The Evanescent Wave Coronagraph

The concept of the Evanescent Wave Coronagraph was proposed in 2003 by Yves Rabbia. It is a type of Lyot coronagraph with an amplitude focal plane mask comprising a lens and a prism placed in contact, as shown in Figure 3.1. The concept is inspired by Newton's rings and the tunneling effect of the evanescent waves in the frustrated total internal reflection (FTIR) phenomenon. The prism is oriented at an angle of incidence greater than the critical angle, resulting in total internal reflection except at the contact area. This is the rejection mask: the on-axis beam is transmitted, and the off-axis beam is reflected. This mask provides an apodization to the star's PSF by properly shaping the materials in contact (Rabbia, 2003).

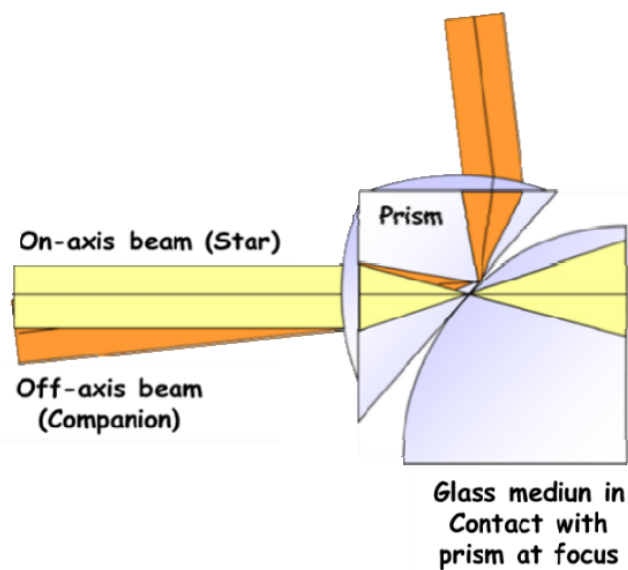


Figure 3.1: The focal plane mask comprises a lens and prism placed in contact. It uses the frustrated total internal reflection principle to separate the starlight from the planet's light. (Rabbia, 2003; Buisset et al., 2017)

3.1 Frustrated Total Internal Reflection

An incoming plane wave, E_i , that is incident on the interface between two media is partly reflected and transmitted. The amount of light reflected and transmitted is determined by Fresnel relations. These relations depend on the index of refraction, incidence angle, and light polarization (Gross, 2005; Zhu et al., 1986). Consider the case of a thin, homogenous film shown in Figure 3.2 where the Fresnel relations of the first two media are given by

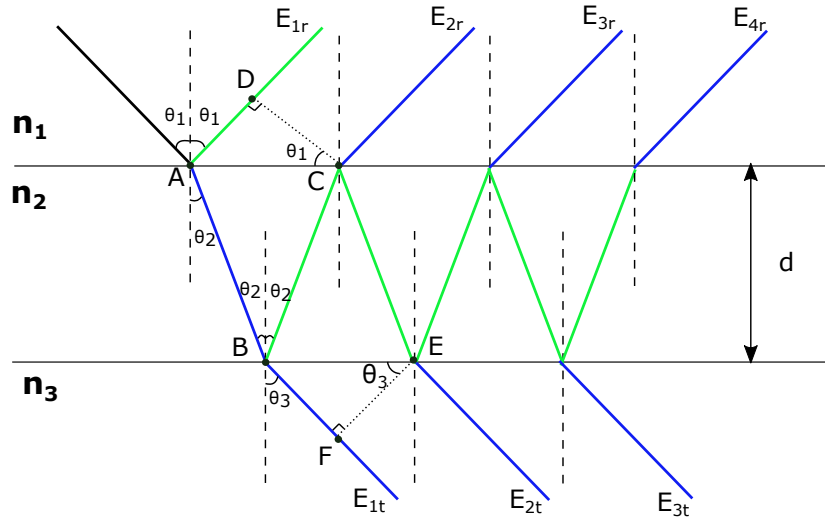


Figure 3.2: Reflection and transmission at a thin, homogeneous film

$$\begin{aligned}
 t_{12}^{\parallel} &= \frac{2n_1 \cos \theta_1}{n_2 \cos \theta_1 + n_1 \cos \theta_2}, \\
 r_{12}^{\parallel} &= \frac{n_2 \cos \theta_1 - n_1 \cos \theta_2}{n_2 \cos \theta_1 + n_1 \cos \theta_2}, \\
 t_{12}^{\perp} &= \frac{2n_1 \cos \theta_1}{n_1 \cos \theta_1 + n_2 \cos \theta_2}, \\
 r_{12}^{\perp} &= \frac{n_1 \cos \theta_1 - n_2 \cos \theta_2}{n_1 \cos \theta_1 + n_2 \cos \theta_2}.
 \end{aligned} \tag{3.1}$$

From the equation above, θ_1 is the incident angle, n_1 and n_2 are the indices of refraction of the first and second medium, respectively, and θ_2 is the transmission angle. Using Snell's law, the transmission angle becomes

$$\theta_2 = \sin^{-1}\left(\frac{n_1}{n_2} \sin \theta_1\right). \quad (3.2)$$

The optical path difference (OPD) of the transmitted beam at medium three is given by

$$OPD_t = n_2 d \cos \theta_2 \quad (3.3)$$

and its corresponding phase difference is equal to

$$\delta = kOPD = \frac{2\pi}{\lambda} n_2 d \cos \theta_2. \quad (3.4)$$

In terms of the incident angle, θ_1 , Equation 3.4 can be rewritten as

$$\delta = \frac{2\pi d}{\lambda} (n_2^2 - n_1^2 \sin^2 \theta_1)^{1/2}. \quad (3.5)$$

The transmission coefficient, t_{13} , is then expressed as

$$\begin{aligned} t_{13} &= t_{12}t_{23}e^{i\delta} + t_{12}e^{i\delta}r_{23}r_{21}t_{23}e^{i2\delta} + t_{12}e^{i\delta}r_{23}r_{21}r_{23}r_{21}t_{23}e^{i4\delta} + \dots \\ &= t_{12}t_{23}e^{i\delta} + t_{12}e^{i\delta}r_{23}r_{21}t_{23}e^{i2\delta} \sum_{m=0}^{\infty} r_{23}^m r_{21}^m e^{i2m\delta}. \end{aligned} \quad (3.6)$$

Meanwhile, the optical path difference between the two reflected beams, E_{1r} and E_{2r} , is given by

$$OPD_r = n_2(\overline{AB} + \overline{BC}) - n_1(\overline{AD}), \quad (3.7)$$

that is just twice the phase difference of the transmitted beam. Thus, the light reflected at the medium 1, denoted by r_{13} , is given by

$$\begin{aligned}
r_{13} &= r_{12} + t_{12}r_{23}t_{21}e^{i2\delta} + t_{12}r_{23}r_{21}r_{23}t_{21}e^{4i\delta} + t_{12}r_{23}r_{21}r_{23}r_{21}r_{23}t_{21}e^{6i\delta} + \dots \\
&= r_{12} + t_{12}r_{23}t_{21}e^{2i\delta} \sum_{m=0}^{\infty} r_{23}^m r_{21}^m e^{2mi\delta}.
\end{aligned} \tag{3.8}$$

The Stokes' relations connect the transmission and reflection coefficients for the light coming from the first medium and the light from the second medium. The following expressions describe them,

$$\begin{aligned}
t_{12}t_{21} + r_{12}^2 &= 1, \\
r_{12} &= -r_{21}.
\end{aligned} \tag{3.9}$$

Using Taylor's expansion and Stokes' relations, the transmission and reflection coefficients can be simplified to (Born and Wolf, 2002)

$$t_{13} = \frac{t_{12}t_{23}e^{i\delta}}{1 + r_{12}r_{23}e^{i2\delta}}, \tag{3.10}$$

and

$$r_{13} = \frac{r_{12} + r_{23}e^{i2\delta}}{1 + r_{12}r_{23}e^{i2\delta}}. \tag{3.11}$$

so that the reflected wave amplitude and transmitted wave amplitude are given by,

$$E_r = r_{13}E_i, \tag{3.12}$$

and

$$E_r = t_{13}E_i. \tag{3.13}$$

Total reflection occurs when the first medium's refraction index is greater than the

second medium's, such as when light transitions from glass to air. The light intensity is maximum in the interface plane at total internal reflection. These waves damped along the interface are called “evanescent waves” (Gross, 2005; Hecht, 2017). In this case, the phase change becomes negative and thus can be rewritten as

$$\delta = i\delta' \quad (3.14)$$

where

$$\delta' = \frac{2\pi}{\lambda} d \left[n_1^2 \sin^2 \theta_i - 1 \right]^{\frac{1}{2}}, \quad (3.15)$$

so that Equations 3.10 and 3.11 are now expressed as

$$t_{13} = \frac{t_{12}t_{23}e^{-\delta'}}{1 + r_{12}r_{23}e^{-2\delta'}}, \quad (3.16)$$

and

$$r_{13} = \frac{r_{12} + r_{23}e^{-2\delta'}}{1 + r_{12}r_{23}e^{-2\delta'}} \quad (3.17)$$

while the corresponding phase delays are represented as (Born and Wolf, 2002)

$$\tan \delta_r = \frac{r_{23}(1 - r_{12}^2 \sin 2\delta)}{r_{12}(1 + r_{23}^2) + r_{23}(1 + r_{12}^2) \cos 2\delta}, \quad (3.18)$$

and

$$\tan \delta_t = \frac{1 - r_{12}r_{23}}{1 + r_{12}r_{23}} \tan \delta. \quad (3.19)$$

At the detector plane, the irradiance of the reflection and transmission coefficients are calculated as $|r_{13}|^2$ and $|t_{13}|^2$, respectively. In unpolarized light, the irradiance is expressed as

$$\begin{aligned}
R &= \frac{1}{2} \left(|r_{13}^{\parallel}|^2 + |r_{13}^{\perp}|^2 \right) \\
T &= \frac{1}{2} \left(|t_{13}^{\parallel}|^2 + |t_{13}^{\perp}|^2 \right).
\end{aligned} \tag{3.20}$$

These evanescent waves propagate when a third medium is placed as close or in contact with the second medium such that their phase change is equal to δ' . As the evanescent waves penetrate the third medium, they decay exponentially, and their strength reaches a value of $1/e$ from the interface up to the penetration depth equal to (Hecht, 2017)

$$d = \frac{\lambda}{2\pi \sqrt{n_1^2 \sin^2 \theta_1 - 1}}. \tag{3.21}$$

For a 45° incident angle traveling from glass ($n_{glass} = 1.5$) to air ($n_{air} = 1$) at a wavelength of $\lambda = 532$ nm, the penetration depth is $d = 240$ nm, which is less than the source wavelength. By introducing a third medium with an index of refraction close to the first medium and inserting an optical component in the second medium such that its thickness is of the order of the wavelength, the total internal reflection becomes “frustrated,” thus the term “frustrated total internal reflection (FTIR)”. The optical component in the second medium allows the evanescent waves to cross the gap, thus causing the tunneling effect of the light (Zhu et al., 1986).

3.2 The Focal Plane Mask

The EvWaCo focal plane mask comprises a lens and a prism placed in contact with an air gap that can be initially approximated using the Newton’s rings setup in Figure 3.3, where a plano-convex lens is placed on top of a flat plate, with its convex part facing the flat plate. Thus, the air gap is given by

$$d(r) = \frac{r^2}{2R}, \tag{3.22}$$

where r is the radial distance from the center of the contact, and R is the radius of curvature of the lens.

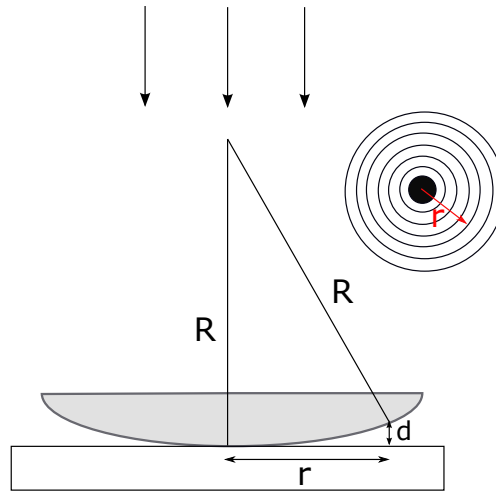


Figure 3.3: Newton's rings setup in reflected light

When the contact between the lens and the prism is very clean (no dust particles, for example), light undergoes a phase change of π , resulting in destructive interference. In the case of EvWaCo, placing the star at this contact area would completely remove the starlight. However, our prism is oriented at an angle greater than the critical angle. This leads to the starlight being transmitted by propagating evanescent waves instead of being destroyed. Meanwhile, an off-axis light will undergo total internal reflection. Figure 3.4 shows that with respect to the PSF at the prism's hypotenuse, the mask will be asymmetric due to the angle of incidence. In the framework of high contrast imaging, EvWaCo's focal plane mask possesses capabilities that will be valuable to coronagraphy: the mask adapts itself to the wavelength, the size and shape of the mask are adjustable (tunable IWA), and both the light from the star and the companion can be collected simultaneously (efficient star centering).

3.3 Early Beginnings

The Center for Optics and Photonics, in collaboration with the Laboratoire Hubert Curien and the Institute d'Optique Graduate School, developed a testbed back in 2016 to demonstrate the concept at optical wavelengths [600 nm, 900 nm]. Preliminary theoretical calculations, including the first proof of concept, were presented in (Buisset et al., 2017).

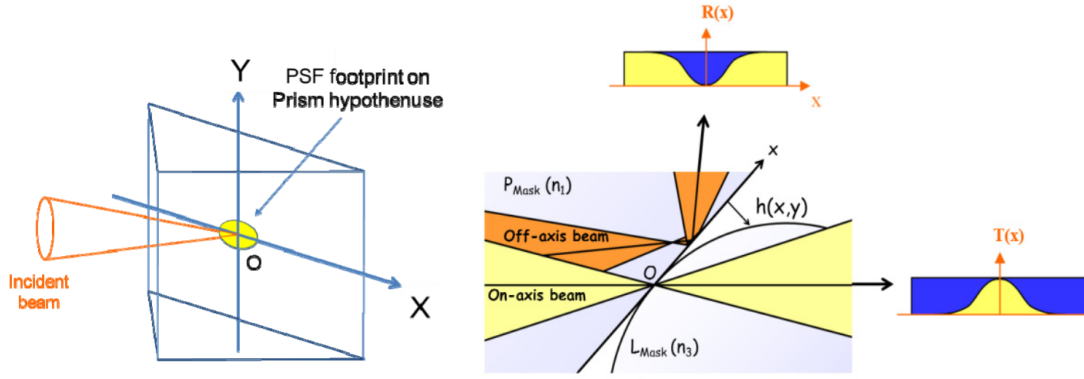


Figure 3.4: Due to the incident angle, the mask appears elliptical, where the minor axis is shorter than the major axis by a factor equal to $\cos\theta$. The figure on the right shows a close-up view of the interface between the prism and the lens. (Buisset et al., 2017)

Later, similar results were obtained at a narrow bandpass centered at 880 nm ($\Delta\lambda/\lambda \approx 6\%$) and at 780 nm ($\Delta\lambda/\lambda \approx 3\%$) (Alagao et al., 2017) (Alagao et al., 2017). These experiments also included observing both the planet and star channels simultaneously. With an inner working angle of $6 \lambda/D$ along the x-axis and $8 \lambda/D$ along the y-axis, the preliminary performance in unpolarized light obtained over the full I-band ($\lambda_c = 800$ nm) shows a normalized irradiance of a few 10^{-6} at distances from the optical axis in the focal plane between $10 \lambda/D$ and $20 \lambda/D$, and a few 10^{-7} between $20 \lambda/D$ and $50 \lambda/D$. A simulated companion, 30000 fainter than the star, located at $15 \lambda/D$, was also detected with an SNR ≈ 75 (Buisset et al., 2017). However, these experiments used a large mask (IWA $\geq 5 \lambda/D$).

Preliminary results on the EvWaCo bench were obtained using the old focal plane mask (FPM), where the control between the lens and the prism is not yet an integrated system, as shown in Figure 3.5. It is composed of off-the-shelf components mounted on passive support without adaptive optics in the laboratory. The static prism is mounted on a rotation stage and translating stages while the lens is glued on a prism held by a kinematic mirror mount installed on an XYZ translating stage. This mechanical structure makes it difficult to control the pressure between the lens and the prism. It needs additional mirrors to properly direct the beam towards the companion channel, as shown in Figure 3.5.

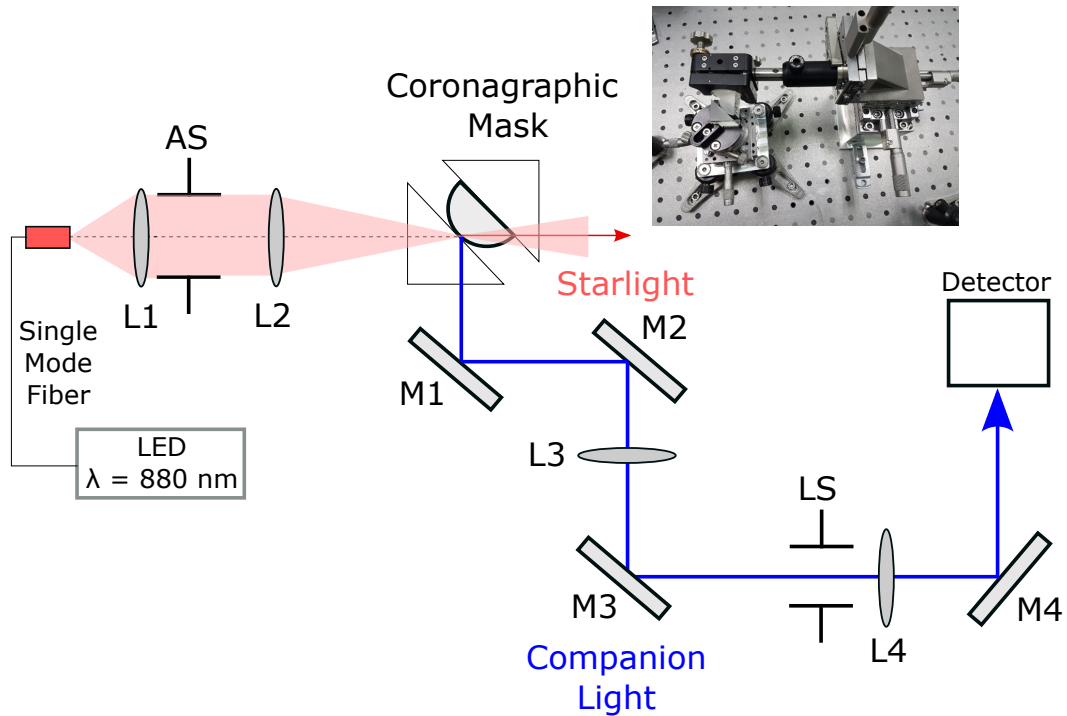


Figure 3.5: Optical setup used to demonstrate the preliminary studies in EvWaCo (Buisset et al., 2017)

3.3.1 The Upgraded Focal Plane Mask

The previous optomechanical mount largely limited the preliminary results. By the end of December 2018, the upgraded optomechanical mount was ready for testing. Figure 3.6 shows a conceptual upgraded focal plane mask that controls the direction of the beam and the adjustment of the pressure between the lens and prism, all integrated into one system. The prism is installed on a static mount comprised of two translating stages with micrometers that control the position of the FPM at the focus and two micrometers resting on two base plates used to control the tilt. Glued to the prism, the lens sits on a high-precision linear slide connected to the static mount. The actuator installed on the same mount compresses the attached coil spring to adjust the pressure between the lens and the prism. In its current design, the force over the contact area can be controlled from 0 N to 50 N with an accuracy of 0.02 N. The details of the more compact EvWaCo testbed will be described in the next chapter (Alagao et al., 2021b).

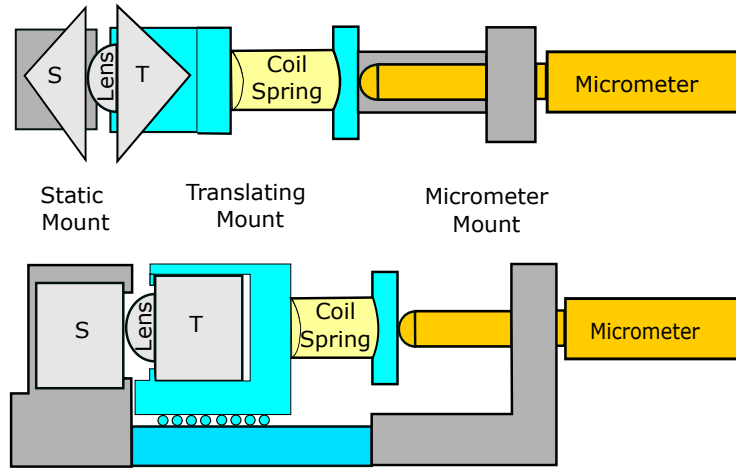


Figure 3.6: Conceptual design of the EvWaCo coronagraphic mask.

3.4 Context of the PhD Research

The results of this preliminary testbed laid the groundwork for an EvWaCo prototype that will also be installed on the 2.4 m Thai National Telescope. This prototype will serve as a technological demonstrator of both the coronagraph and its adaptive optics system. This prototype is a joint project between NARIT Center for Optics and Photonics, Centre de Recherche Astrophysique de Lyon (CRAL), Institut d’Optique Graduate School (IOGS), and Laboratoire Hubert Curien (LabHC). It is specified to observe in the R- and I-bands with a raw contrast (defined in Chapter 4) of 10^{-4} at an inner working angle of $3 \lambda/D$ ($0.5''$). The limiting magnitude of the central object is 8. So far, this demonstrator is set to observe late-type main sequence stars and bright dwarfs brown dwarfs (Ridsdill-Smith et al., 2023). Table 3.1 lists the prototype’s main specifications.

Hence, at the start of this Ph.D. research, the following research objectives set the course of my PhD studies:

- 1) To define the optical alignment procedure of the Evanescent Wave Coronagraph prototype and implement this procedure in measuring on-sky optical performance
- 2) To simulate the effect of central obscurations on the coronagraph performance using Evanescent Wave Coronagraph analytical and numerical models and

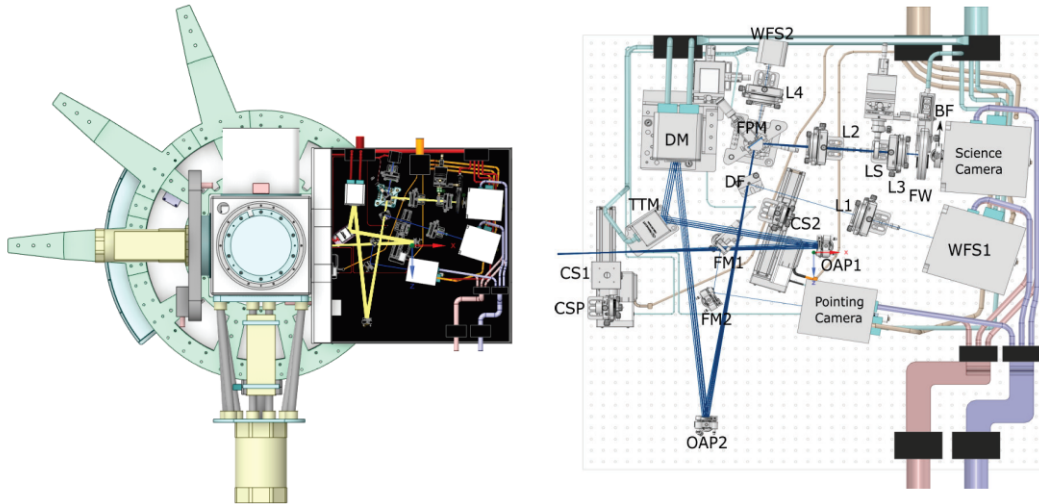


Figure 3.7: (left) First version of the EvWaCo Prototype Design on the Thai National Telescope installed vertically and (right) its contents. The following are the components inside the prototype: calibration source 1 (CS1), calibrating sphere (CSP), off-axis parabola 1 (OAP1), off-axis parabola 2 (OAP2), flip mirror 1 (FM1), folding mirror 2 (FM2), tip-tilt mirror (TTM), deformable mirror (DM), dichroic filter (DF), calibration source 2 (CS2), collimating lens 1 (L1), wavefront sensor 1 (WFS1), focal plane mask (FPM), collimating lens 2 (L2), Lyot stop (LS), focusing lens 3 (L3), filter wheel (FW), broadband filter (BF), science camera, collimating lens 4 (L4), and wavefront sensor 2 (WFS2). (Alagao et al., 2021a)

optimizing an apodizer in the optical system to reach the highest throughput and the deepest contrast

- 3) To couple the coronagraph's star channel with a high-resolution spectrograph and analyze the spectrum of the star during the observation of the companion

3.5 Scope of this PhD Research

The Evanescent Wave Coronagraph is a concept proposed by Yves Rabbia in 2003, and the proof of concept was later demonstrated in 2016 at the Center for Optics and Photonics at the National Astronomical Research Institute of Thailand. The early preliminary calculations, which serve as the starting point, are documented in (Buisset et al., 2017). Before my PhD, I was already in charge of this instrument's full alignment, data gathering, and partial analysis. My PhD research further explores the capabilities of the Evanescent Wave Coronagraph at smaller inner working angles ($\leq 3 \lambda/D$). The main focus is characterizing and optimizing the EvWaCo focal plane mask through experiments and numerical

Table 3.1: Optical Specifications of the EvWaCo Prototype.

Parameter	Specification	Comments
Science channel spectral band	R- and I- bands	Goal: V-, R- and I-bands
Strehl ratio	$SR \geq 0.8$	$\lambda = 800 \text{ nm}$, $m_v = 8$, $s \approx 1''$
AO loop frequency	$\geq 1 \text{ kHz}$	Real-time compensation
Entrance pupil shape and size	1.2 m x 0.8 m	Unobstructed pupil
DM number of actuators	192 actuators	16 actuators across pupil major axis
Raw contrast	$\leq 10^{-4}$ at IWA	$\Delta m \approx 10$
Inner working angle	0.5''	Target: $\leq 0.3''$ ($2 \lambda/D$ at 800 nm)
FOV	10''	AO active area and star halo
Plate scale	0.08''	2 pixels per λ/D
Central object limiting magnitude	8	$SR \approx 0.8$ in I-band

simulations to answer its implications on the objectives set at the start of my PhD.

CHAPTER 4

Experimental Validation and Characterization

With the ability to adjust the actuator while maintaining the stability of the focal plane mask along the line of sight, the next step is to assess the performance of the coronagraph at smaller inner working angles ($\leq 3\lambda/D$) using this upgraded focal plane mask. This chapter focuses on the experimental procedures used to determine the performance of EvWaCo and its sensitivity to low-order aberrations such as tilt and defocus, including the repeatability of the results and the stability of the focal plane mask.

4.1 The Setup

Figure 4.1 shows a schematic diagram of the more compact EvWaCo testbed with the upgraded focal plane mask. This testbed has two sources: one mimicking the host star and another one, the companion. The star source comprises a stable tungsten lamp focused on a $50\ \mu\text{m}$ multi-mode fiber (MMF) by an achromatic doublet lens. The MMF is then connected to a single mode fiber (SMF) to direct the light toward the coronagraph. Meanwhile, the light source for the companion is an LED with a central wavelength, $\lambda_c = 780\ \text{nm}$ ($\Delta\lambda/\lambda \approx 3\%$) that is injected into another SMF. The beamsplitter BS recombines the beam from the star and companion source. The aperture stop transmits the collimated beam from the lens L1. Lens L2 focuses the beam on the focal plane mask (FPM). The prism used in the focal plane mask is an N-BK7 right angle prism from Thorlabs with an anti-reflection coating of $650\ \text{nm} - 1050\ \text{nm}$ at its legs, while the plano-convex lens placed in contact is an uncoated Thorlabs N-BK7 with an $18\ \text{mm}$ lens diameter and $30\ \text{mm}$ focal length.

At the FPM plane, the beam can either be reflected or transmitted depending on its angle of incidence, θ_i . In this particular setup, the angle of incidence of the chief ray is approximately 42° . The on-axis beam gets transmitted towards the star channel.

The transmitted starlight is re-imaged onto a second CCD camera, CCD2, using a pair of achromatic doublet lenses. The off-axis beam gets reflected towards the companion channel. From the FPM, lens L3 collimates the beam and directs it towards the Lyot stop. The Lyot stop is a circular mask with a slightly smaller diameter than the AS. This beam is then focused toward another detector, CCD1. A filter wheel that houses a neutral density filter and another achromatic doublet is installed in front of the camera. Its purpose is to allow the imaging of modes from PSF to pupil and vice versa during the alignment and measurement. Table 4.1 lists the values of the optical components used in the testbed. The size of the resolution element (λ/D) is 20 microns at the detector plane, which means that we have at least 2.7 pixels per λ/D at $\lambda_c = 800$ nm. A step-by-step alignment procedure is presented in Appendix A.

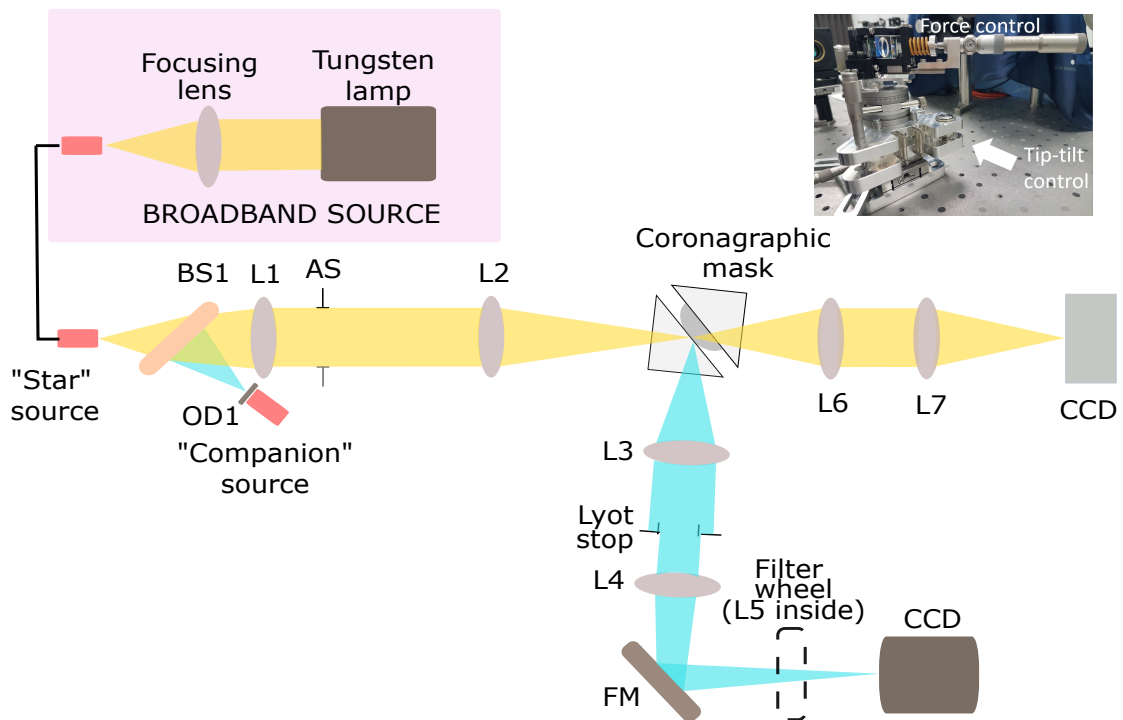


Figure 4.1: Schematic diagram of the EvWaCo testbed used to characterize the coronagraph performance at small IWA ($\leq 3\lambda/D$).

Table 4.1: Parameters in the EvWaCo Testbed.

Parameter	Value (in mm)	Comments
f_1	200	Thorlabs B-coated Achromatic doublet
f_2	300	Thorlabs B-coated Achromatic doublet
f_3	150	Thorlabs B-coated Achromatic doublet
f_4	100	Thorlabs B-coated Achromatic doublet
f_5	75	Thorlabs B-coated Achromatic doublet
f_6	60	Inside the filter wheel
D_{AS}	8	
D_{LS}	3.25	$0.8D_{AS}$
d_{pix}	0.0074	FLI Microline pixel size
T_{CCD}	-20	(in degrees) CCD cooling temperature

4.1.1 Pupil Irradiance Distribution

When the star is on-axis, the energy at the exit pupil is mostly concentrated at the edges, forming a fine annular shape due to the diffraction of light, as shown on Figure 4.2 (right), while on the same figure, the exit pupil plane shows a uniformly illuminated beam when the star source is placed off-axis. This is expected since the focal plane mask only allows the high frequencies to be propagated to the detector plane, and these high frequencies represent fine features such as the edge of the aperture stop. A lens L5 is activated inside the filter wheel to obtain these images. The pupil diameter is approximately 2 mm with an average extension width equal to 86 μm . At this location, a Lyot stop, equal to 81% of the exit pupil diameter, is installed - reducing the light transmitted to the detector to 65% of the incident light.

4.1.2 Mask Response

When obtaining flat-field images, an integrating sphere and a narrow-band spectral filter with a central wavelength of λ_c are temporarily installed between the lens L1 and the aperture stop, as shown in Figure 4.3.

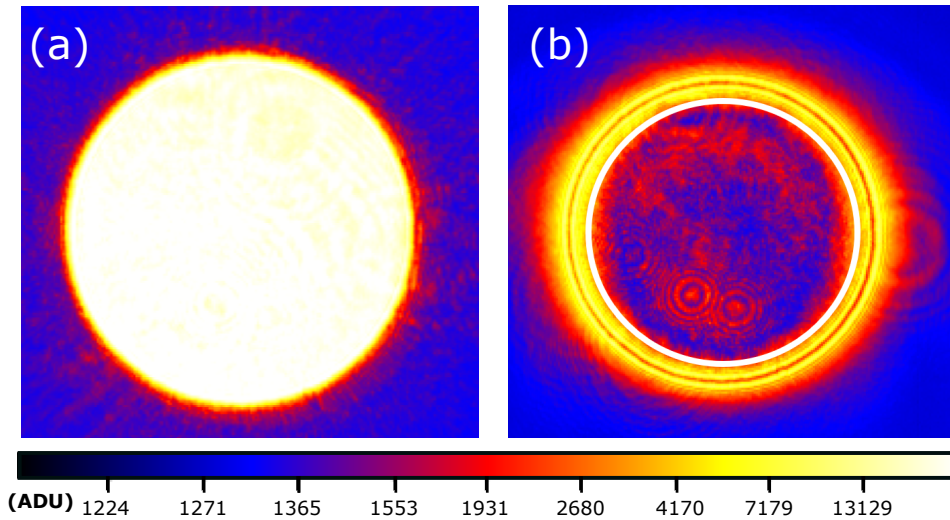


Figure 4.2: Irradiance distribution at the exit pupil or central wavelength $\lambda_C = 780$ nm ($\Delta\lambda/\lambda \approx 3\%$). When the star PSF is off-axis (left), the result is a uniform irradiance while light is concentrated along the edges when the PSF is centered on the mask. The Lyot stop (white circle) is slightly smaller than the aperture diameter by 81%.

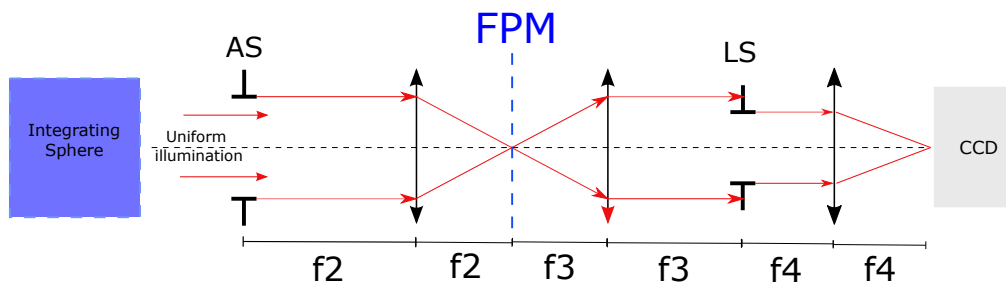


Figure 4.3: Schematic diagram of the setup to obtain the flat field (mask) images.

To demonstrate the capability of the upgraded focal plane mask to adjust the pressure between the lens and the prism easily, the force applied on the prism was varied from 0.10 N and 10.5 N, as shown in Figure 4.4. These measurements used a source with a central wavelength of $\lambda_c = 800$ nm with a Full Width at Half Maximum (FWHM) of 40 nm. The calculated force assumes a configuration where a sphere is placed in contact with a flat plate (Hertzian contact stress) that relates the diameter of the contact area to the pressure, for a given micrometer reading (Budynas and Nisbett, 2014). Figure 4.5 shows a cross-section of the mask response to increasing pressure showing that the mask size increases as the pressure on the prism increases.

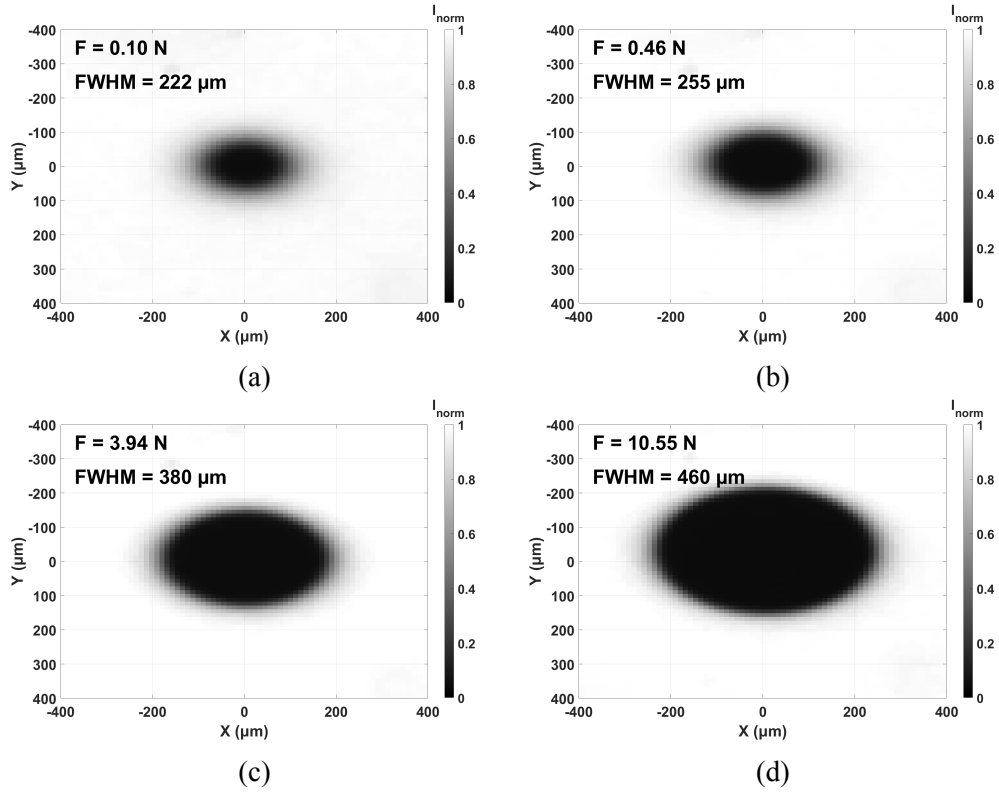


Figure 4.4: Flat-field (mask) images showing the mask response to increasing pressure on the prism.

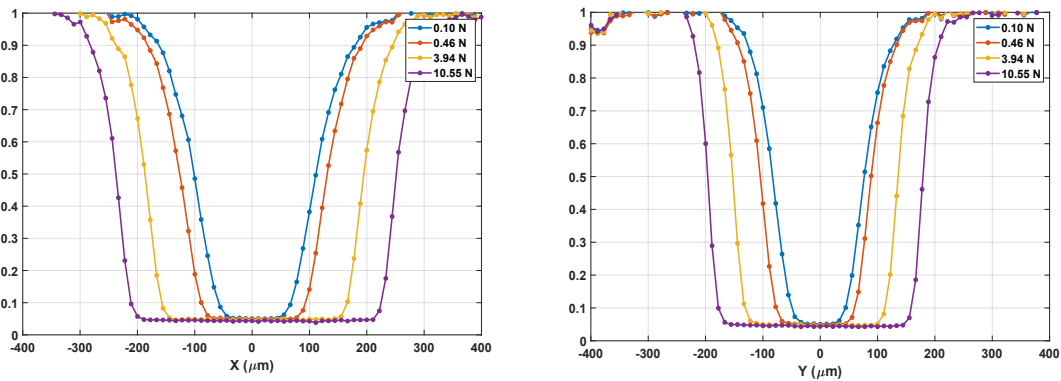


Figure 4.5: Cross-section of the mask reflection profiles as the force applied increases, resulting to increasing the mask FWHM and the contact area.

4.1.3 Modelling the air gap

The EvWaCo coronagraphic performance highly depends on the air gap - a critical parameter for FTIR to occur. For our setup, the air gap can only be estimated by finding the best equation, resulting in a mask that matches our experimental results. For a mask at a given pressure, the air gap for a mask with an IWA of $3 \lambda/D$ along the minor axis can

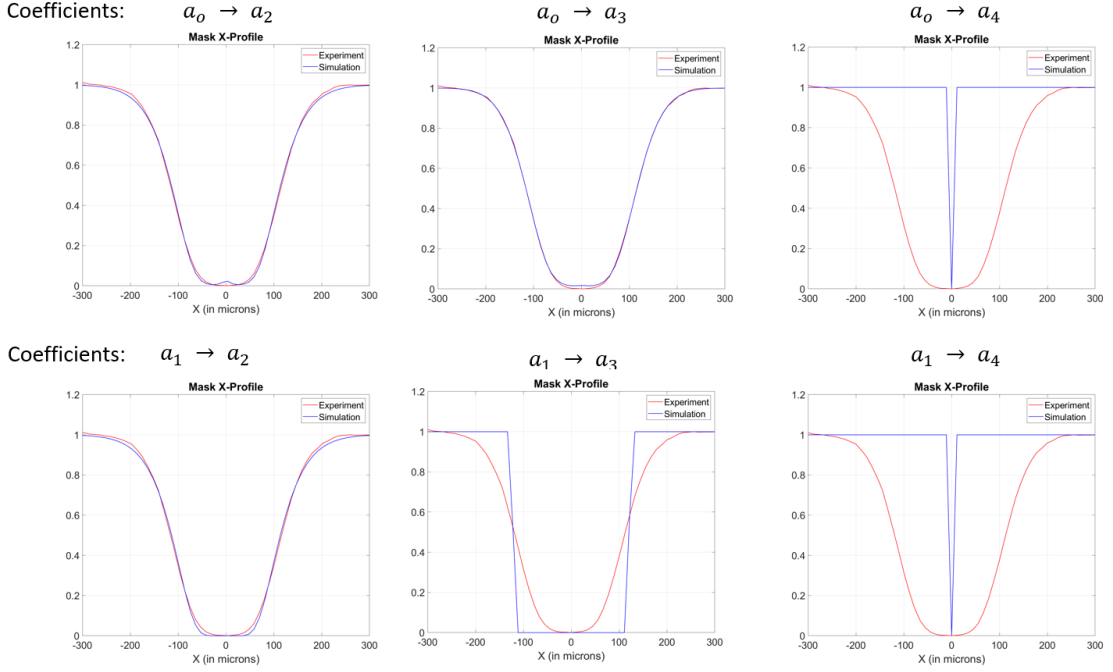


Figure 4.6: Corresponding mask cross-section along its major axis for different representations of the air gap obtained by varying the number of polynomial coefficients used in the optimization. The best approximation of the air gap is when only the first-degree and second-degree polynomials are considered, as shown by the better fit between the experimental and simulated mask profiles.

be deduced by calculating the coefficients of the following polynomial equation:

$$d(\rho) = \max(a_1\rho + a_2\rho^2, 0), \quad (4.1)$$

where ρ is the radial distance to the contact point in the prism hypotenuse plane, $a_1 = -1.10 \cdot 10^{-3}$ and $a_2 = 36 \mu\text{m}^{-1}$, resulting to an air gap shown in Figure 4.7. A Matlab built-in function called *fminsearch*, using the Nelder-Mead simplex direct search (Lagarias et al., 1998), was used to find the best polynomial coefficients that minimizes the sum of the squared difference between the simulated and experimental mask data. The choice for the number of coefficients in the polynomial needed is shown in Figure 4.6.

The theoretical and experimental mask profiles in Figure 4.8 show that the FWHMs (and their corresponding IWA) along X and Y are $FWHM_x \approx 240 \mu\text{m}$ ($IWA_x \approx 4.00 \lambda_1/D$) and $FWHM_y \approx 180 \mu\text{m}$ ($IWA_y \approx 3.00 \lambda_1/D$), respectively, at the wavelength $\lambda_c = 800 \text{ nm}$ in unpolarized light. The mask is asymmetric, with its X-axis larger than its

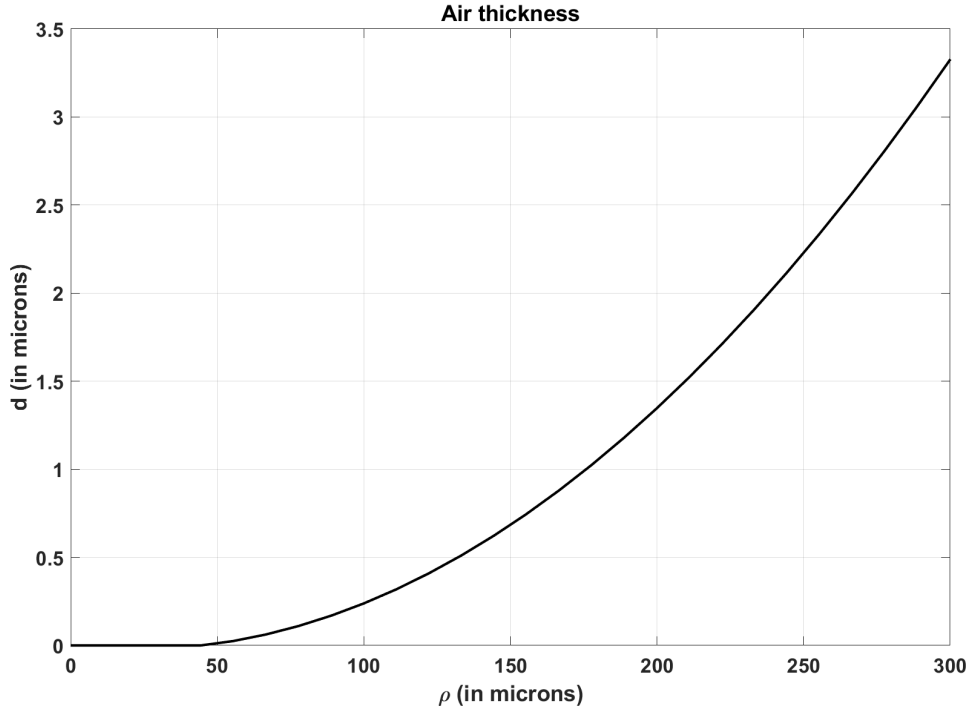


Figure 4.7: Air gap for the mask at $IWA_y = 3 \lambda/D$ using the coefficients: $a_1 = -1.10^{-3}$ and $a_2 = 36 \mu\text{m}^{-1}$.

Y-axis axis, due to the angle of incidence at the FPM (Buisset et al., 2017). With a ratio of $IWA_x/IWA_y = 1.33$, this corresponds to an angle of incidence, $\theta_i \approx 42^\circ$.

Close to the contact area, the theoretical mask transmission is slightly smaller than the experimental one. Farther from the contact area, up to about $+150 \mu\text{m}$ along the x-axis and $+125 \mu\text{m}$ along the y-axis, both the theory and experiment have a good agreement, implying that the location of the FWHM is at least correctly modeled. There is, however, a slight discrepancy after the FWHM which may not significantly impact the raw contrast calculation.

4.1.4 Mask response at different wavelengths

For the measurement of the mask response at λ_2 , the source was changed to an LED emitting at $\lambda_{peak} = 617 \text{ nm}$ and a spectral filter centered at $\lambda_2 = 650 \text{ nm}$ ($\Delta\lambda = 40 \text{ nm}$).

Figure 4.9 compares the theoretical and experimental mask profiles obtained at two different wavelengths using the approximation of the air gap obtained in the previous

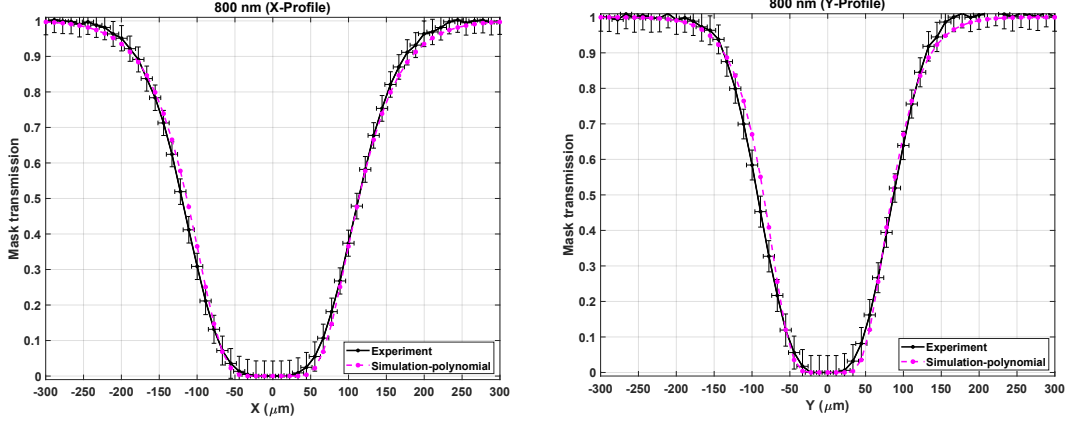


Figure 4.8: Comparison between the theoretical and measured mask response along the major axis of the mask (x-axis) and the minor axis (y-axis). Horizontal error bars are equal to ± 1 pixel, while vertical error bars represent a standard deviation from the 101 flat-field image obtained.

section. For a mask to be considered achromatic, the size of the mask must vary depending on the wavelength such that the mask obtained at λ_2 (blue curve) must be smaller than the ones obtained at λ_1 (pink curve). This is observed at λ_2 where $FWHM_X \approx 208 \mu\text{m}$ ($IWA_X \approx 4.27 \lambda/D$) and $FWHM_Y \approx 158 \mu\text{m}$ ($IWA_Y \approx 3.24 \lambda/D$) - confirming the mask's inherent behavior to adapt to the wavelength.

4.2 Raw contrast performance

Following the formalism described in (Ruane et al., 2018), the raw contrast is calculated as :

$$C(x, \lambda) = \frac{\eta_s(x_o, \lambda)}{\eta_p(x_o, \lambda)}, \quad (4.2)$$

where $\eta_s(x_o, \lambda)$ is the fraction of available starlight detected and $\eta_p(x_o, \lambda)$ is the fraction of companion light detected. The quantity $\eta_s(x_o, \lambda)$ is given by

$$\eta_s(x_o, \lambda) = \int_{AP(x_o)} PSF_{coro}(x, 0, \lambda) dx, \quad (4.3)$$

where $PSF_{coro}(x, 0, \lambda)$, is the image of the on-axis star at the detector and $AP(x_o)$, is equal

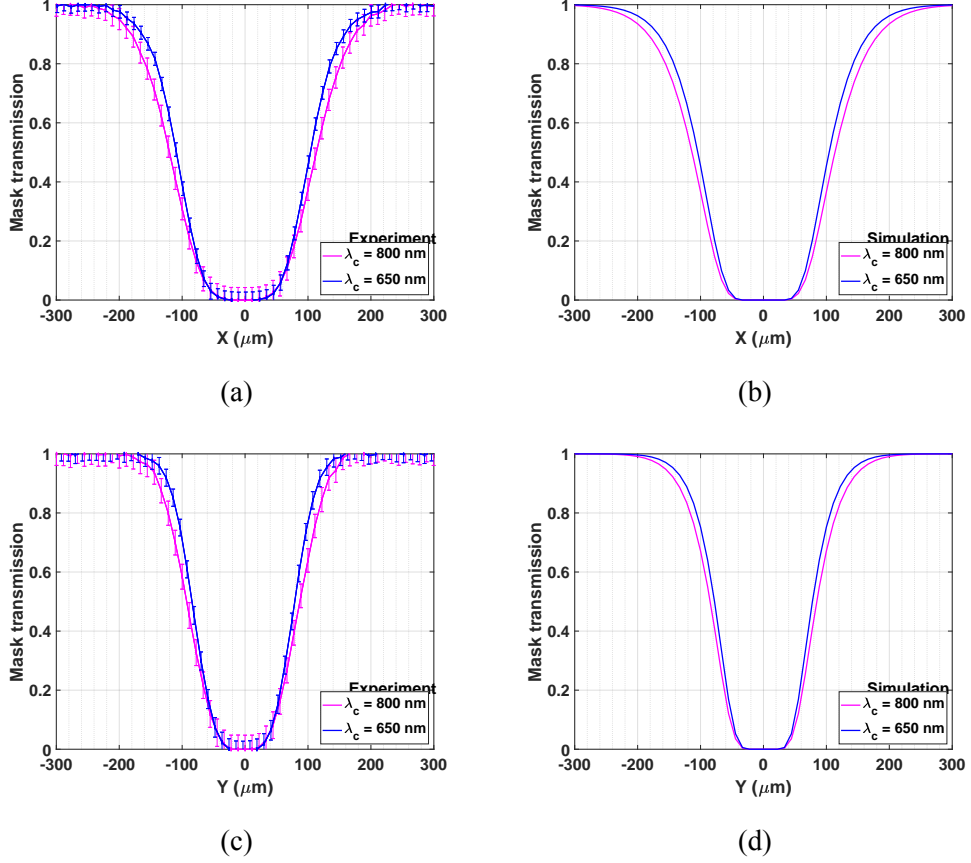


Figure 4.9: Experimental and theoretical mask profiles along the x- and the y-axis at different central wavelengths: $\lambda_1 = 800$ nm (pink curve) and $\lambda_2 = 650$ nm (blue curve). The result confirms with theoretical expectation that the mask will be larger at a longer wavelength.

to 1 pixel. Meanwhile, the quantity $\eta_p(x_o, \lambda)$ is calculated as

$$\eta_p(x_o, \lambda) = \int_{AP(x_o)} PSF_{coro}(x, x_o, \lambda) dx. \quad (4.4)$$

where $PSF_{coro}(x, x_o, \lambda)$ is the PSF recorded at a distance x_o from the mask's center. The assumption here is that PSF_{coro} does not vary over the FOV at distances greater than $7 \lambda/D$ due to the transmission of the mask that is close to 1.

Figure 4.10 illustrates the calculation of raw contrast adapted in this research. The figure on the left shows an image of the star residual irradiance $PSF_{coro}(x, 0, \lambda)$ and the PSF of the companion $PSF_{coro}(x, x_o, \lambda)$ measured at a distance $x_o = 8 \lambda/D$ from the mask center while the right figure shows the cross-sections of the $PSF_{coro}(x, 0, \lambda)$ and

$PSF_{coro}(x, x_o, \lambda)$ as the basis for the calculation of η_s and η_p , respectively.

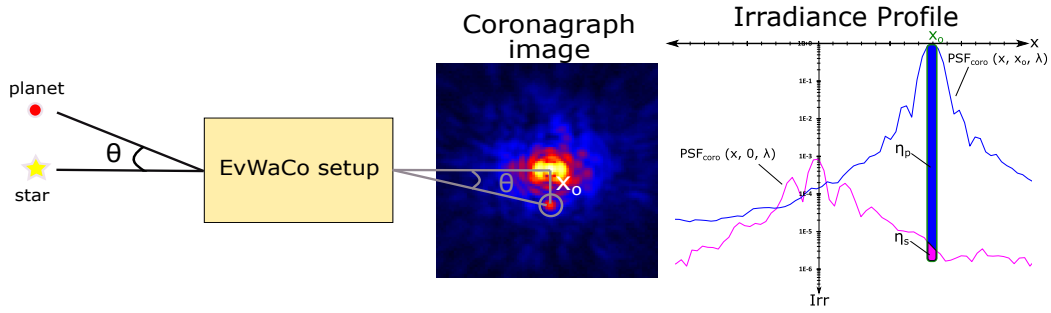


Figure 4.10: Illustration of the raw contrast calculation. The angular separation between the star and the planet is given by θ . The sample coronagraphic image demonstrates the presence of a planet located at a distance, x_o , from the mask center.

The normalized irradiance denoted by, I_{norm} , represents the residual starlight, which is the ratio between the unsaturated off-axis PSF peak and the on-axis PSF. Appendix B discusses the method of calculating I_{norm} from the experimental data. The mask transmission, $T(x, \lambda)$, dictates how much light from the companion can be detected. Thus, the raw contrast will be calculated as

$$C(x, \lambda) = \frac{I_{norm}(x, \lambda)}{T(x, \lambda)}. \quad (4.5)$$

Figures 4.11 and 4.12 show the normalized irradiance obtained using two spectral bands of the Johnson-Cousins photometric filter (Bessel, 1990): I-band and the R-band. The I-band filter has a central wavelength $\lambda_c = 800$ nm with a wavelength range between 700 nm and 900 nm and a spectral ratio $\Delta\lambda/\lambda_c = 20\%$. Meanwhile, the R-band filter has a central wavelength of $\lambda_c = 650$ nm with a wavelength range between 550 nm and 800 nm and a spectral ratio $\Delta\lambda/\lambda_c = 23\%$. During the acquisitions at each bandpass, the filter in front of the camera is replaced while the rest of the setup remains untouched.

To calculate the theoretical raw contrast, the numerical model takes in the following inputs: i) spectral flux incident on the detector (see Figure 4.13), ii) the air gap profile (see Figure 4.7), iii) the diameter of the AS and LS, and iv) the focal length of L2, L3, and L4. The irradiance distribution at the CCD channel is calculated using the formalism presented

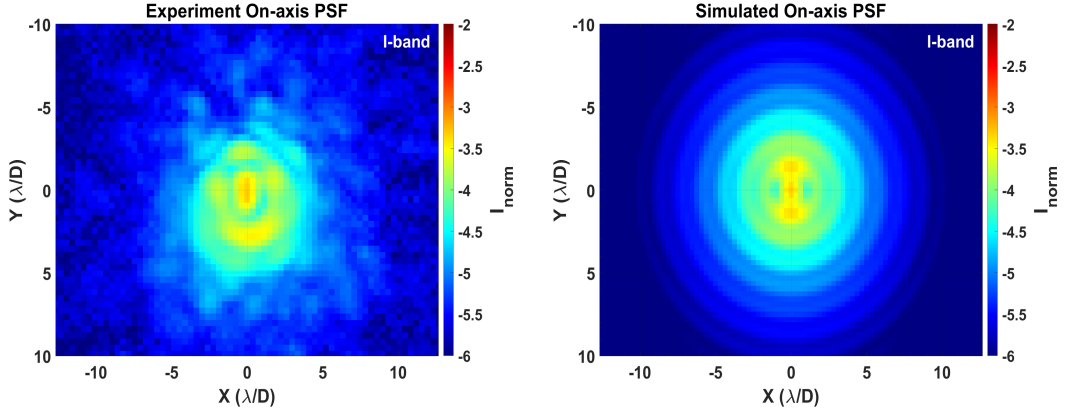


Figure 4.11: Normalized irradiance distribution of the on-axis star over the full I-band: $\lambda_c = 800 \text{ nm}$, $\Delta\lambda/\lambda_C = 20\%$.

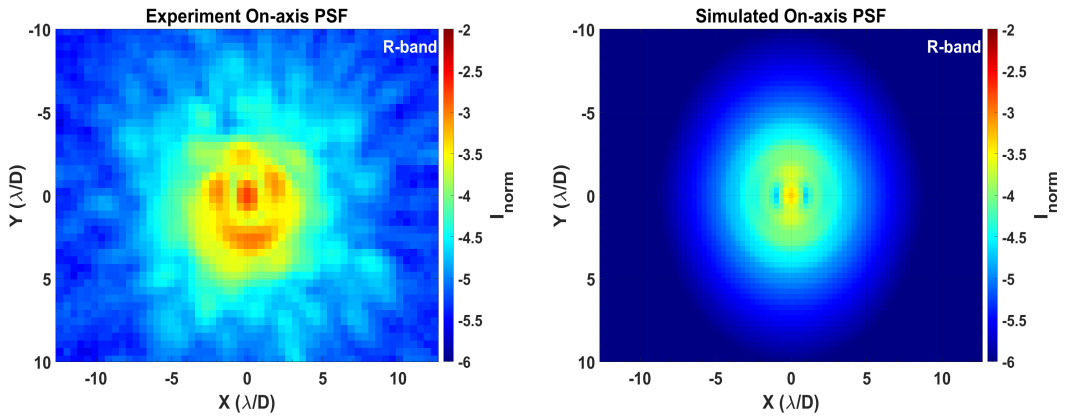


Figure 4.12: Normalized irradiance distribution of the on-axis star over the full R-band: $\lambda_c = 650 \text{ nm}$, $\Delta\lambda/\lambda_C = 23\%$.

in Chapter 2, and more details on the numerical modeling are discussed in Appendix C.

Figure 4.14 shows the average of the raw contrast measured at radial distances between $1.5 \lambda/D$ to $20 \lambda/D$ (pink curve) together with its corresponding spectral response. The PSF peak was suppressed by three orders of magnitude for both spectral bands. Between $3 \lambda/D$ and $4 \lambda/D$, the experimental raw contrast in the I-band varies between $2 \cdot 10^{-4}$ and $5 \cdot 10^{-5}$ while it varies between $2 \cdot 10^{-3}$ and $3 \cdot 10^{-4}$ in the R-band. Meanwhile, along the same distance, the theoretical raw contrast varies between $1 \cdot 10^{-3}$ and $2 \cdot 10^{-4}$ in the I-band and between $3 \cdot 10^{-3}$ and $2 \cdot 10^{-4}$ in the R-band. Between $4 \lambda/D$ and $5 \lambda/D$, the experimental raw contrast in the I-band varies between $5 \cdot 10^{-5}$ and $2 \cdot 10^{-5}$ while it varies between $3 \cdot 10^{-4}$ and $8 \cdot 10^{-5}$ in the R-band. On the other hand, the theoretical raw contrast at the same distance varies between $1 \cdot 10^{-4}$ and $3 \cdot 10^{-5}$ in the I-band and between $2 \cdot 10^{-4}$

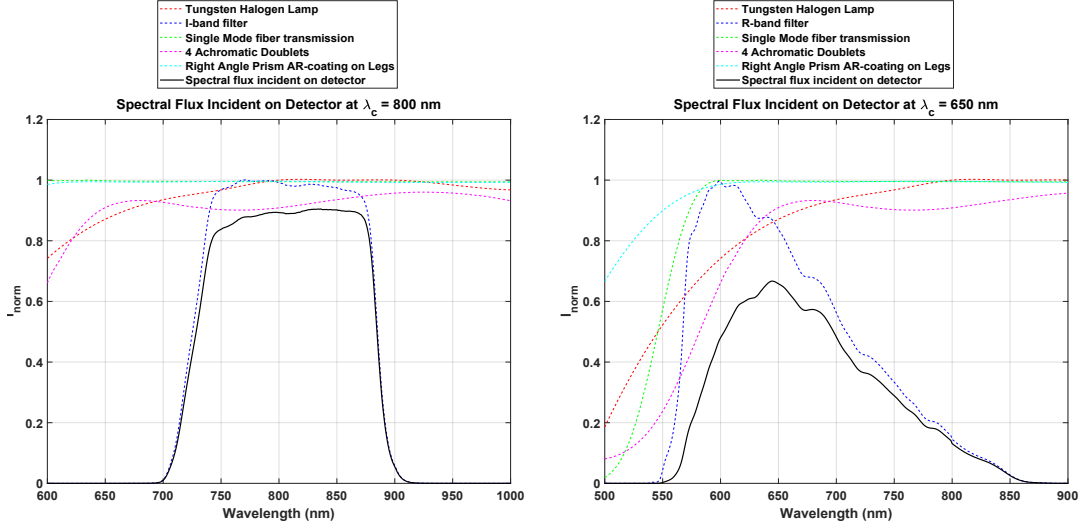


Figure 4.13: Profiles of the spectral flux incident on the detector at $\lambda_c \approx 800$ nm (left) and $\lambda_c \approx 650$ nm (right).

and 4.10^{-5} in the R-band.

The mismatch between the theoretical and the experimental mask transmission may cause this discrepancy. The experimental raw contrast values obtained in the R- and I-band differ by an order of magnitude but the theoretical results are similar, thus confirming the theoretical achromaticity of EvWaCo. In addition, low-order aberrations such as tilt and defocus may contribute to the difference in the experimental raw contrast values between the two passbands.

Between $5 \lambda/D$ and $10 \lambda/D$, the experimental raw contrast decreases from $C \approx 2.10^{-5}$ to $C \approx 3.10^{-6}$ for the I-band and from $C \approx 8.10^{-5}$ to $C \approx 9.10^{-6}$ for the R-band. Along the same distance, the theoretical contrast is between $C \approx 10^{-5}$ to $C \approx 10^{-6}$ for both the I-band and the R-band. The origin of this difference between the experiment and the theoretical contrast could be the presence of speckles in the experimental measurements. Overall, our theoretical results show that the similarity between the I- and R-bands is valid at every radial distance, confirming the theoretical achromatic behavior of the EvWaCo mask in unpolarized light over the two spectral bands.

4.3 Companion Detection

To simulate the detection of a companion, its PSF, 25,000 times fainter than the star, is placed at $5.5 \lambda/D$ distance from the star's center. Figure 4.15 shows the irradiance distribution for the star and the companion with and without the coronagraphic effect. When the star is off-axis, the companion is barely detected in the star's blinding light. However, the companion becomes visible once the star is centered on the coronagraphic mask.

Background noise due to star residual noise, speckle noise, stray light photon noise, detector thermal noise, and readout noise, may contaminate the companion signal, thus, it needs to be extracted. The background noise can then be calculated by taking the standard deviation, $\sigma_{Background}$, over an annular region starting with an inner radius $R1 = 2.5 \lambda/D$ and an outer radius, $R2 = 3.5 \lambda/D$. This calculation is repeated over an annular region with inner radii equal to 3.5, 4.5, ..., 19.5 λ/D , with an annular width always kept at 1 λ/D . Between 3 λ/D and 10 λ/D from the center of the mask, the background noise varies from $\sigma_{Background} \approx 3 \cdot 10^{-5}$ to $\sigma_{Background} \approx 10^{-6}$. At distances greater than 10 λ/D , this noise decreases from $\sigma_{Background} \approx 10^{-6}$ to $\sigma_{Background} \approx 10^{-7}$.

The companion is considered to be detected if the signal-to-noise ratio (SNR) is ≥ 5 . The $\sigma_{Background}$ at the companion's location x_o is calculated by taking the standard deviation of a circle with a radius equal to 1 λ/D , centered at x_o . It is estimated that the SNR at this location is equal to 11.

4.4 Repeatability and stability

Measurements obtained over eight months were analysed to determine the repeatability and stability of the coronagraph's performance. The pressure between the lens and the prism was not adjusted but for each measurement, both the position of the PSF and the Lyot stop were re-centered each time to ensure a high performance.

Figure 4.16 shows the residual light's x- and y- profiles on the I-band and the black curve represents the average of these measurements. Despite measuring at different dates, the overall shape of the profile remains the same. Figure 4.17 shows the radial average

of the curves for 10 sets of measurements. At the location of the shortest IWA, the average normalized irradiance is $I_{norm} \approx 10^{-4}$. The average normalized irradiance is equal to $I_{norm} \approx 6.10^{-5} \pm 1.10^{-5}$ at $3.5 \lambda/D$, $I_{norm} \approx 3.10^{-5} \pm 7.10^{-6}$ at $4.5 \lambda/D$ and $I_{norm} \approx 2.10^{-5} \pm 5.10^{-6}$ at $5.5 \lambda/D$. These measurements were obtained in-air without any adaptive optics.

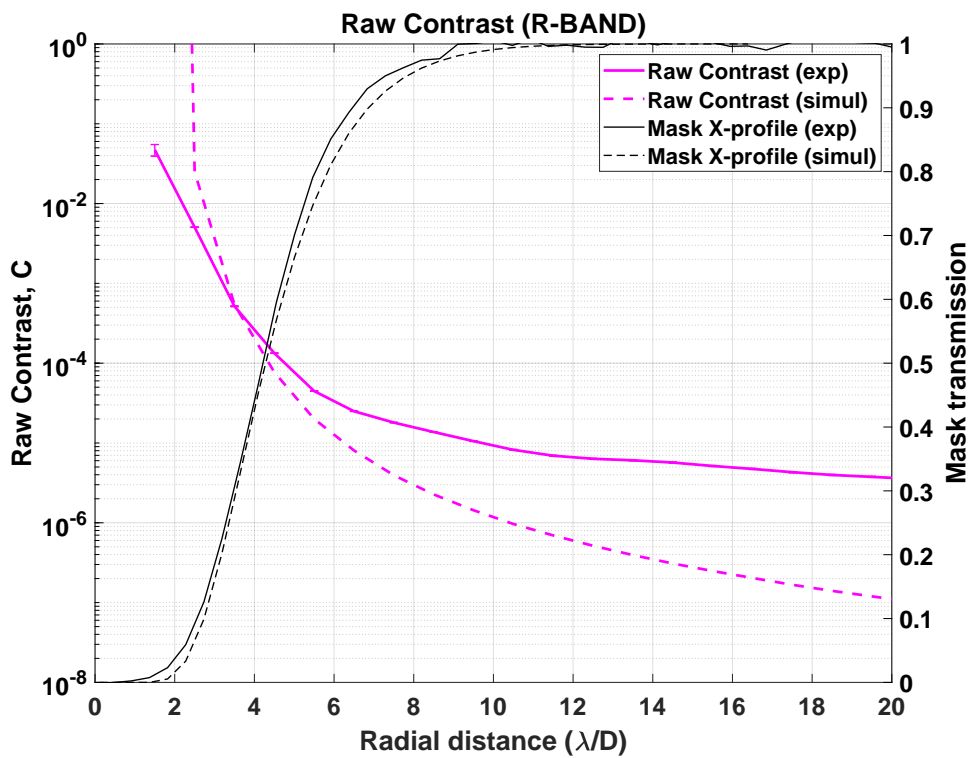
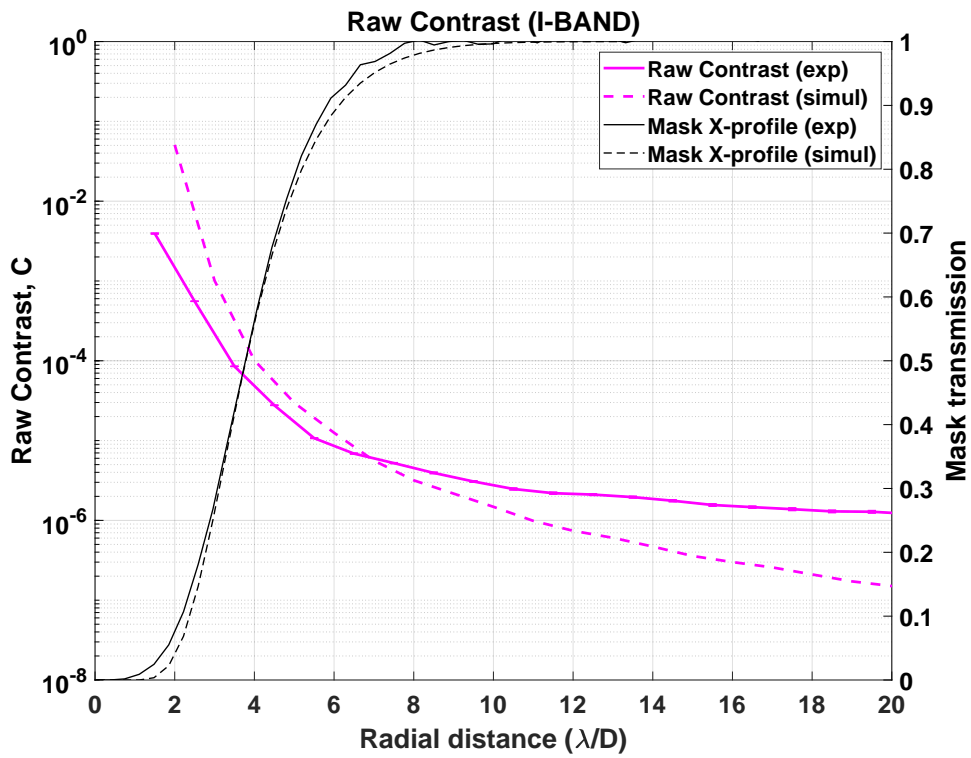


Figure 4.14: Calculated raw contrast for each passband obtained experimentally and numerically.

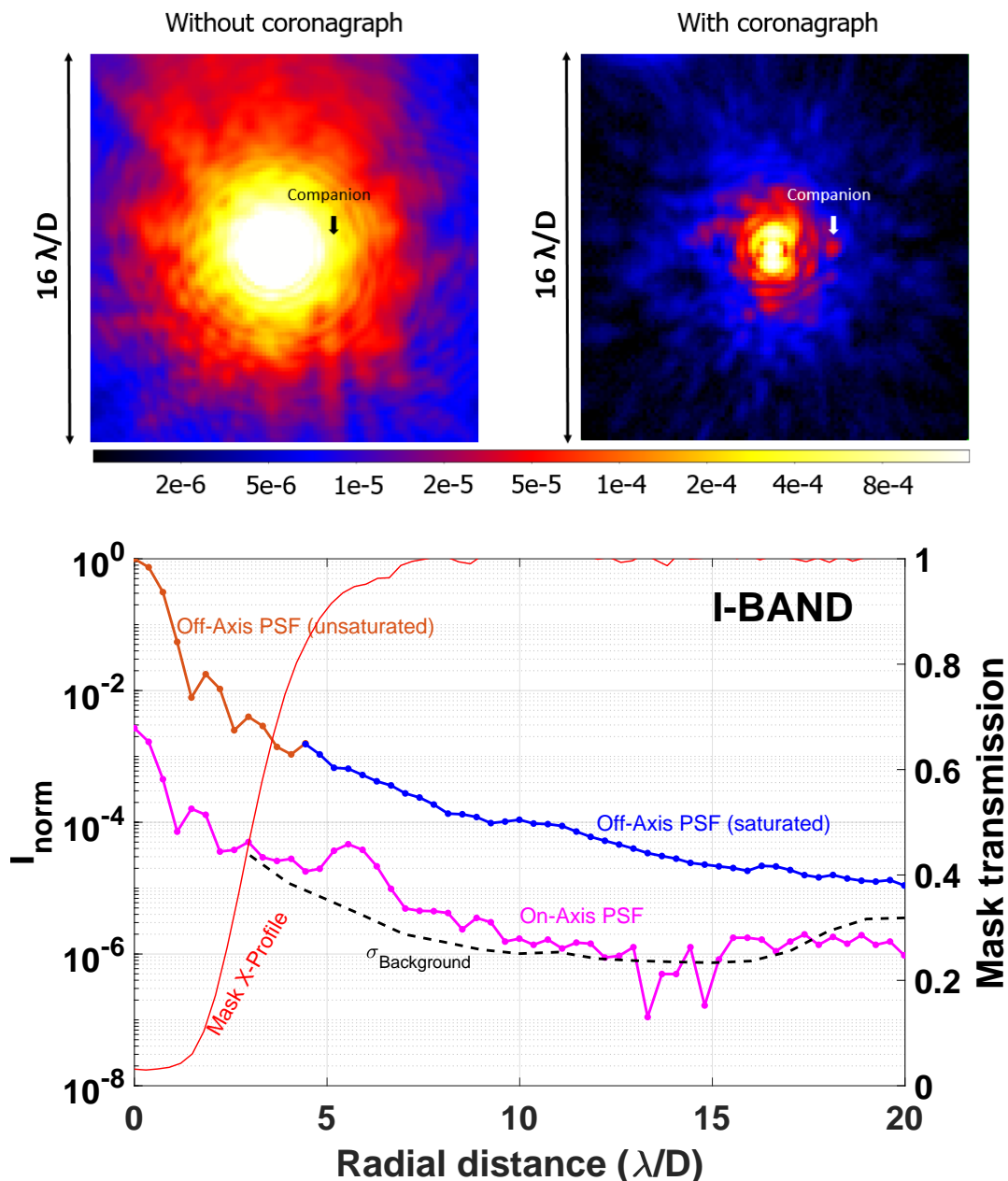


Figure 4.15: Irradiance distribution of the star with a companion, 25000 times fainter than the star, located at $5.5 \lambda/D$ from the star center, without the coronagraph (first figure), with the coronagraph (second figure), and the corresponding cross-section of the coronagraphic image (third figure). This experiment was obtained using an LED emitting at $\lambda_C = 780$ nm with a spectral ratio $\Delta\lambda/\lambda \approx 3.2\%$ serving as the companion source. The final images shown here are a median of 101 calibrated science images obtained at an integration time of 1 s per frame. The companion can be detected with an SNR of 11.

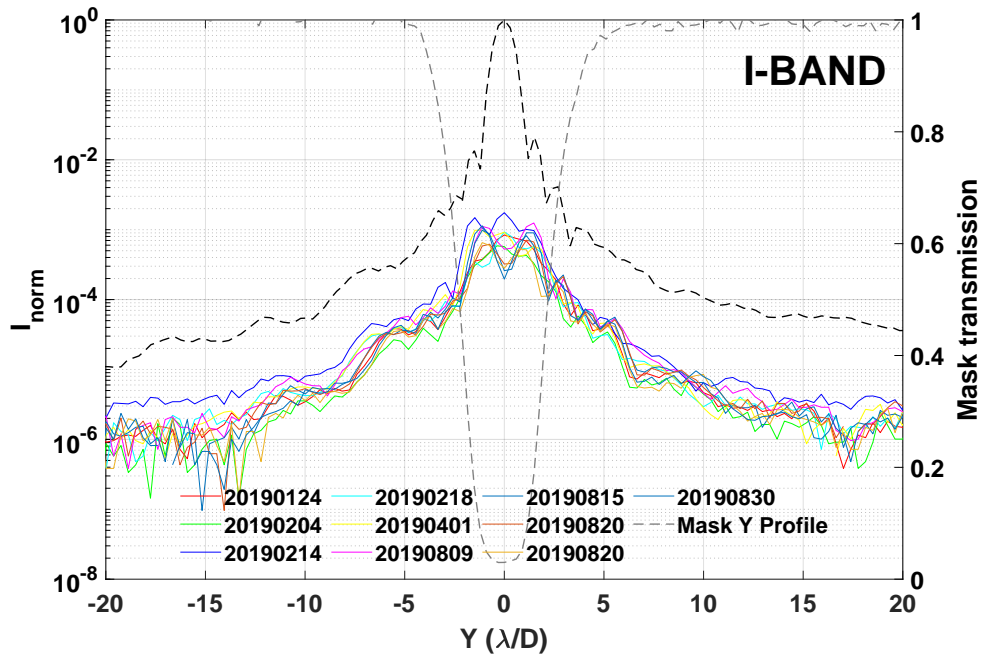
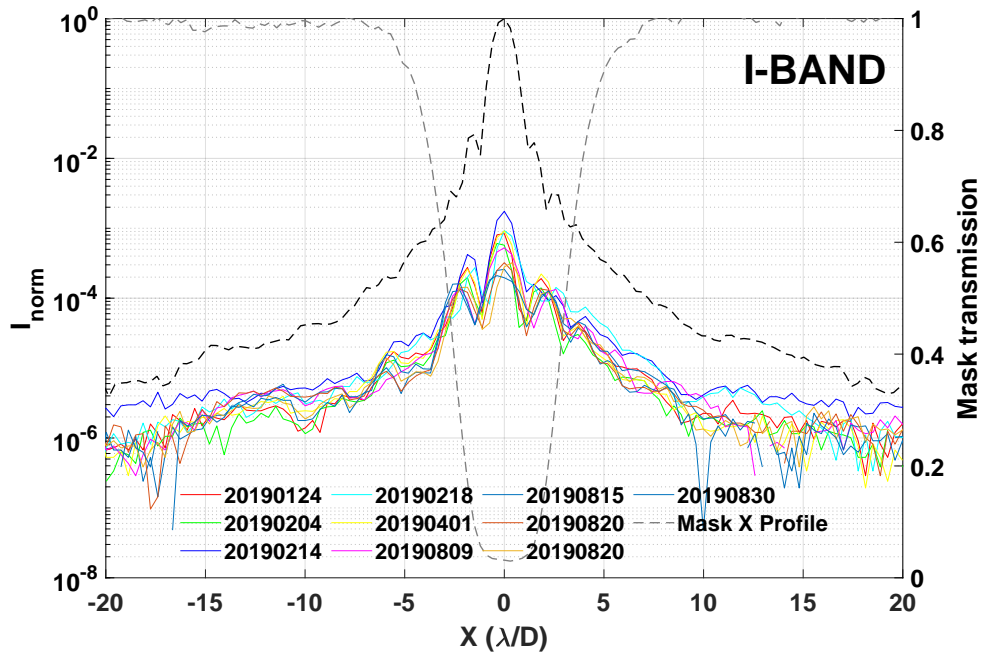


Figure 4.16: Cross-section along the x-axis and the y-axis of the PSF images obtained over the full I-band in unpolarized light. The different colors represent 10 normalized irradiance measurements done over eight months.

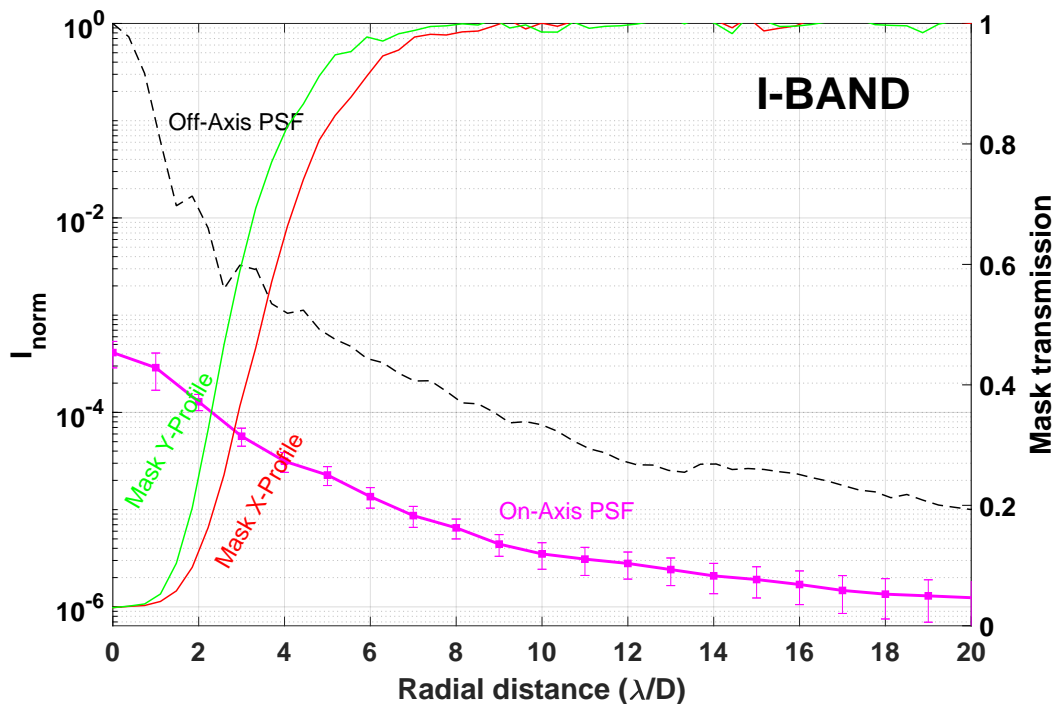


Figure 4.17: Radial average of the normalized irradiance and the corresponding standard deviation of the 10 contrast measurements. At the location of the IWA, the average normalized irradiance is approximately equal to $I_{norm} \approx 6 \cdot 10^{-5} \pm 1 \cdot 10^{-5}$ at $3.5 \lambda/D$, $I_{norm} \approx 3 \cdot 10^{-5} \pm 7 \cdot 10^{-6}$ at $4.5 \lambda/D$ and $I_{norm} \approx 2 \cdot 10^{-5} \pm 5 \cdot 10^{-6}$ at $5.5 \lambda/D$.

4.5 Sensitivity Measurements

4.5.1 Variation of the normalized irradiance due to tip-tilt

It is critical to properly center the PSF on the focal plane mask, as even a small amount of starlight leakage can contaminate the faint companion signal. The variation of the contrast performance due to tilt was done by installing a pointing camera. For these measurements, a beamsplitter is temporarily installed right after the aperture stop so that the reflected beam is focused by the lens L5 on a Point Grey Camera with a pixel size of $3.4 \mu m$, as shown in Figure 4.18, allowing us to measure how much tilt was introduced to the optical path.

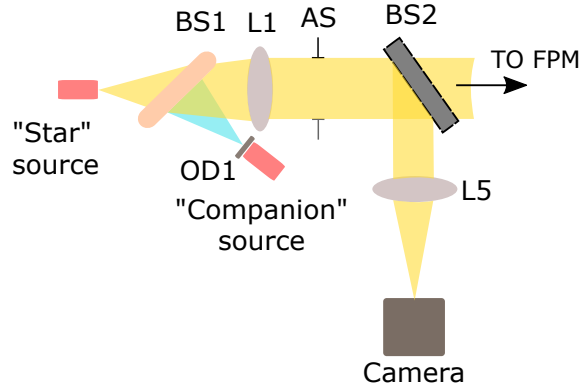


Figure 4.18: Setup for measuring the tilt introduced in the setup. To measure how much tilt is introduced in the setup, we measured how the PSF shifts in the camera to the reference position.

The PSF is first centered on the mask to serve as a reference. Then, the star source fiber is displaced to introduce tilt, which is equivalent to de-centering the PSF on the FPM. Figures 4.19 and 4.20 show the cross-section of the irradiance distribution recorded at the companion channel CCD. The tilt is expressed in terms of λ/D where D is equal to the diameter of the aperture stop, and the error bar corresponds to the standard deviation of the contrast values calculated from the 101 images obtained for each tilt.

Along the x-axis, the normalized irradiance at the IWA is better than 10^{-4} when the tilt is smaller than $\theta_x < 1 \lambda/D$. Meanwhile, the normalized irradiance at $5 \lambda/D$ and $6 \lambda/D$ show only slight variations. At $\pm 3 \lambda/D$, the normalized irradiance y-profile shows an asymmetry, which could be because the PSF position set as the reference is slightly

shifted along the y-axis. Despite that, it can be deduced from Figure 4.20 that normalized irradiance is better than 10^{-4} for tilt angles smaller than $\theta_Y < 0.2 \lambda/D$.

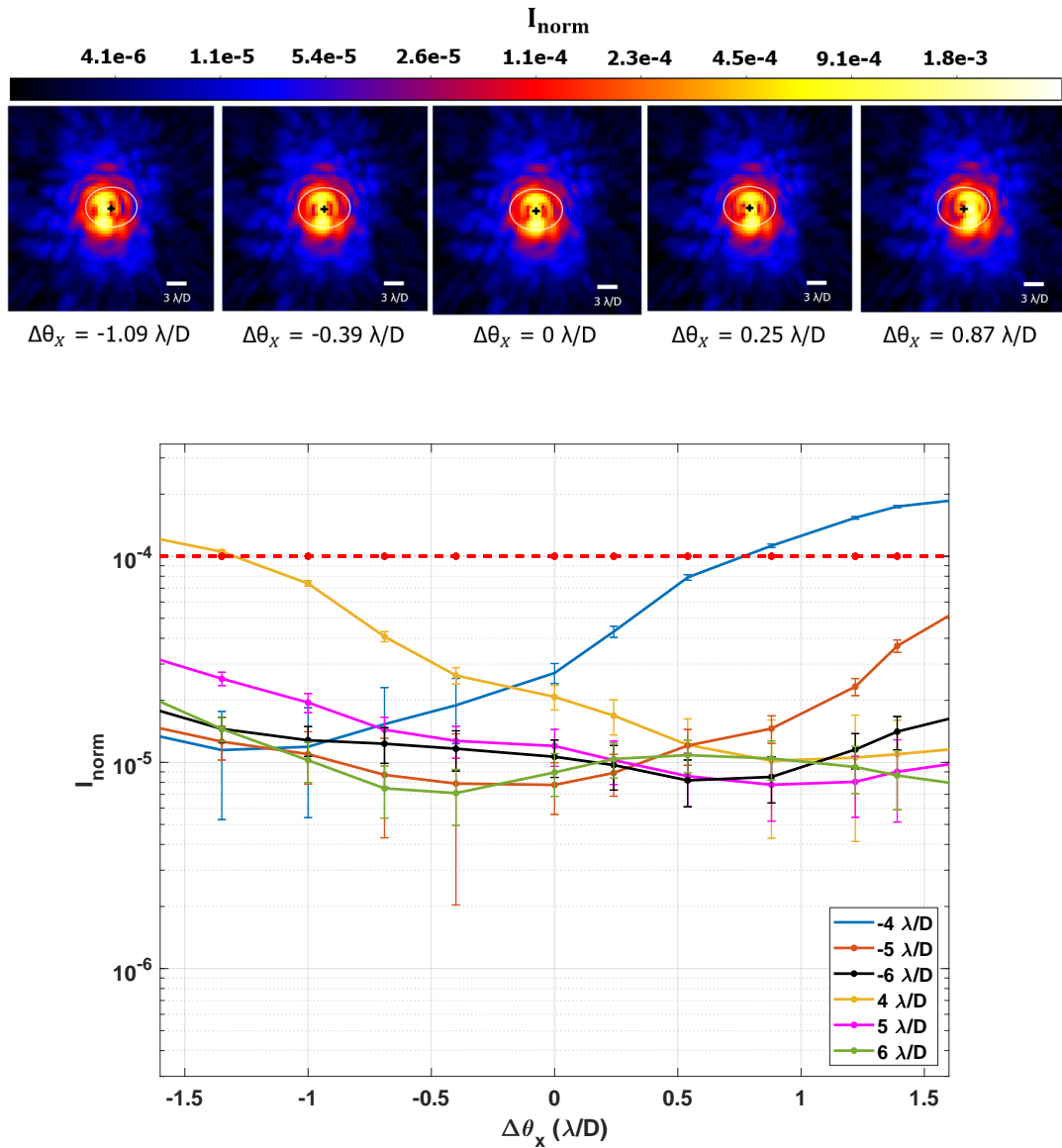


Figure 4.19: Coronagraphic images at varying levels of tilt introduced along the x-axis. The center of the mask is marked by the black cross, and the location of the IWA is represented by the ellipse. The images have the same brightness scale.

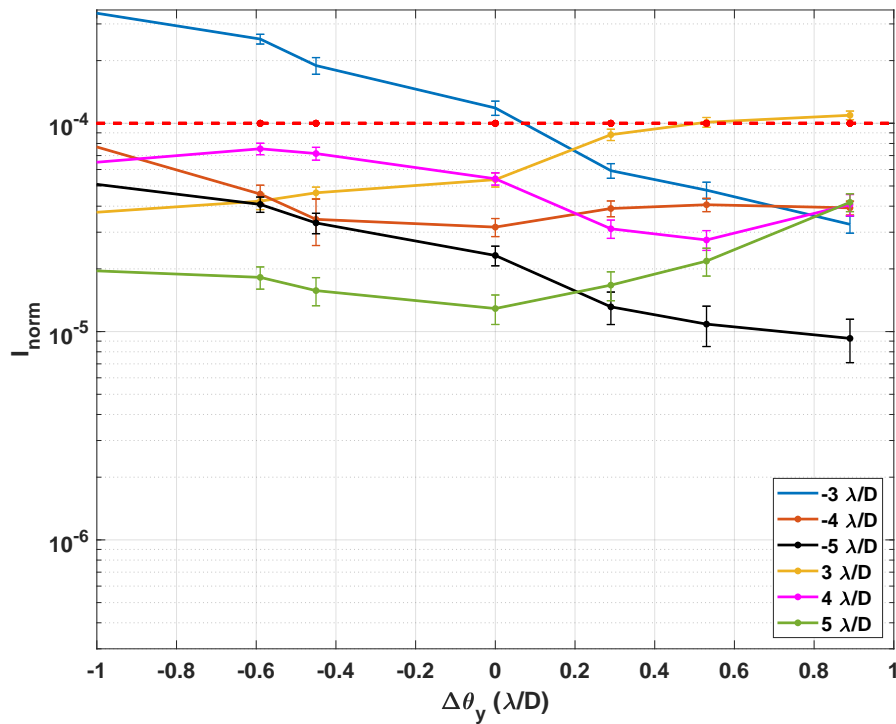
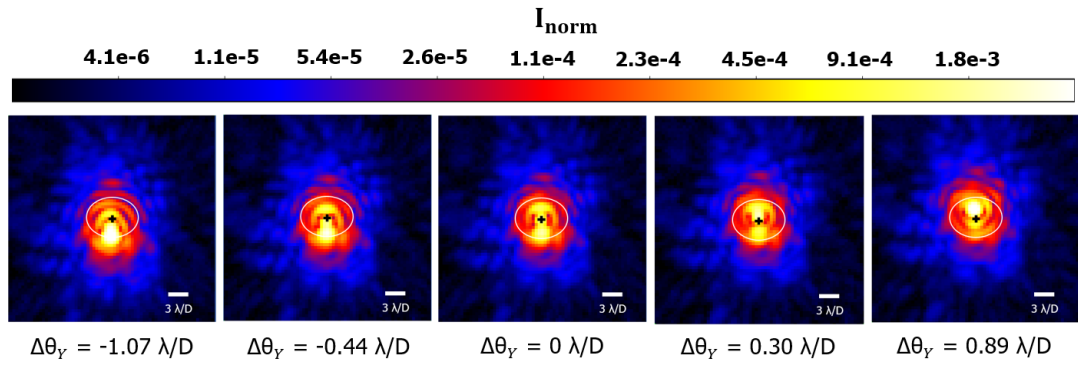


Figure 4.20: Coronagraphic images at varying levels of tilt introduced along the y-axis. The center of the mask is marked by the black cross, and the location of the IWA is represented by the ellipse. The images have the same brightness scale.

4.5.2 Variation of the normalized irradiance due to the defocus

To simulate the coronagraphic performance due to defocus, the star source is displaced along the optical axis. This displacement is expressed in terms of the PTV (peak-to-valley) wavefront error. Zemax was used to calculate the PTV wavefront error induced by each displacement (see Figure 4.21). The Zemax model consists of a point source collimated by a lens. The lens is displaced to simulate a defocus, and the wavefront error is calculated after the aperture stop, which is located one focal length away from the lens. The corresponding wavefront error of λ PTV induced for each displacement is presented in Figure 4.22. One hundred one images were acquired for each displacement, and the normalized irradiance values are calculated over a circular annulus with an extension of $1 \lambda/D$. The error bars are calculated from a standard deviation of the 101 images. At $3 \lambda/D$ from the center of the mask, the normalized irradiance values are better than 10^{-4} for a wavefront less than 0.65λ PTV. This is expected since EvWaCo has a long depth of focus. However, if the IWA is smaller than $3 \lambda/D$, the effect of this amount of defocus will result in a significant starlight leak.

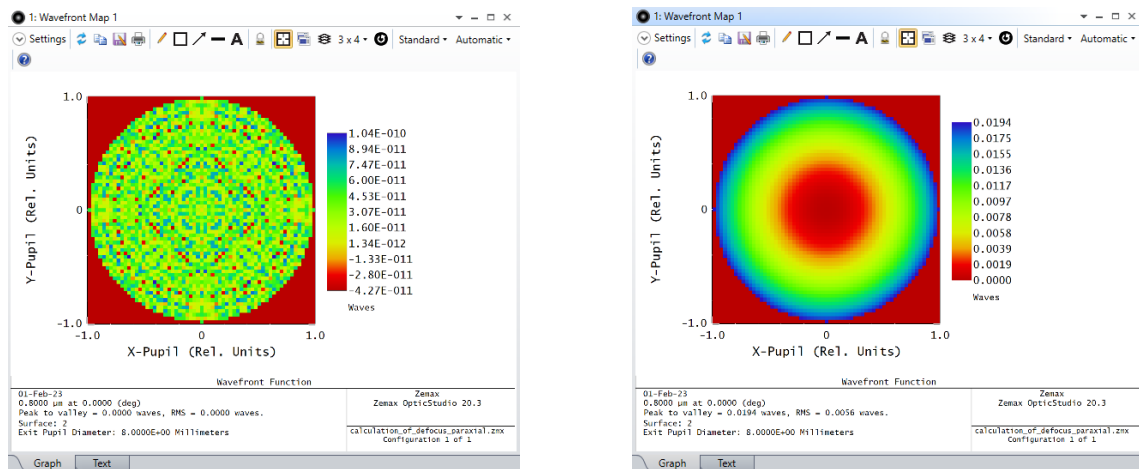


Figure 4.21: Wavefront map calculating Zemax for a setup without introducing a defocus and after displacing the star source by $200 \mu\text{m}$.

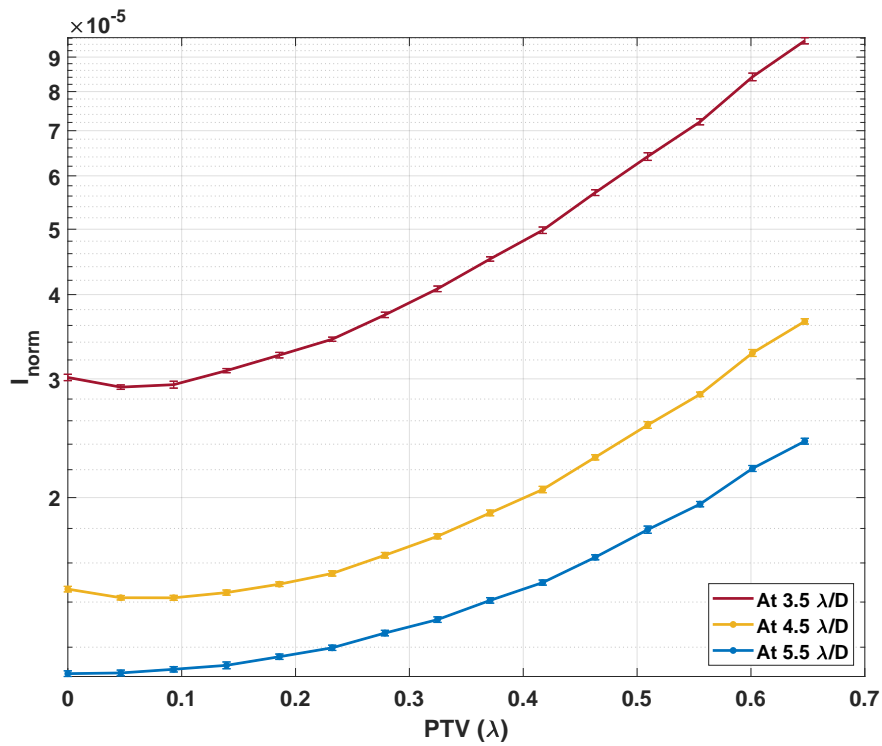
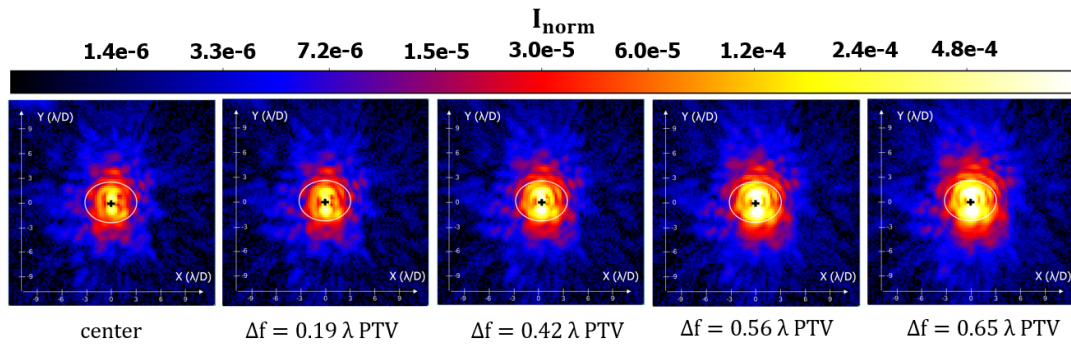


Figure 4.22: Normalized irradiance at specific radial locations from the center of the mask: $3.5 \lambda/D$ (red curve), $4.5 \lambda/D$ (yellow curve), and $5.5 \lambda/D$ (blue curve) expressed in terms of $\lambda \text{ PTV}$.

4.5.3 Variation of the normalized irradiance due to Lyot stop misalignment

The Lyot stop plays an important role of reducing the residual starlight that reaches the detector. Otherwise, the uncontrolled starlight leakage could degrade the coronagraph performance. The Lyot stop was intentionally misaligned along the x- and the y-directions to determine the lateral misalignment that can be tolerated. Figures 4.23 and 4.24 show how the contrast varies when the Lyot stop is not precisely positioned at the center of the exit pupil (EP) as represented by the black circle.

Figure 4.23 reveals that misalignment of $74 \mu\text{m}$ ($0.02 D_{EP}$) along the x-direction does not significantly impact the normalized irradiance at the location of the IWA ($IWA_X \approx 4.00 \lambda/D$, $IWA_Y \approx 3.00 \lambda/D$). A similar behavior is observed for a misalignment of $84 \mu\text{m}$ ($0.02 D_{EP}$) along the y-direction as shown in Figure 4.24. These results show the possibility of enlarging the Lyot stop to 90% the pupil diameter size (currently, it is at 81%) which starts to be a tighter tolerance.

4.6 Raw Contrast at different mask pressure

Figure 4.25 shows the experimental raw contrast obtained at varying mask IWA. So far, the best raw contrast performance was reached using a mask with the smallest IWA (minimum pressure) (Alagao et al., 2021b).

The transmission profile of the FPM resembles a Gaussian only when the IWA is small, such as when it was set to $3 \lambda/D$ (minor axis). As mentioned in Chapter 2, Gaussian masks provide an apodization of the Airy wings that contaminate the planet's faint signal. Meanwhile, larger-pressure masks have a transmission that resembles a top-hat profile.

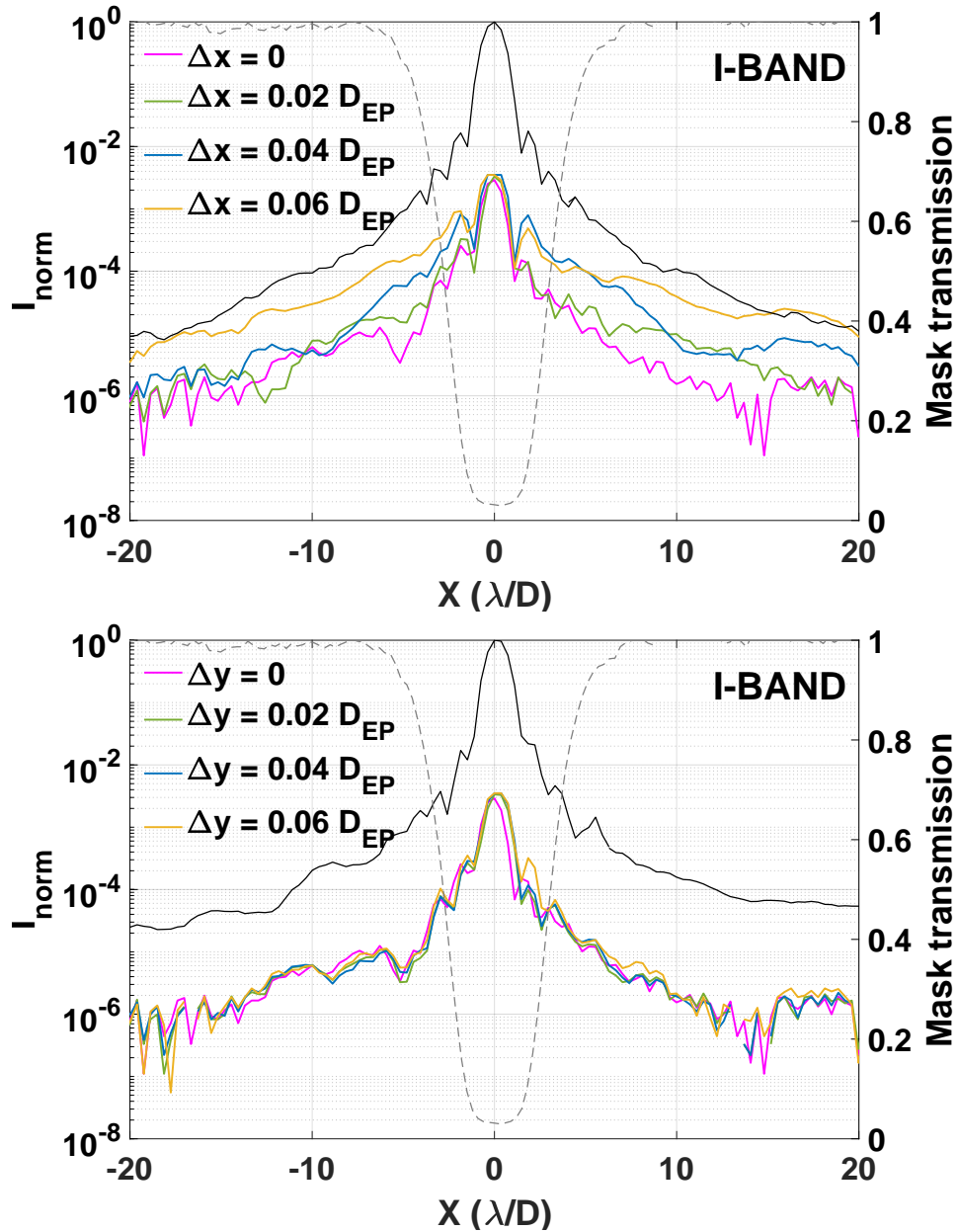
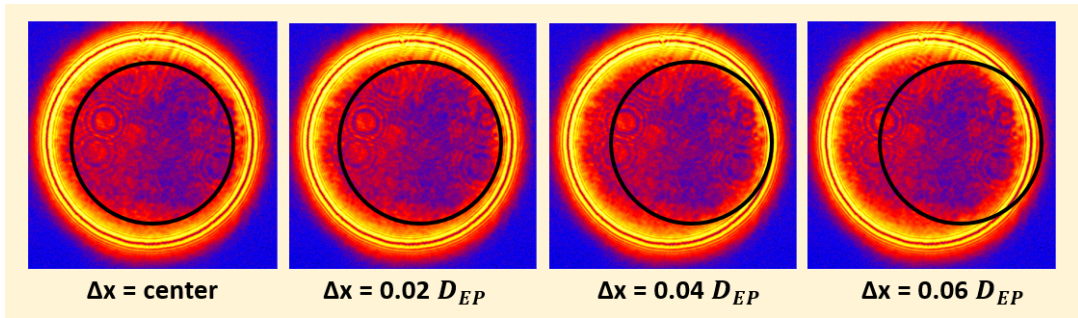


Figure 4.23: Normalized irradiance for each corresponding LS (black circle) misalignment along the x-axis. A misalignment of up to $74 \mu\text{m}$ ($0.02 D_{EP}$) does not significantly affect the normalized irradiance at the $IWA_X \approx 4.00 \lambda/DV$

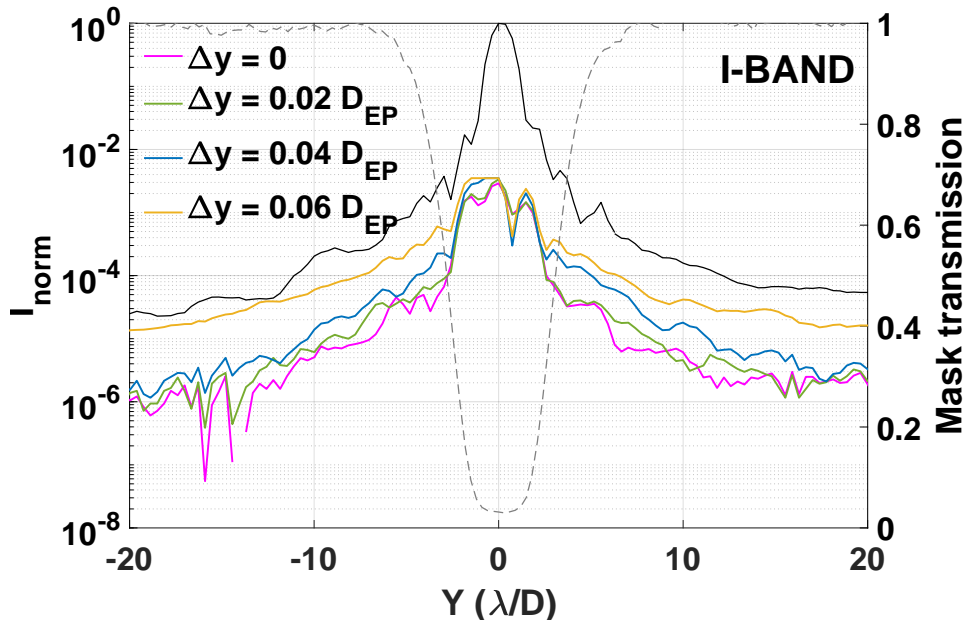
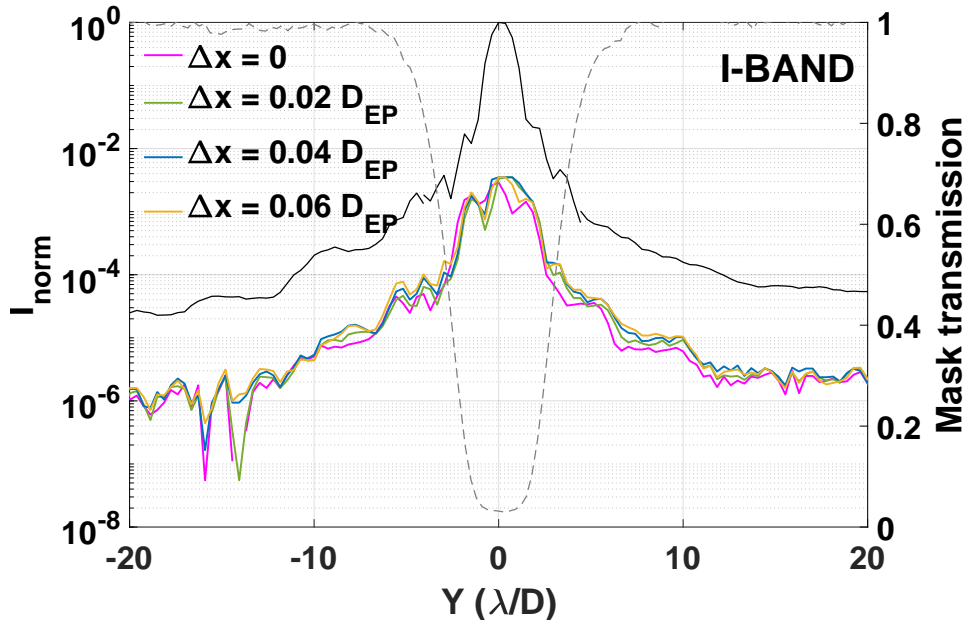
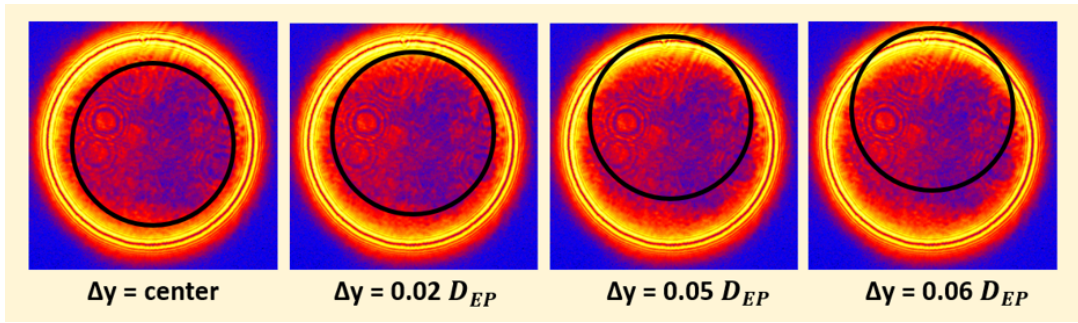


Figure 4.24: Normalized irradiance for each corresponding LS (black circle) misalignment along the y-axis. A misalignment of up to $84 \mu\text{m}$ ($0.02 D_{EP}$) does not significantly affect the normalized irradiance at the $IWA_X \approx 3.00 \lambda/D$.

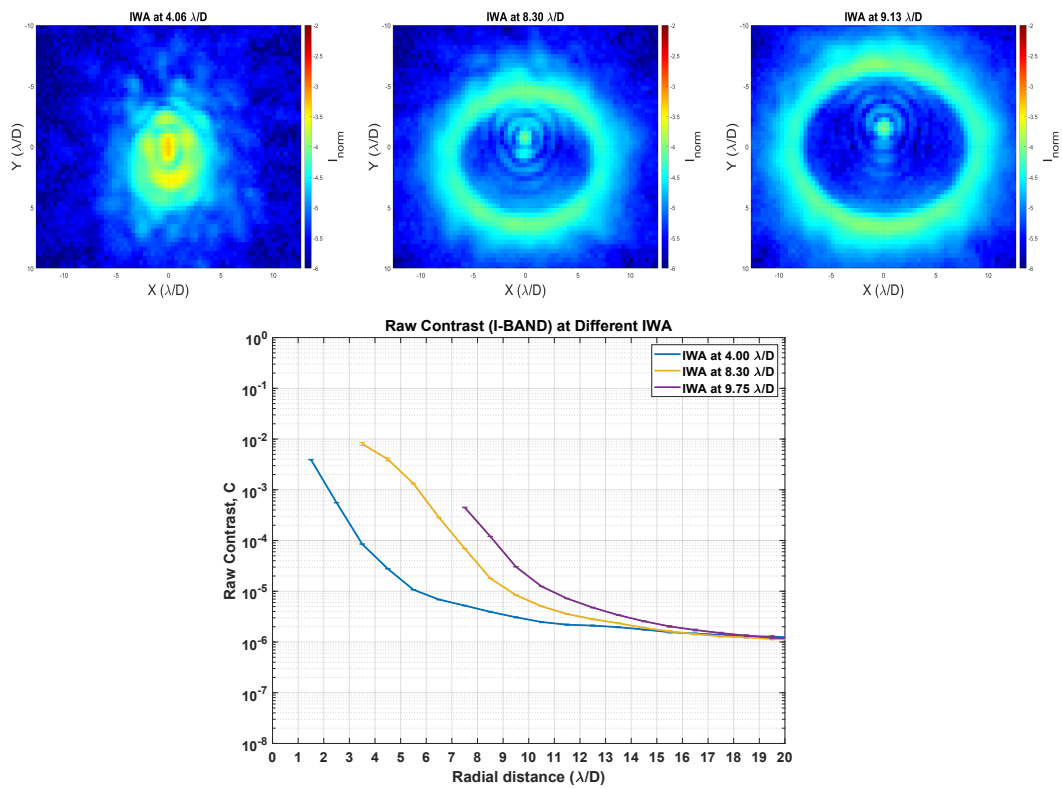


Figure 4.25: [Top] 2D normalized irradiance distribution of the on-axis star over the full I-band at different IWA. [Bottom] Radial average of the raw contrast curves. Refer to Figure 5 for the mask response at each IWA. (Alagao et al., 2021b)

4.7 Summary

The upgraded focal plane mask demonstrated that the size can be easily increased, if needed, without further modifications to the setup. It was also shown that the achromatic properties of the mask are best exhibited at the smaller inner working angles of the mask. This setup was shown at $IWA \approx 3 \lambda/D$ along the mask minor axis. This is a significant improvement from the results presented in (Alagao et al., 2017), where the diameter of the mask did not vary linearly with the wavelength.

The closest approximation of the air gap shows that the raw contrast at the IWA is approximately 10^{-4} . Although the experimental results are not exactly similar, the theoretical results demonstrated the achromatic rejection over the full I-band and R-band at the IWA.

Measurements aiming to reproduce the results show that the results are repeatable and stable. However, it must be noted that these measurements are on a passive setup, and it only requires centering and de-centering the PSF on the mask. It did not undergo any rigorous testing, such as vibration testing.

In terms of sensitivity to aberrations, due to the asymmetry of the mask, it is more sensitive to tilt along the direction of the minor axis. In particular, it can tolerate a tilt of $\theta_y \approx 0.2 \lambda/D$ and $\theta_x \approx 1 \lambda/D$. In terms of defocus, it can tolerate a wavefront error of less than 0.65λ PTV. Meanwhile, the tests for coronagraph performances suggest that the Lyot stop diameter can be enlarged up to 90%, thereby increasing the throughput; however, it will come at the expense of tighter tolerance for Lyot stop alignment. Finally, a simulated companion, placed at $5.5 \lambda/D$, 25,000 times fainter than the star, can be detected at an $SNR > 5$ in the laboratory setting without adaptive optics.

CHAPTER 5

Optimization

One of the important results of the previous chapter is the raw contrast at varying inner working angles. It demonstrated that the smallest inner working angle ($\approx 3 \lambda/D$ along the mask minor axis) yielded the best raw contrast performance. This chapter presents my further investigation of the question: What is the smallest IWA that can be attained using the EvWaCo focal plane mask with an acceptable performance?

5.1 Improving the estimation of the air gap

Later in the study, we found out that the approximation of the air gap can be improved by dividing the coefficients by a constant, x_o , using the following equation:

$$d(m) = \max\left(\sum_{n=0}^3 a_n \left(\frac{x}{x_o}\right)^n, 0\right), \quad (5.1)$$

where a_n represents the coefficient of the polynomial of degree n , and x_o is the distance from the center of the contact area where the mask transmission is 0.5. Adding all the coefficients will give the corresponding air gap at that distance.

Recalculating the coefficients of the polynomial Equation in 5.1, the following coefficients for our mask with an IWA of $3 \lambda/D$ along the minor were obtained: $a_0 = 1.4808 \times 10^{-9}$ m, $a_1 = 8.0244 \times 10^{-8}$ m, $a_2 = -3.7319 \times 10^{-9}$ m, and $a_3 = 1.5494 \times 10^{-7}$ m. These coefficients yield the mask profiles shown in Figure 5.1 showing that both the experimental and the simulated mask profiles fit provided a good match, especially at the region close to the contact area. This is a significant improvement in the approximation of the air gap presented in Chapter 4. Adding these coefficients tells us the air gap where the mask reached a transmission of 0.5 or its half width at half maximum (HWHM). The smallest mask reached its FWHM when the air gap was approximately $d = 2.3293 \times 10^{-7}$

m or 233 nm at $x_o = 100$ microns.

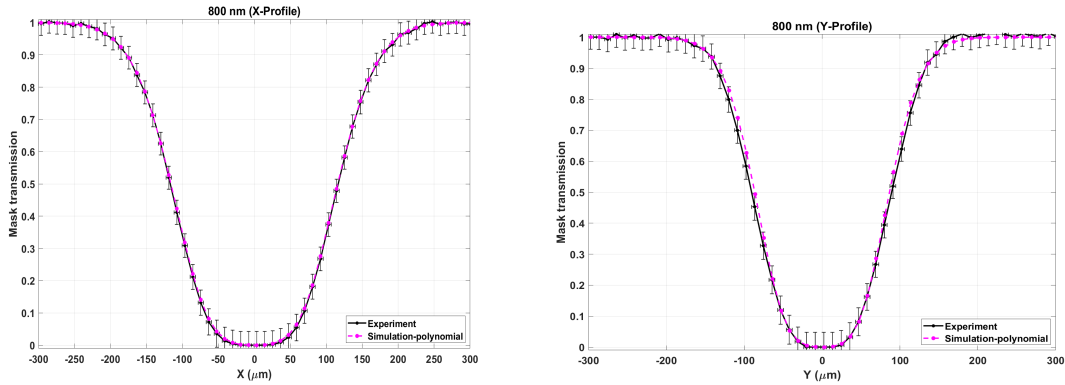


Figure 5.1: Comparison between the theoretical and measured mask response along the major axis of the mask (x-axis) and the minor axis (y-axis) using the new air gap approximation. The error bars along the horizontal axis equal ± 1 pixel. Meanwhile, the error bars along the vertical axis are the standard deviation of the irradiance value from the 101 flat-field images obtained at the time of the acquisition of the experimental data. Unlike the previous estimation of the air gap, this time, the experiment and simulation perfectly match, especially close to the contact area.

The same polynomial equation calculates the air gap for a larger mask, such as the one with an IWA at $9.13 \lambda/D$. The calculated coefficients are: $a_0 = -2.0554 \times 10^{-7}$ m, $a_2 = -2.2493 \times 10^{-6}$ m, $a_2 = 3.6322 \times 10^{-6}$ m, and $a_3 = -8.5237 \times 10^{-7}$ m at $x_o = 250$ microns, the HWHM of the mask. The sum of these coefficients yields $d = 3.2497 \times 10^{-7}$ m or approximately 325 nm.

Figure 5.2 shows the estimated air gap (first row) and their corresponding mask reflection profiles. Using the same Equation 5.1 yielded mask reflection profiles where both the experiment and the simulation perfectly match. It is also important to note that at the location of the mask FWHM, the estimated air gap for each mask is less than the source wavelength, which is 800 nm. The penetration depth - distance from the boundary where the strength of evanescent waves decreases to $1/e$ of the original value - at this wavelength is close to 850 nm for an incident angle close to 42° . Recall that the critical angle is 41.45° .

The mask profiles highly depend on the air gap. The sharp change in the air gap resulted in an almost top-hat profile, while having a smoother transition farther from the contact area resulted in the achromatic rejection. This smooth transition in the air gap is

the key to the apodization process of the PSF wings at the mask FPM plane.

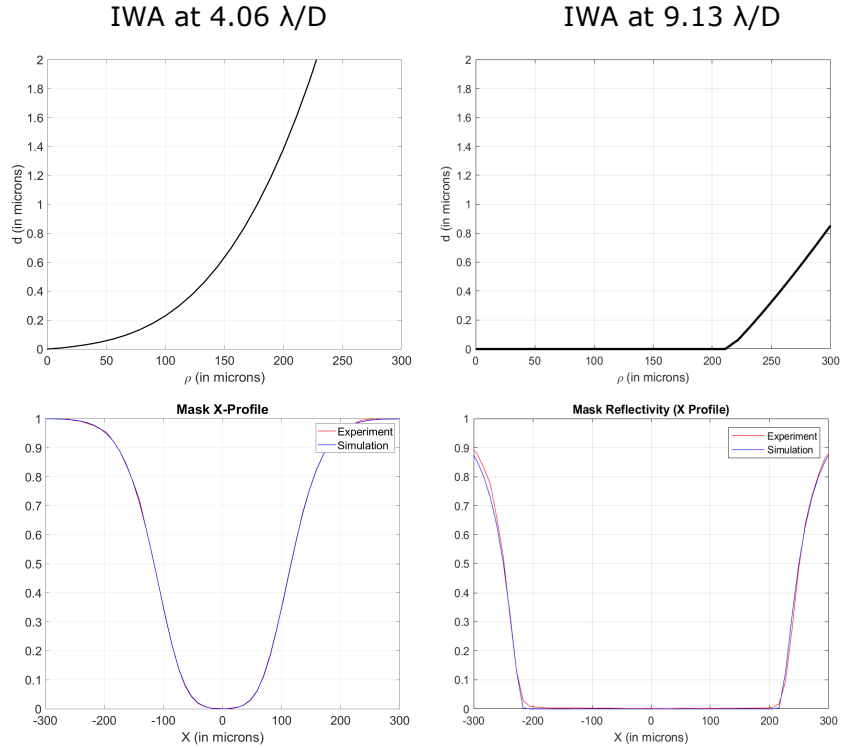


Figure 5.2: Calculated air gap at different mask IWA generated using the Equation 5.1. The mask profiles below show that the experiment and the simulations match very well, implying that the estimated air gap may exactly represent the air gap during the experiments.

5.2 Optimizing the performance using a Gaussian apodizer

As mentioned in Chapter 2, another method for optimizing the performance of a Lyot coronagraph is by modifying the amplitude of the pupil plane. A simple example is by using a Gaussian apodizer. Using the current focal plane mask with the small IWA, the Gaussian apodizer is designed so that its FWHM matches the FWHM of the mask profile using the following expression at the entrance pupil:

$$P(\xi, \eta) = Ae^{\frac{\xi^2}{2\sigma_\xi^2} + \frac{\eta^2}{2\sigma_\eta^2}} \quad (5.2)$$

where $\sigma_\xi^2 = 0.023$, and $\sigma_\eta^2 = 0.023$. Figure 5.3 (left) shows how this value was obtained. The same method used to obtain the coefficients of the air gap in Chapter 4,

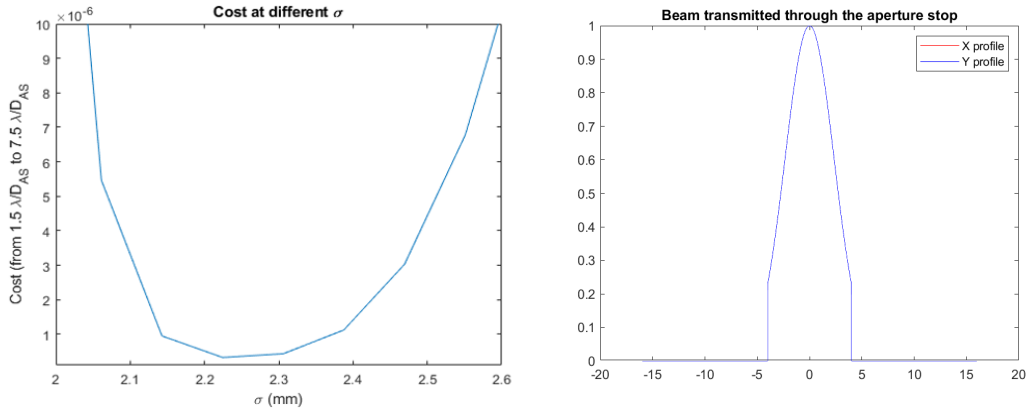


Figure 5.3: (Left) Cost values (Sum squared difference between the model and target) at varying values of σ . (Right) Cross-section of the irradiance distribution at the entrance pupil after passing through the Gaussian apodizer. The apodizer transmits approximately 23% of light through its edges.

the optimization toolbox was also used to find the minimum cost: $Cost = \sum (Model - Target)^2$, where the model is the current calculation of the raw contrast. Target assumes zero residual starlight between the distances $1.5 \lambda/D$ and $7.5 \lambda/D$. This results in a Gaussian aperture that transmits approximately 23% through its edges.

Figure 5.4 shows the irradiance distribution at the important planes after adding an apodizer. This calculation uses the model described in Appendix C. The apodization is done only at the aperture stop. Normalized irradiance distribution profiles at the CCD plane in Figure 5.5 show that the signal has been attenuated by an order of magnitude at the wings of the PSF.

Due to the asymmetry of the mask, the calculation of the raw contrast will be revised as illustrated in Figure 5.6. The previous chapter assumes a circular annulus in calculating the radial average of the raw contrast. This time, an elliptical annulus will be implemented to compare the simulation and experimental raw contrast.

Figure 5.7 shows that the experimental and simulated raw contrasts agree, especially at distances less than the inner working angle. However, beyond the IWA, the speckles dominate the setup, which results in a deviation from the simulation. The Gaussian

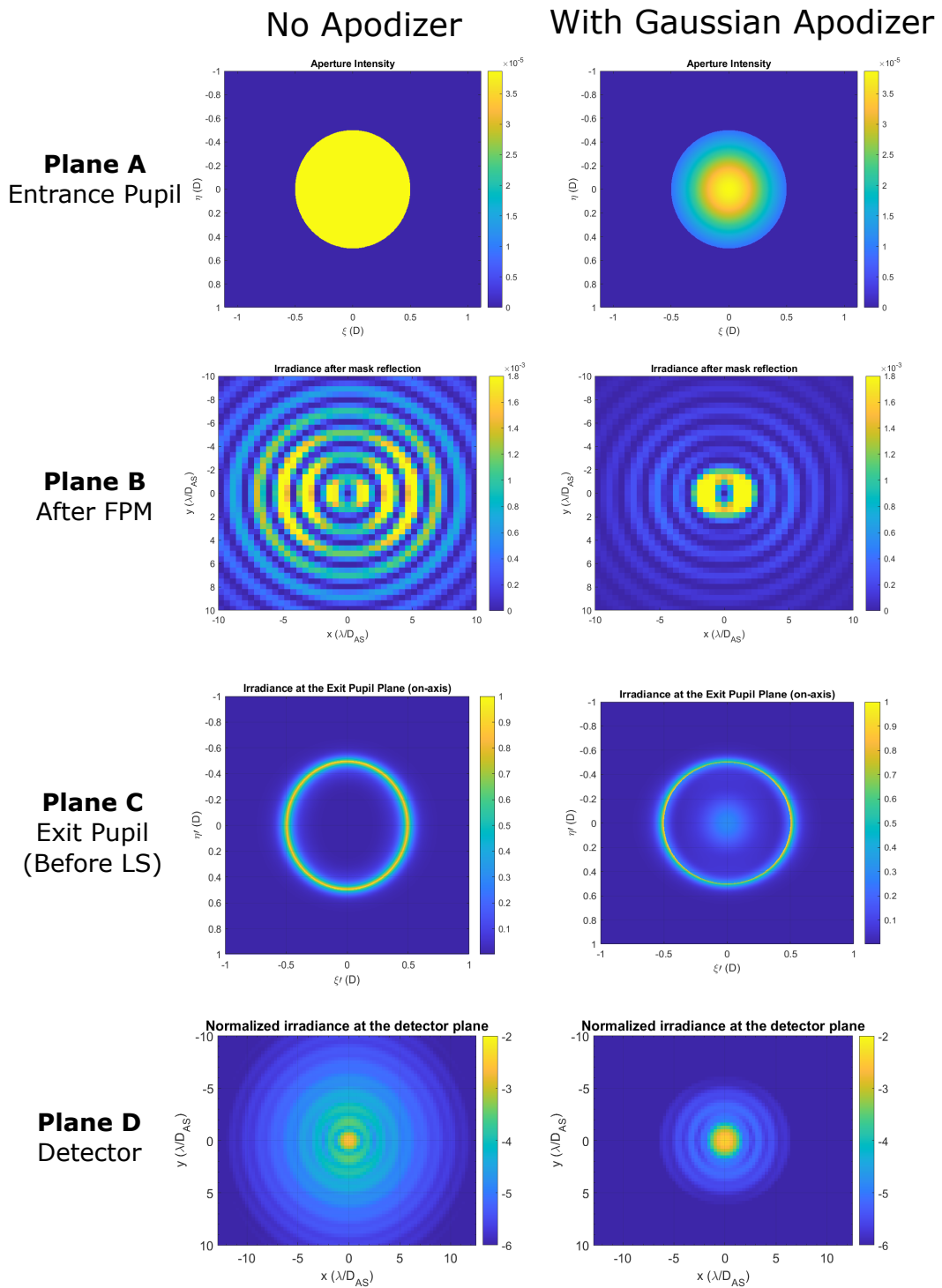


Figure 5.4: 2D Irradiance Distribution at the entrance pupil plane (Plane A), focal plane after the mask (Plane B), exit pupil plane (Plane C), and detector plane (Plane D) before (left column) and after adding a Gaussian apodizer (right column) in the model.

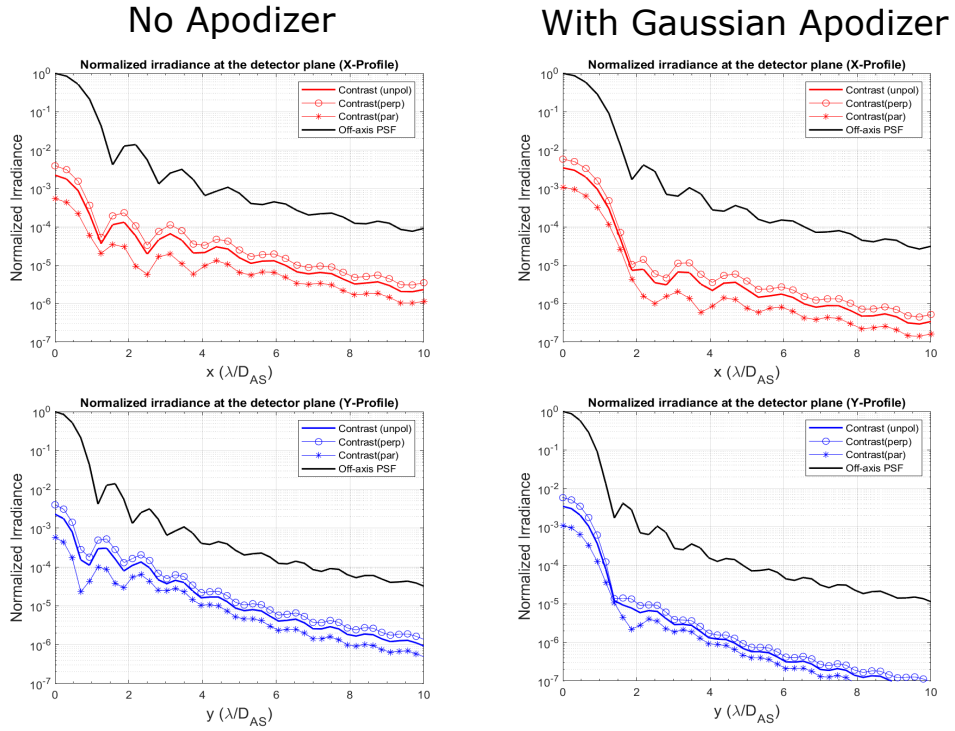


Figure 5.5: Normalized irradiance distribution at the CCD plane with and without a Gaussian apodizer. Results show that a simple Gaussian apodizer attenuated the signal at the PSF wings by an order of magnitude.

apodizer improved the raw contrast by an order of magnitude, such that at the inner working angle, $IWA \approx 4 \lambda/D$, the raw contrast is around 10^{-5} . Finally, Figure 5.8 shows that the raw contrast in the R-band and I-band are the same, verifying the achromatic rejection of EvWaCo.

5.2.1 Mask at $IWA_y \approx 2 \lambda/D$

Adjusting the pressure between the lens and the prism is the equivalent of shaping the air gap. In the previous setup, the smallest mask we can obtain at an $\theta_i \approx 42^\circ$ has an IWA of $3 \lambda/D$ along the mask's minor axis. The actuator we were using at the time had a precision of 10 microns. At the same angle of incidence, a smaller IWA may be achieved with an actuator with finer precision. What happens when the angle of incidence is changed? How does it affect the raw contrast performance?

Figure 5.9 shows the transmission of the evanescent waves along the boundary at

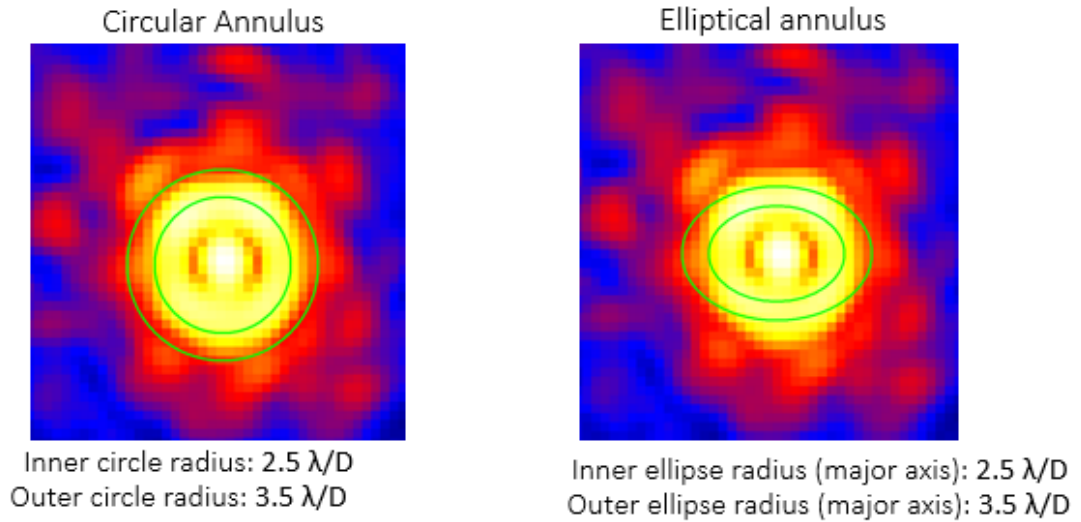


Figure 5.6: Illustration of the radial average calculation.

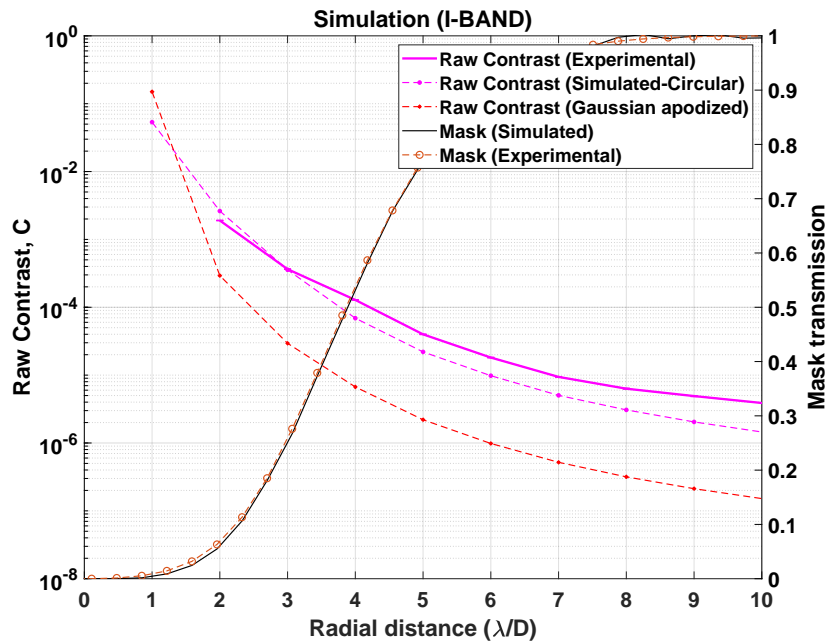


Figure 5.7: Raw contrast using the new equation to calculate the air gap. The experiment and the simulated profiles are a close match. It also shows that the Gaussian apodizer that allows a transmission of 20% at the aperture edges improved the raw contrast by an order of magnitude.

varying air gaps. The evanescent waves travel the farthest from the boundary when the angle of incidence is 42° . The plot shows that you can capture these evanescent waves at a distance greater than 1 micron. Meanwhile, the higher the angle of incidence, the closer the third medium needs to be to capture the evanescent waves.

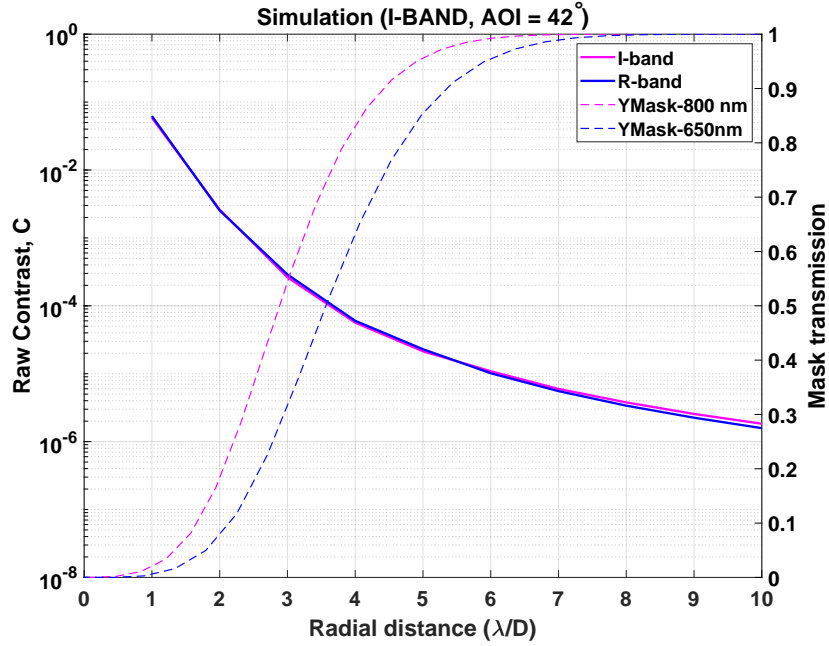


Figure 5.8: Calculated raw contrast in both the R- and I-band, showing the achromatic rejection of EvWaCo.

The testbed was briefly re-aligned for an angle of incidence of 48° , and the mask was set such that the minor axis would be close to $2 \lambda/D$. This small inner working angle is accessible with the actuator of the focal plane mask we used. Although the inner working angle is smaller than the previous setup, the normalized irradiance of the on-axis PSFs is similar to our first coronagraph data using the upgraded focal plane mask at 42° , as shown in Figure 5.10. The PSF peak was suppressed by 3 orders of magnitude while at its inner working angle, the normalized irradiance is a few 10^{-4} .

With the same calculation as in Chapter 5 for the raw contrast, the simulation results in Figure 5.11 shows a raw contrast of 10^{-4} at respective IWA along the x-axis: $\approx 4 \lambda/D$ at $\theta_i = 42^\circ$ and $\approx 3 \lambda/D$ at $\theta_i = 48^\circ$.

5.3 Summary

This chapter demonstrated that the raw contrast performance close to the inner working angle agrees with better estimation of the air gap. However, the raw contrast performance deviates from the simulation at higher frequencies due to speckles that were not

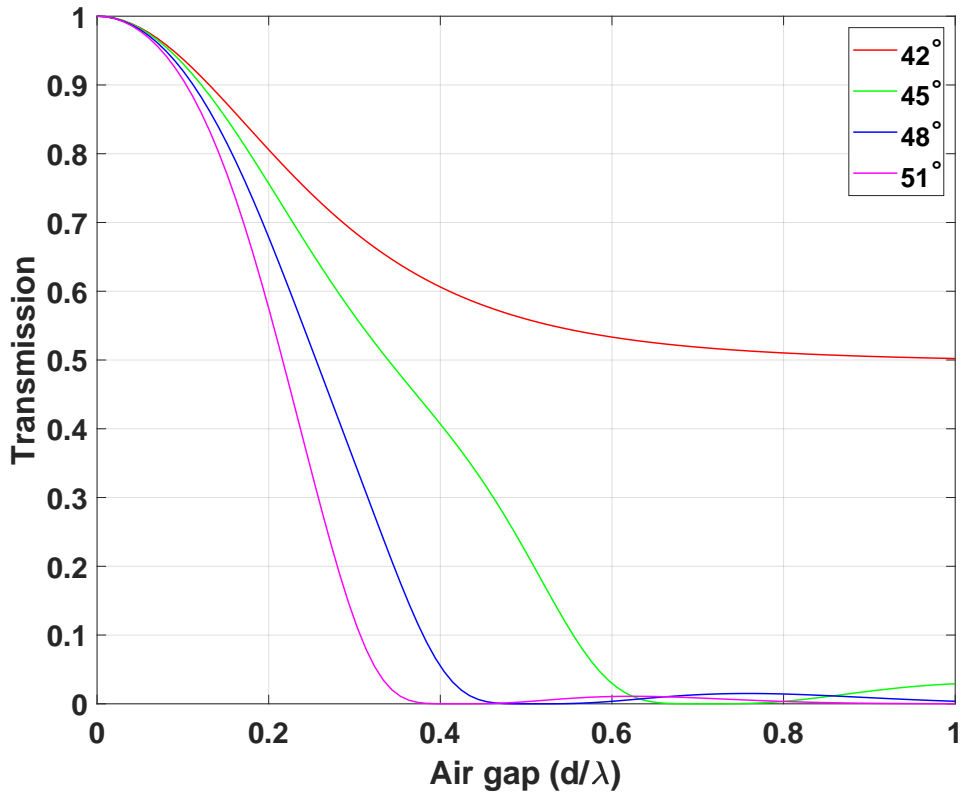


Figure 5.9: The distance along the boundary where you can capture evanescent waves at $1/e$ of their maximum value - penetration depth - varies at different angles of incidence. This is the transmission in unpolarized light.

controlled. This also shows that the raw contrast performance at the inner working angle is approximately 10^{-4} with the coronagraph alone. Apodization can further improve this raw contrast performance by an order of magnitude. It has been demonstrated in simulations by adding a Gaussian apodizer at the entrance aperture. So far, our results have shown that it is possible that we can still go down to an IWA of $2 \lambda/D$ along the mask minor axis using a different angle of incidence, θ_i , and still get consistent results: three orders of magnitude PSF peak suppression and a 10^{-4} raw contrast at the IWA. However, centering the star PSF on the mask may become tricky at smaller inner working angles. This makes the star channel's role very important- ensuring that the PSF is well-centered and controlling the low-order aberrations.

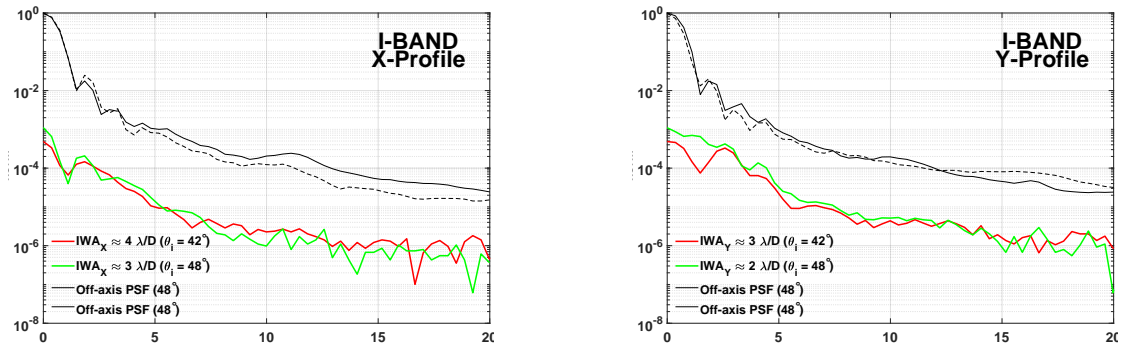


Figure 5.10: Normalized irradiance distribution over the full I-band at different angles of incidence and mask IWA. The on-axis profiles along x and y show that the normalized irradiance is similar despite the difference in the size of the mask.

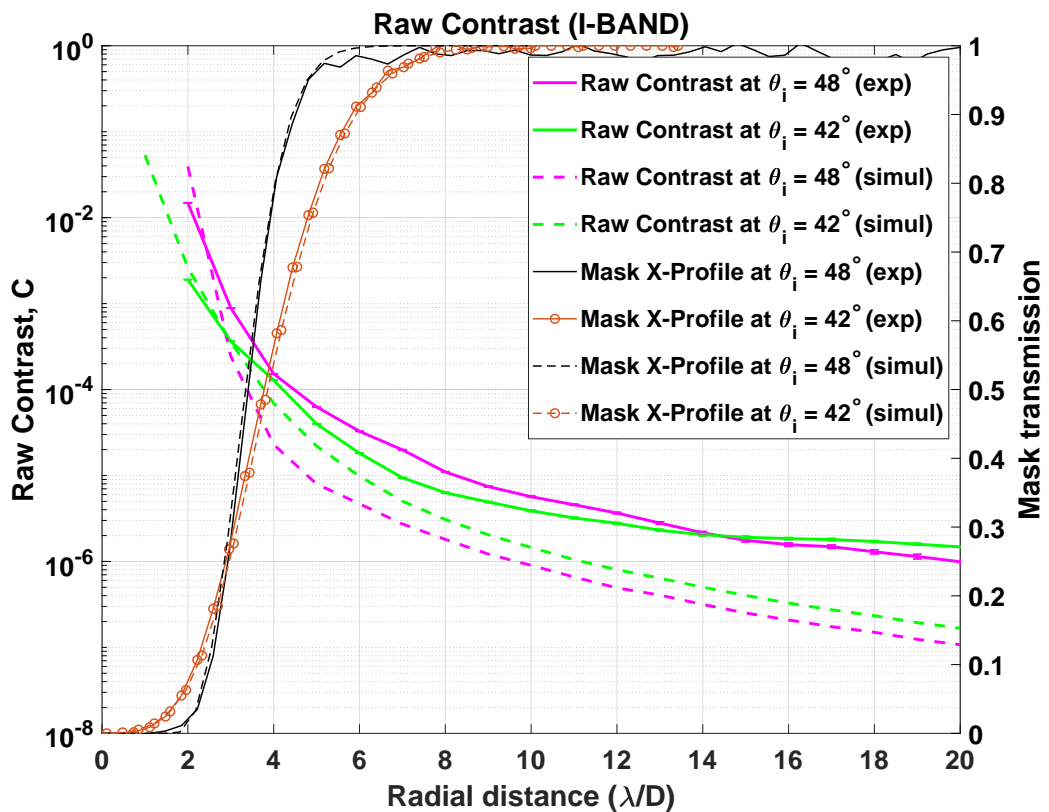


Figure 5.11: Raw contrast in the I-band at 48° angle of incidence and an IWA of $2 \lambda/D$ along the minor axis. At $3 \lambda/D$ along the mask major axis, the raw contrast is at 10^{-4} .

CHAPTER 6

Discussion

The core of the Evanescent Wave Coronagraph is to use the frustrated total internal reflection principle to isolate the starlight from the planet light. This concept is demonstrated by placing a lens and a prism in contact to serve as the focal plane mask. This chapter discusses the limitations of this approach, upgrades to the current setup, and comparison to existing coronagraphs.

6.1 Limitations of the proposed approach

The setup presented is on a passive setup in-air. It does not have an adaptive optics system to correct the wavefront errors due to the optical quality of the components, and the smallest mask size tested has an inner working angle of $3 \lambda/D$ along the minor axis. During the time of the tests, this is the most repeatable smallest mask size - one where the lens is just touching the prism hypotenuse without applying pressure.

The angle of incidence used here is 42° - very close to the critical angle, while the focal ratio is 37.5. The f-number controls how much the size of the PSF increases at the focal plane. To optimize the achromatic rejection, the size of the PSF must match the size of the mask at a particular wavelength. Figure 6.1 shows the relationship between the FWHM of the PSF and the mask at different angles of incidence when the air gap was first assumed to be $d = r^2/2R$. Their linearity is assessed using the Curve Fitting Tool in Matlab and summarized in Table 6.1. A slope of 1 means that the relationship is linear. From the results, the current f-number is the optimal angle for such an air gap and is the incidence angle used in all the previous communications under this project (Buisset et al., 2017; Alagao et al., 2017).

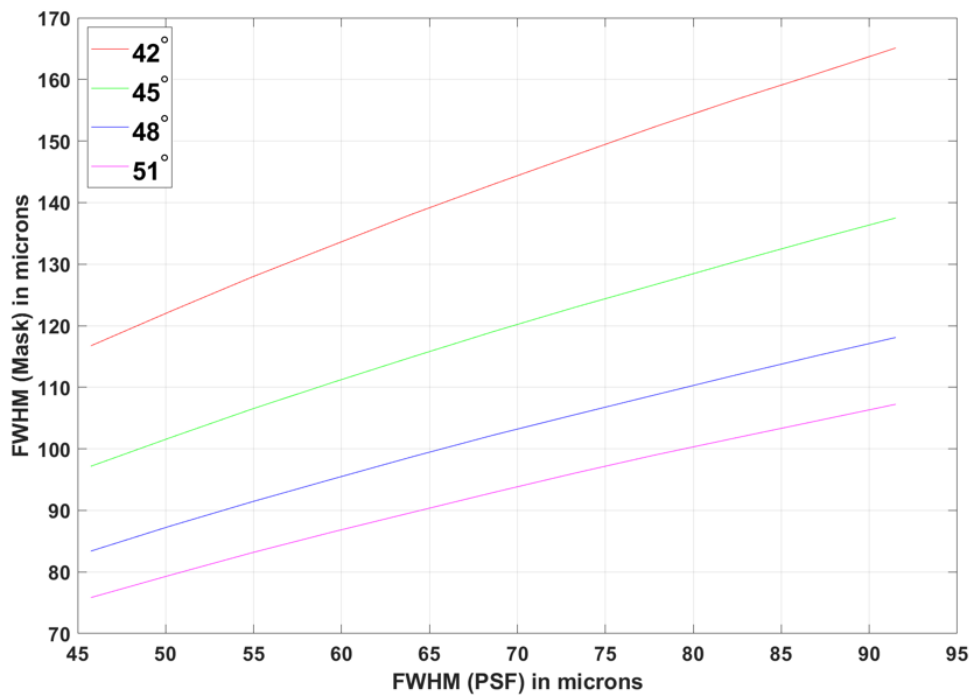


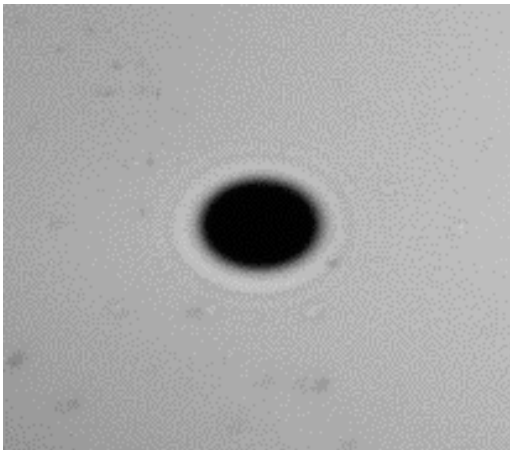
Figure 6.1: Variation of the mask and the PSF at various angles of incidence considering an air gap: $d = r^2/2R$, where r is the radial distance, and R is the radius of curvature of the lens.

Table 6.1: Statistics to Test the Linearity of the Mask and PSF FWHM at different angles of incidence: $f(x) = p_1x + p_2$ for an air gap at $d = r^2/2R$

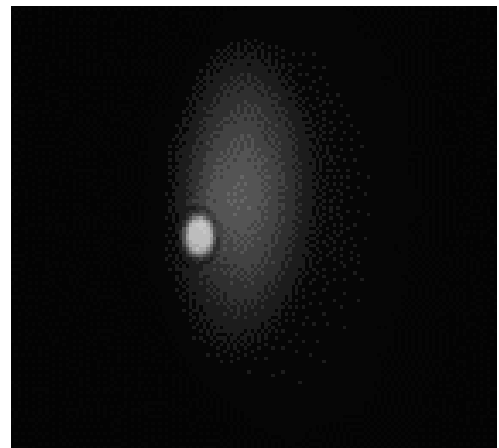
Angle of Incidence	p1	p2	R-squared
42°	1.053	69.9	0.9977
45°	0.878	58.12	0.9978
48°	0.754	49.86	0.9978
51°	0.683	45.47	0.9975

6.1.1 Caveats in using $\theta_i = 42^\circ$

Using $\theta_i = 42^\circ$, a slight tilt induced by a misalignment of the focusing lens in front of the FPM may cause the incidence angle to be less than the critical angle, resulting in interference patterns close to the mask or possibly Newton's rings. Figure 6.2 shows interference patterns in both the companion channel and the star channel flat field images when both the aperture stop and the Lyot stop were removed. For a beam aperture number equal to 37.5, the corresponding semi-cone angle is approximately 0.8° . An angle of incidence of 42° represents the angle between the chief ray and the normal of the prism hypotenuse while the marginal rays will be approximately $42^\circ \pm 0.8^\circ$.



(a) Companion Channel



(b) Star Channel

Figure 6.2: Appearance of possible Newton's rings in the flat field images in both channels due rays with angles of incidence less than the critical angle. This image was obtained when the Lyot stop was temporarily removed from the optical path. The image of the mask in the star channel showed some stray light on one side of the image.

Because the angle of incidence is very close to the critical angle, rays where the angle of incidence is less than the critical angle are transmitted and show up as dark regions in the pupil image. This can be verified through a non-sequential model in Zemax. Figure 6.3 shows the irradiance of the beam reflected by the static prism for a detector placed at the reflected part of the prism, and the entrance pupil is determined by the clear aperture of the focusing lens.

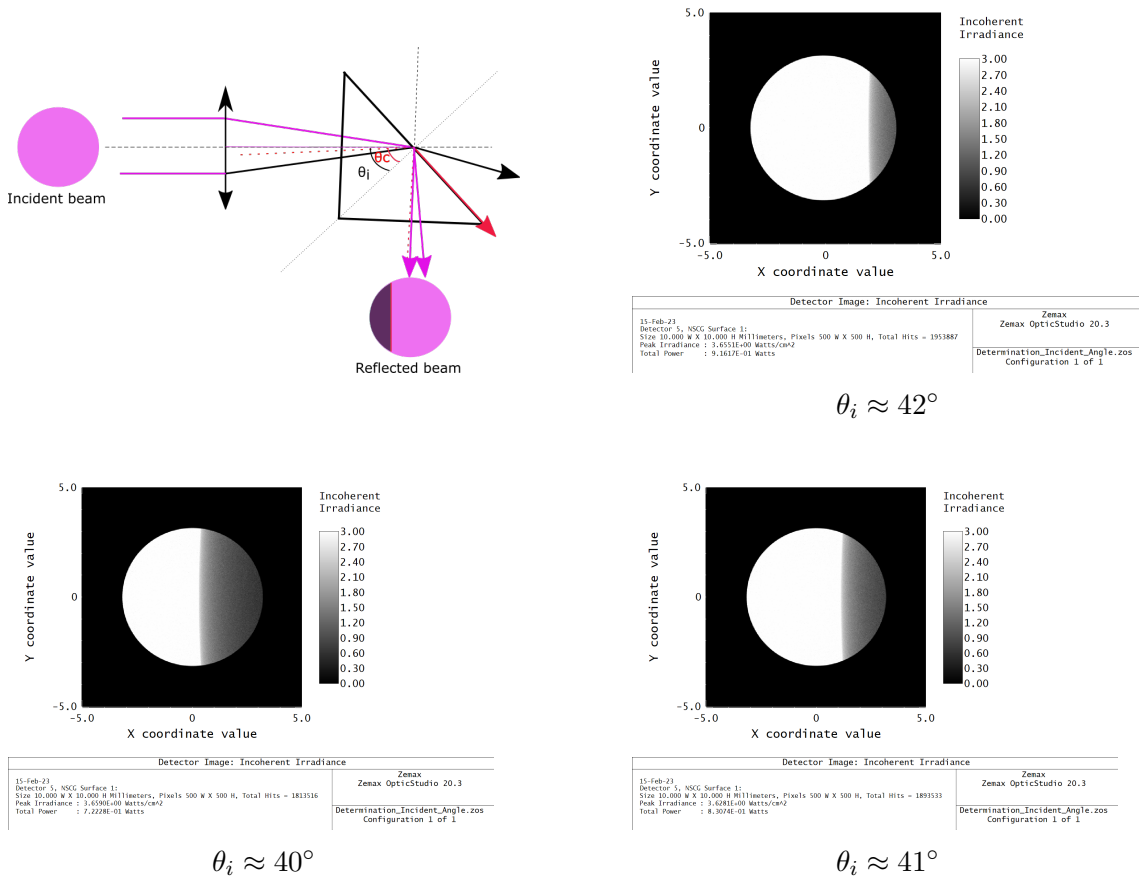
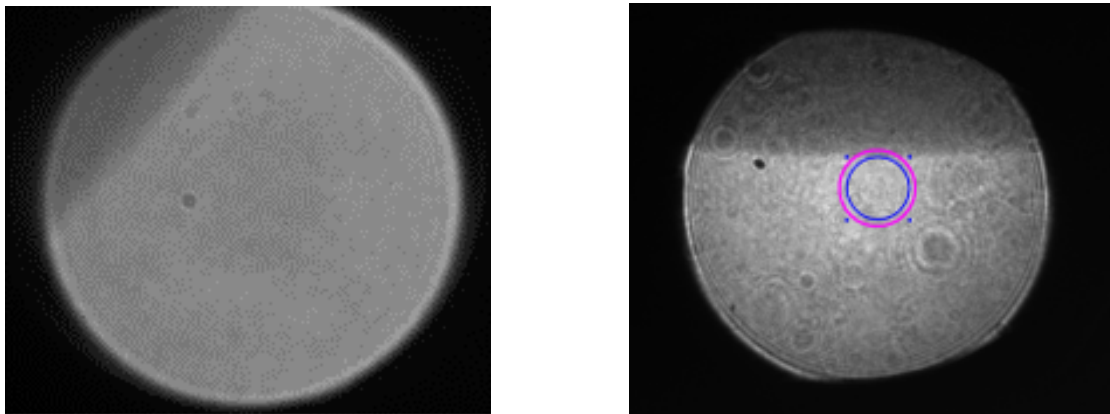


Figure 6.3: Setup drawing for obtaining the pupil images used to determine the angle of incidence (top left) and the corresponding pupil images for $\theta_i = 40^\circ$, $\theta_i = 41^\circ$, and $\theta_i = 42^\circ$. The magenta arrows represent the rays greater than the critical angle (marked by the red dashed line) and, thus, are reflected, while the black arrows represent the transmitted ray. On the pupil image, this shows up as a dark region.

In practice, this can be observed by looking at the pupil image after removing both the aperture and Lyot stops. Figure 6.4 demonstrates the case where the angle of incidence is at 42° and the one where the interference pattern was observed. It was observed when the Lyot stop was removed in the optical path in the companion channel but was apparent when the aperture stop was still in the optical path. The aperture stop selects the bundle of

rays focused on the prism. In this same image, the location of the aperture stop and the Lyot stop were also overlaid. As observed in the image, some of the rays transmitted through the aperture stop are less than the critical angle, resulting in the fringes only observed when the Lyot stop was removed. You will also notice that the dark region occupies a larger region in the pupil image, implying that the incident angle may be less than the critical angle. Upon calculation, the angle of incidence was estimated to be 40° . It will be worth considering angles greater than the incident angle to avoid this issue during integration and assembly on a telescope.



(a) Pupil image at $\theta_i \approx 42^\circ$

(b) Pupil image at $\theta_i < \theta_c$

Figure 6.4: Pupil images after removing the aperture stop and the Lyot stop: (a) at $\theta_i \approx 42^\circ$ and (b) at $\theta_i \approx 40^\circ$ when the fringes were observed. The magenta circle represents the location of the aperture stop, while the blue circle represents the location of the Lyot stop. A small portion of the dark region is within the area transmitted by the aperture stop. This region represents rays less than the critical angle and, thus, are transmitted, resulting in interference in the flat-field image.

6.1.2 Current solution to mask hysteresis

In the experiments presented in Chapter 4, we adjusted the actuator so that the inner working angle of the mask for a certain wavelength (say $\lambda \approx 800$ nm) is equal to $3 \lambda/D$ and was maintained throughout the experiment. Without any abrupt adjustment to the actuator, it ensures that the results are repeatable.

Actuators are prone to hysteresis - for a given micrometer reading in the actuator, the size of the mask may not be the same after pushing or pulling the actuator. The actuator must be well-calibrated. One of the steps towards resolving this issue is by assessing in

real-time the IWA of the mask while adjusting the actuator on the FPM to avoid such discrepancies. The method uses 2D Gaussian fitting of the flat-field images to find the center of the mask and display its corresponding cross-section along the mask's major axis. Figure 6.5 shows a screenshot of this tool that allows us to quickly assess the corresponding FWHM as soon as the pressure is adjusted. The data points (blue) are plotted against the fitted Gaussian curve (orange line). Knowing the number of pixels per λ/D , one can immediately calculate the current IWA. For example, in the current setup, 1 λ/D equals 3 pixels; thus, an FWHM of 18 pixels corresponds to 3 λ/D along the mask major axis. So far, our preliminary tests show that although useful to the users during the adjustment of the desired mask IWA, calibration is still needed to achieve the desired air gap.

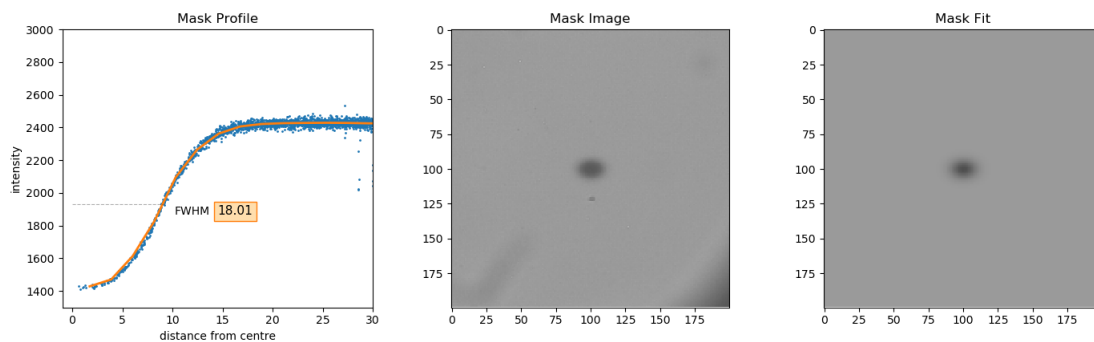


Figure 6.5: Mask profile along the x-axis with an IWA of 3 λ/D obtained at $\lambda_c = 800nm$. These images were obtained using the mask pressure tool developed to automatically determine the IWA during pressure adjustment. 1 λ/D is equal to 3 pixels. Thus, to obtain an IWA of 3 λ/D , the FWHM should be 18 pixels. Image credit: Matthew Ridsdill-Smith

6.2 Considerations for the focal plane mask design

The performance of the coronagraph depends on the air gap. Small changes in the air gap could impact the performance significantly. A close-up view of the boundary between the prism and the lens in Figure 6.6 shows the distance from the center of the contact area where an off-axis PSF will remain focused at the prism hypotenuse. Raw contrast performances are calculated using three sets of PSF as described in Appendix B: on-axis PSF, unsaturated off-axis PSF, and saturated off-axis PSF. The off-axis PSF represents the flux of the star in non-coronagraphic mode. Using the EvWaCo focal plane mask, the focusing lens on the FPM must have a depth of focus such that the PSF remains focused at a certain distance from the contact area. For a focal ratio equals 37.5, the corresponding

depth of focus (DOF) equals $\pm 2 \lambda (f/\#)^2$ or ± 2.25 mm at 800 nm. The focal ratio affects the linearity between the mask and the PSF FWHMs and impacts how far from the contact area the PSFs will remain focused at the prism hypotenuse for off-axis sources. Because of the long DOF, it is quite tricky to determine whether the PSF is precisely focused on the prism hypotenuse. During our experiments, this was determined by adjusting the focusing lens along the optical axis such that you obtain a very dark signal at the center of the exit pupil plane.

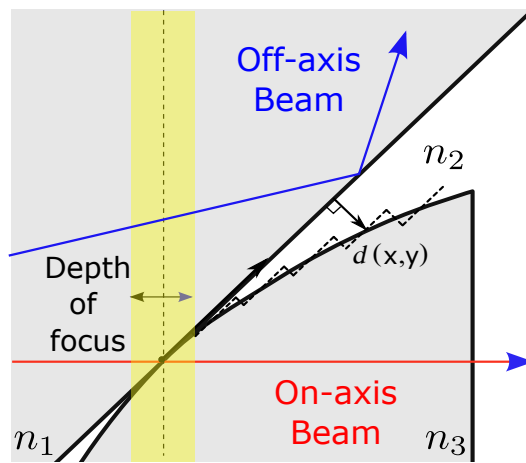


Figure 6.6: Closer look at the boundary between the lens and the prism. Using a higher focal ratio for EvWaCo results in a longer depth of focus which makes it tricky to precisely focus the star PSF exactly at the prism hypotenuse. Image credit: Anthony Berdeu

6.3 Combining the coronagraph and wavefront control - setup upgrade

The previous chapters mostly discussed the performance at the companion channel. One of EvWaCo's main capabilities is simultaneously gathering the starlight and companion light. The light transmitted by the focal plane mask, referred to as the star channel, ensures that the star is well-centered on the focal plane mask and has a potential for low-order wavefront sensing. We have shown a preliminary result of the star channel in our previous communication (Alagao et al., 2017) using a large mask, but we have yet to investigate the performance of the star channel for smaller masks.

The EvWaCo testbed, described in Chapter 4, was upgraded again to include a deformable mirror and star channel, as shown in Figure 6.7. Lenses L2 and L3 are added to the optical train to re-image the surface of the DM at the aperture stop. The beam transmitted by the FPM goes towards the star channel composed of two lenses L8 and L9, responsible for re-imaging the star PSF at the FPM hypotenuse plane. The star channel camera is a Point Grey Camera Grasshopper 3 with a pixel size of $3.45 \mu m$. In this channel, the beam reflected by the beam splitter (BS) could be directed to a wavefront sensor (WFS) or coupled to an optical fiber to be fed to another instrument, such as a spectrograph. For reference, the setup was first aligned with a flat mirror in place of the DM. Table 6.2 lists the changes in parameters due to this realignment.

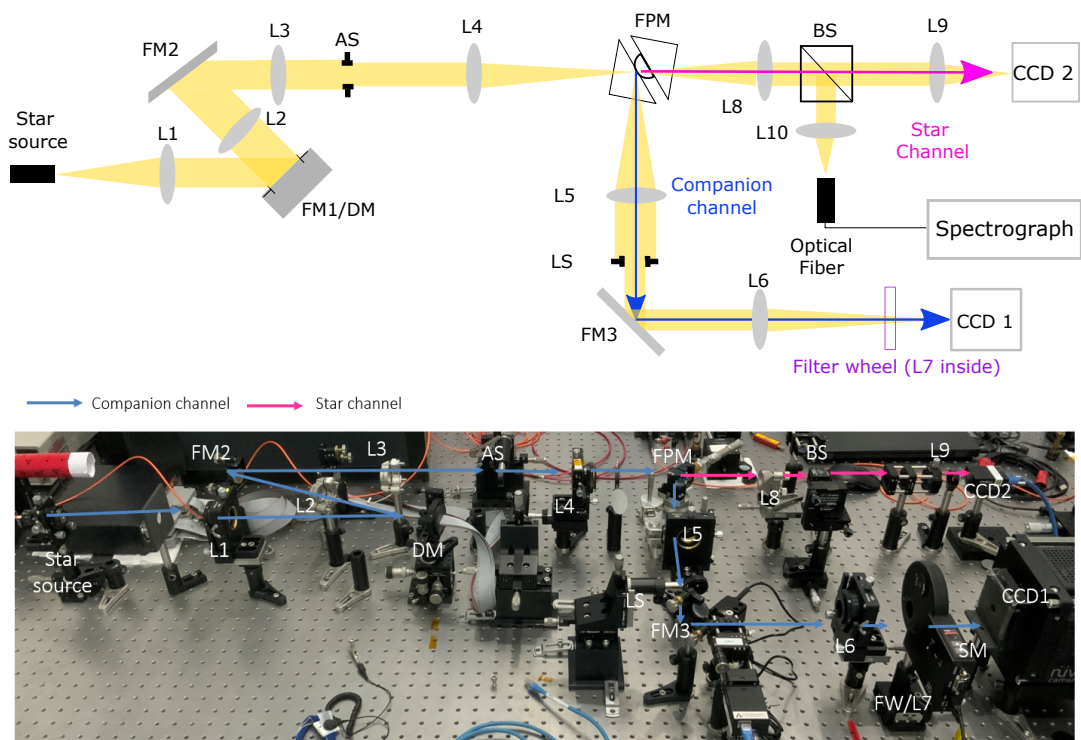


Figure 6.7: Schematic and image of the upgraded EvWaCo testbed. The blue lines represent the light path of the companion channel, while the magenta line represents the light path of the star channel. The meanings of the acronyms inside the diagram are as follows: achromatic doublet (L), plane mirror (FM), deformable mirror (DM), aperture stop (AS), focal plane mask (FPM), beam splitter (BS), wavefront sensor (WFS), charge-coupled device (CCD).

Table 6.2: Parameters of the new EvWaCo Testbed

Parameter	Value (in mm)	Comments
f_1	250	Collimator
f_2	200	Re-imaging lens
f_3	200	Re-imaging lens
f_4	150	Focuser
f_5	150	Collimator
f_6	250	Focuser
f_7	100	Inside the filter wheel
f_8	150	Collimator
f_9	75	Focuser
D_{AS}	4	Aperture stop and DM diameter
D_{LS}	3.25	$0.8D_{AS}$
d_{pix}	0.016	Nuvu Hnu 512
T_{CCD}	-60	(in degrees) CCD cooling temperature

Table 6.3 lists the relation between the linearity of the mask FWHM and the PSF FWHM using a better estimate of the air gap, discussed in Chapter 5, for a small mask. Results showed that 42° remains the optimal angle. However, it must be noted that the linearity between the FWHMs of the mask and the PSF at different incident angles varies depending on the air gap. For the current air gap, the relationship between the FWHM of the mask and the PSF is becoming less linear.

Table 6.3: Statistics to Test the Linearity of the Mask and PSF FWHM at different angles

of incidence: $f(x) = p_1x + p_2$ for an air gap at $d = \max \left(\sum_{n=0}^3 a_n \left(\frac{x}{x_o} \right)^n, 0 \right)$

Angle of Incidence	p1	p2	R-squared
42°	1.012	95.15	0.995
45°	0.896	78.47	0.995
48°	0.805	66.39	0.995
51°	0.751	0.751	0.751

In our recent upgrade, the $f/\#$ is kept at 37.5, but the angle of incidence has been changed to 45° . This is also the angle of incidence being considered for the most recent design of the EvWaCo prototype.

6.3.1 Verifying the alignment of the DM

Speckles limited the raw contrast performance obtained in the laboratory due to the absence of adaptive optics. By convention, a high-contrast imager combines a coronagraph and an adaptive optics system to perform wavefront control. Aberrations and speckles degrade the raw contrast performance and must be minimized to detect faint companions.

The first set of tests done on the upgraded testbed is to correct for the static aberrations due to misalignments in the system. The Toolkit for Adaptive Optics (TAO) software developed by our collaborators from Centre de Recherche Astrophysique de Lyon (CRAL) integrated the DM and camera control under one software using a client-server architecture. It contains the necessary algorithms to control the in-house AO components. One of the algorithms is the correction of the non-common path aberrations (NCPA) that uses NEWUOA Powell's algorithm (Powell, 2006). It outputs the appropriate DM commands to obtain the best image quality by maximizing the variance in the image plane.

The algorithm will calculate the DM commands after assessing the quality of the PSF at CCD1. These calculations are already embedded in the TAO software. In these measurements, the lens and the prism were still not in contact, mimicking a non-coronagraphic setup to simplify the alignment verification. The EvWaCo focal plane mask filters the low-order frequencies when the lens and the prism are in contact (coronagraphic mode), making it difficult to assess whether the DM is conjugated well to the aperture stop. If so, we will observe a uniform illumination at the exit pupil when the actuators are poked.

This testbed is reserved for pedagogical purposes - to learn high-contrast imaging. In the context of my PhD, I used this test bed to learn how to integrate the alignment of the DM to the coronagraph for the first time. The deformable mirror used is a BMC DM from the Thorlabs educational kit, while the DM that will be used for the EvWaCo prototype is

an ALPAO DM and characterized in a different testbed (Berdeu et al., 2022).

Before running the NCPA algorithm inside the TAO, the integration time was set such that the maximum value of the PSF peak was half the maximum before saturation. The region of interest is also cropped only to assess the variance on an area that does not include the secondary diffraction peaks. In our case, it corresponds to a 40 pixel by 40 pixel area of approximately $\pm 6\lambda/D$, ensuring that it does not include the bright secondary peaks.

The evolution of the PSF before and after modal correction is shown in Figure 6.8, and the quality of the PSFs was assessed by calculating the fraction of encircled energy (Figure 6.9). In theory, 84% of the energy in an Airy pattern is contained in the 1st dark ring represented by the dashed curves. With the flat mirror, this value is 69% and 45% when the DM is at rest. For the flat command of the DM (actuators at 0.5 stroke), the energy inside the first Airy radii is close to 67%. It is also good to note that the flat command of the DM behaves almost like a flat mirror. Moreover, after doing a modal correction, the fraction of encircled energy at 1 Airy radius is 73%, slightly better than with the flat command. The reference flat mirror has a surface flatness of $\lambda/10$ at 632.8 nm from the Newport website.

6.3.2 Preliminary results at the companion Channel and star channel

The same DM commands obtained after modal correction were used to assess the preliminary coronagraphic performance of this upgraded setup. It can be observed from the companion channel images that the central peak of the star has been reduced by 3 orders of magnitude, as already observed in the previous experiment. However, the surrounding bright light at the location of the IWA that was suspected to be due to low-order aberrations was already reduced after modal correction. Although the secondary diffraction peaks looked like dominant structures, they were outside the region of correction that is only up to $\pm 5 \lambda/D$. These peaks are located at $\pm 9 \lambda/D$ with a width of around $5 \lambda/D$.

The second column of Figure 6.10 shows the part of the PSF transmitted by the focal plane mask, and their respective cross-sections are shown in Figure 6.11. The images

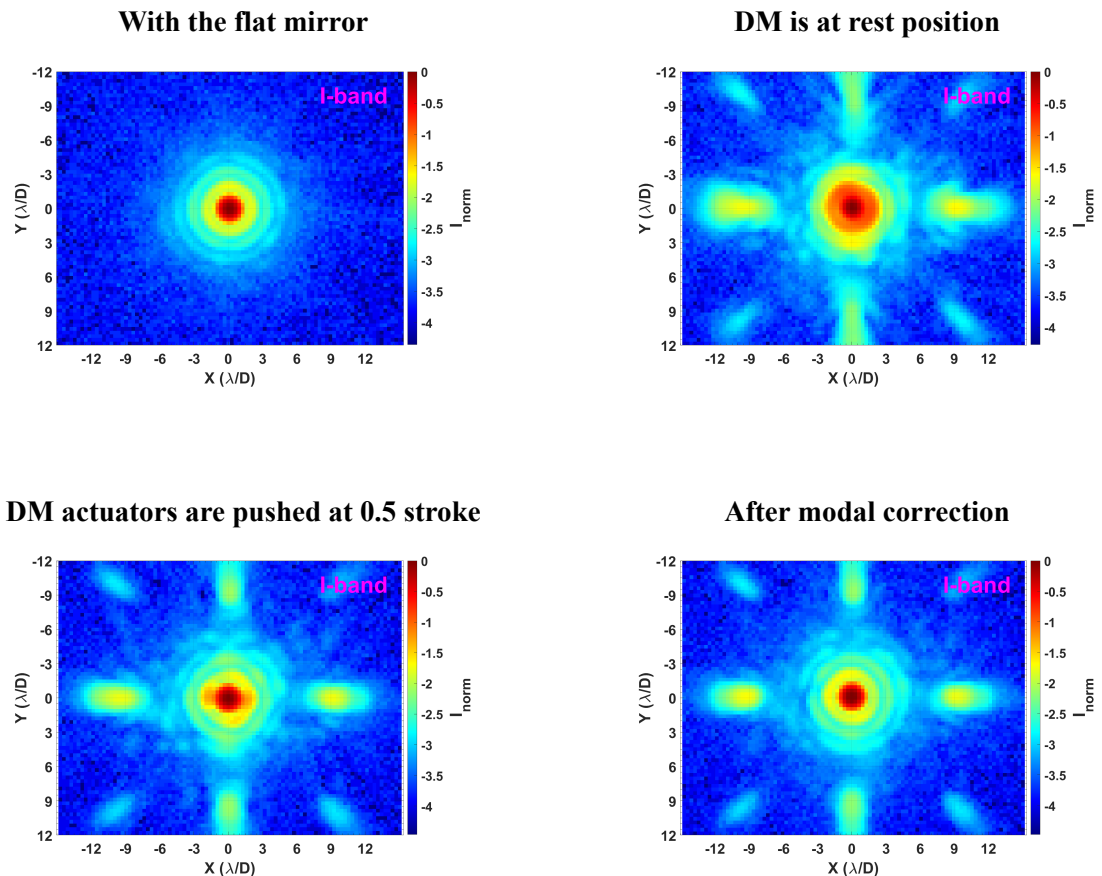


Figure 6.8: Qualitative comparison of the non-coronagraphic PSFs obtained using the flat mirror, when the DM is at rest when the actuators are pushed at 0.5 stroke (flat command) and after performing the modal correction.

reveal the presence of the central peak and the first Airy ring. Recall that the focal plane mask apodizes the wings of the PSF. This implies that the number of Airy rings observed at the star channel depends on the mask's size and the detector's sensitivity. The number of Airy rings transmitted by the focal plane mask is only up to 3 and the rest were already apodized because the location of the other rings fall in an air gap beyond the penetration depth of the evanescent waves.

These results are only preliminary. The next step would be to perform the static aberration correction in coronagraphic mode (lens and prism in contact) and assess the limits imposed by the BMC DM on the system's performance through simulations.

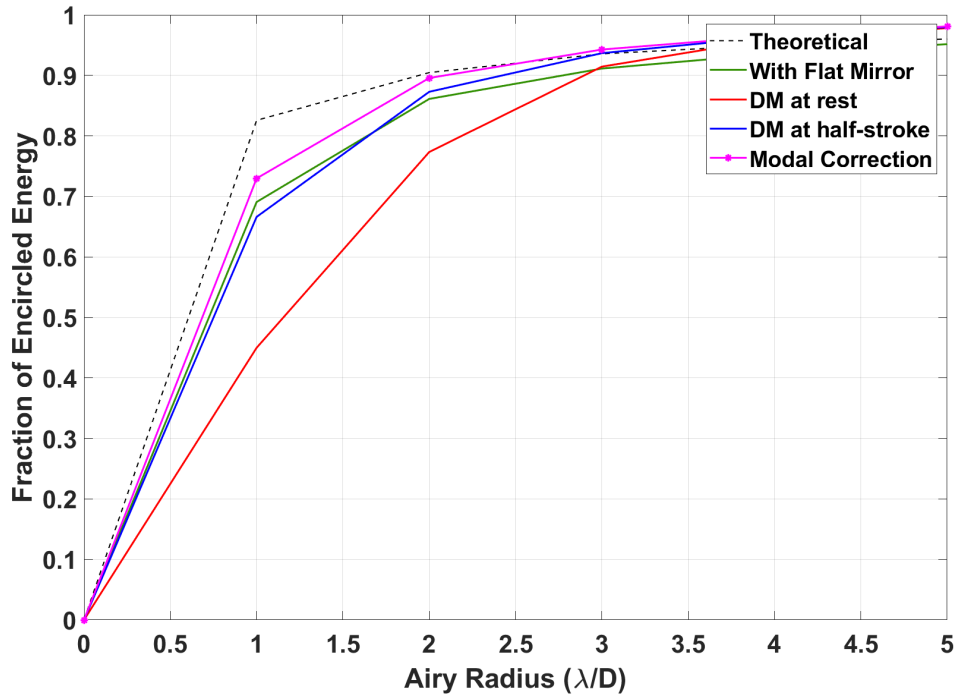
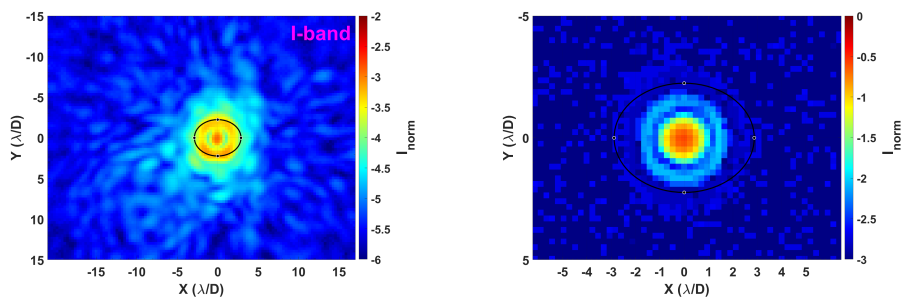


Figure 6.9: Fraction of encircled energy of the non-coronagraphic PSF before and after correction. At 1 Airy radius, the fraction of the encircled energy is the following: 84% (Theoretical), 69% (flat mirror), 45% (DM at rest), 67% (DM half-stroke), and 73% (modal correction).

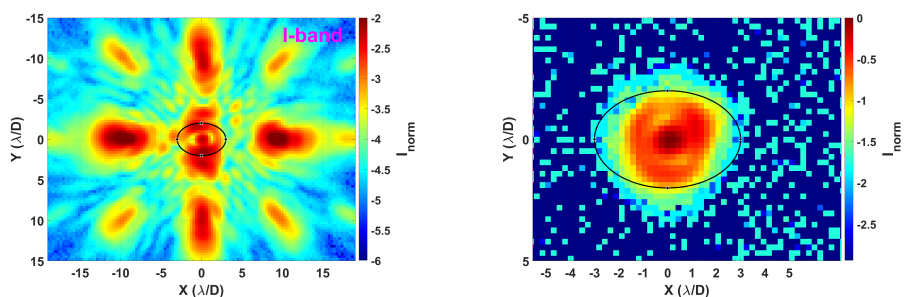
6.4 Summary

The concept of EvWaCo can be easily demonstrated with an off-the-shelf lens and prism. However, care must be taken when considering the beam aperture number at the focal plane and the angle of incidence. These two parameters impact the mask profile and the efficiency of the achromatic rejection. Since the air gap plays an important role in determining the coronagraphic performance, it is worth considering the hysteresis of the actuator used in the FPM. In this study, a real-time evaluation of the mask IWA is starting to be tested in the lab. The current laboratory performance of EvWaCo is limited by the absence of adaptive optics to minimize the presence of speckles that degrade the contrast performance. Hence, the setup has been upgraded to include the deformable mirror and the implementation of the Toolkit for the TAO software. These steps lay the groundwork for EvWaCo to incorporate wavefront control in its main operation and assess the performances that can be achieved with the EvWaCo prototype that will be installed at the 2.4 m Thai National Telescope.

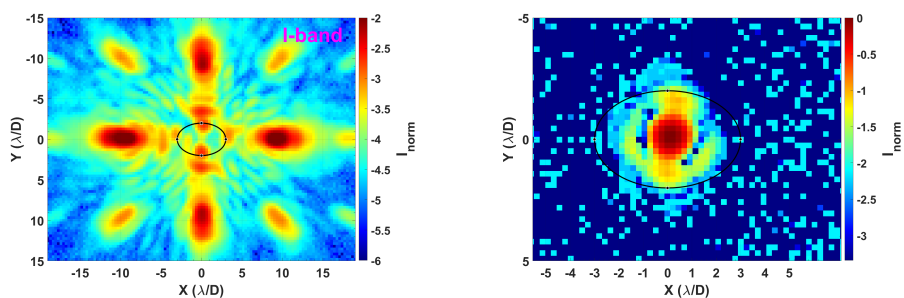
With the flat mirror



DM at rest



DM at half-stroke



DM after modal correction

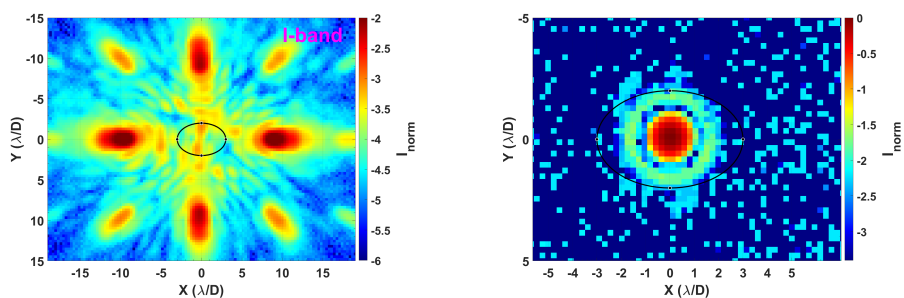


Figure 6.10: 2D Map of the Normalized Irradiance from the upgraded EvWaCo testbed using only the flat mirror (reference) and after installing the DM. These images were obtained over the full-Iband in unpolarized light with mask IWA (ellipse): $IWA_x \approx 3 \lambda/D$ and $IWA_y \approx 2 \lambda/D$.

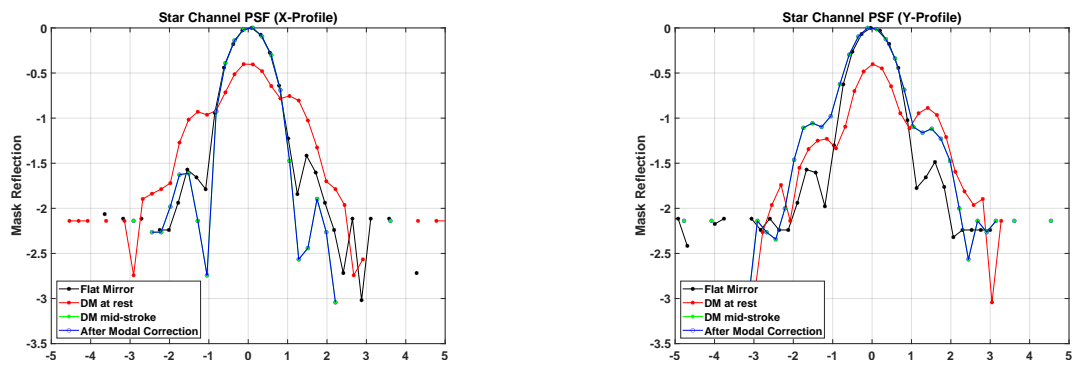


Figure 6.11: Cross-section of the transmitted star PSF for an $IWA_y \approx 2\lambda/D$ in the I-band. The results indicate that the number of rings visible at the star channel highly depends on the size of the mask used.

CHAPTER 7

Conclusion and Perspectives

The advantage of direct imaging over other exoplanet methods is access to the planet's photons for spectrally characterizing its atmosphere. Coronagraphy blocks the starlight or strongly attenuates it at the telescope focal plane to detect a planet and any faint hidden structures close to its environment that will enrich our understanding of planet formation, such as circumstellar disks and debris.

The Evanescent Wave Coronagraph (EvWaCo) is a type of Lyot coronagraph that utilizes the frustrated total internal reflection principle to isolate the starlight from the planet light. Its focal plane mask comprises a prism, oriented at an angle of incidence greater than the critical angle such that total internal reflection may occur, and a lens placed in contact to capture the evanescent waves decaying rapidly at the boundary of the prism hypotenuse. This configuration allows us to capture the star and planet's light simultaneously.

This PhD study focused on the characterization of EvWaCo at small inner working angles ($\leq 3 \lambda/D$) by assessing its performance in a passive, in-air testbed using the upgraded focal plane mask optomechanical support that allows an easier and more stable adjustment of the pressure between the lens and the prism - thereby, adjusting the air gap, and varying the size of the mask.

Experimental results showed a raw contrast of 10^{-4} at $3 \lambda/D$ over the full I-band ($\lambda_c = 800 \text{ nm}$, $\Delta\lambda/D \approx 20\%$) and at $4 \lambda/D$ over the full R-band ($\lambda_c = 650 \text{ nm}$, $\Delta\lambda/D \approx 23\%$). Experiments done over the 8-month study showed that the results are repeatable - the PSF peak was suppressed by three orders of magnitude while at the IWA, the normalized irradiance is typically 10^{-4} .

The coronagraph's sensitivity to tilt, defocus, and lateral misalignment of the Lyot

stop were also measured. Because of the angle of incidence, the mask is elliptical, where the ratio between its FWHM along its x-axis (major axis) and y-axis (minor) equals $1/\cos\theta$. This results in a variation in the tilt tolerable misalignment along each axis: $\theta_y \approx 0.2 \lambda/D$ and $\theta_x \approx 1 \lambda/D$. Meanwhile, the performance of the coronagraph still yields a normalized irradiance of 10^{-4} with defocus of up to 0.65λ PTV. The results for misaligning the Lyot stop, which is currently 0.8 times the aperture stop diameter, suggest that the current Lyot stop diameter can still be enlarged to 90% but with a tighter alignment tolerance. Finally, a simulation of a planet in the lab, 25,000 times fainter than the star with a separation of $5.5 \lambda/D$, demonstrated that it can be detected with an SNR of 11.

The air gap between the lens and the prism drives the performance of the coronagraph. However, due to the lack of a force sensor, the deformation on the prism surface when the lens is pressed can only be derived from experiments. The air gap was estimated using an n-degree polynomial equation and finding the coefficients where the simulated mask profiles best match the experimental mask profiles. The mask profiles are computed from the derived Fresnel reflection coefficients where a thin, homogeneous medium (considered air) is sandwiched between two media of the same index of refraction.

These reflection coefficients of the mask depend on the index of refraction, angle of incidence, and polarization. The angle of incidence used in our first EvWaCo tests is approximately 41.75° , slightly above the critical angle, 41.45° , for the N-BK7 glasses. To optimize the achromatic rejection, the f-number is matched so there will be a linear relationship between the FWHM of the mask and the PSF. Thus, the f-number used in the setup is 37.5.

The current setup uses achromatic doublets with AR coatings in the wavelength range [650 nm, 1050 nm]. This coating is only suitable for experiments in the I-band [700 nm, 900 nm]. However, in the R-band [500 nm, 800 nm], unwanted reflections due to wavelengths outside the AR coating range may cause scattered light that will contaminate the high-frequency region. This led to a mismatch in the experimental raw contrast results in the I-band and the R-band. This issue will be resolved in the EvWaCo prototype as it uses off-axis parabolas. The simulated raw contrast shows that an achromatic rejection

is achieved over the full R- and I-band [500 nm, 900 nm], thus confirming that the mask adapts to the wavelength.

Another interesting result in the study is that the achromatic rejection is only effective at the smallest inner working angle, where $IWA_x \approx 4 \lambda/D$ and $IWA_y \approx 3 \lambda/D$. This result led to a closer investigation of the limiting factor in achieving an achromatic rejection using the EvWaCo focal plane mask. So far, another study at a different angle of incidence 48° using the current setup reached similar performance over the full I-band but at a smaller inner working angle, $IWA_x \approx 3 \lambda/D$ and $IWA_y \approx 2 \lambda/D$. Finally, a simple Gaussian apodizer can be used at the entrance pupil to improve the performance to 10^{-5} at the IWA and $\leq 10^{-7}$ at distances greater than $6 \lambda/D$. This test has been simulated first with the mask with $IWA_x \approx 4 \lambda/D$ and $IWA_y \approx 3 \lambda/D$ in the I-band.

7.1 Comparison to existing coronagraphs

In theory, several coronagraphs already reach the 10^{-10} contrast required to detect Earth-like planets (Guyon et al., 2006). However, there are different trade-offs regarding manufacturability, useful throughput, discovery space, ability to work at smaller angular separations, and sensitivity to stellar angular size. The work presented here shows that even using a simple off-the-shelf lens and prism, a raw contrast of 10^{-4} can already be achieved at smaller inner working angles ($\geq 2 \lambda/D$). However, unlike the optical vortex coronagraph (Mawet et al., 2010) and the PIAA (Guyon, 2003) that can offer a 100% throughput, the Lyot stop in EvWaCo is slightly undersized to a factor of 0.8, decreasing the throughput in the system.

The APLC uses a pupil apodization, a hard-edged focal plane mask, and a Lyot stop. The APLC tests for VLT-SPHERE (Guerri et al., 2011) show a normalized irradiance of 10^{-5} at the IWA. Meanwhile, in the Gemini Planet Imager (Soummer et al., 2009), their propagation modeling in the H-band for the APLC shows that a raw contrast (without wavefront control) of 10^{-6} can be obtained at angular separations $> 5 \lambda/D$. Using the pupil apodization techniques of APLC and the EvWaCo focal plane mask, a similar performance may be achieved at a broader spectral bandwidth than the conventional APLC setup.

Phase masks, such as the FQPM and the vector vortex, are known to achieve deep contrasts at small inner working angles. However, they are also more sensitive to low-order aberrations, thus requiring exquisite wavefront control to maintain contrast stability. The best place to sense these aberrations is to put a measuring apparatus as close to the coronagraph (Mawet et al., 2012). EvWaCo can simultaneously access the starlight and planet night light. Access to the star ensures proper centering on the mask and control of low-order aberrations to prevent star leakage around the mask center. Most coronagraphs rely on the residual starlight to assess the low-order wavefront aberrations. For EvWaCo, the quality of the PSF can already be assessed through the star channel either by imaging or wavefront sensing.

Most coronagraphs, such as the vortex coronagraph, need to be polarized. In the case of EvWaCo, the raw contrast is at 10^{-4} in unpolarized light. Although EvWaCo needs demonstration, preliminary calculations (Buisset et al., 2017) show that the EvWaCo mask varies at different polarizations. There is a potential to gain a deeper contrast in favor of one polarization.

Finally, because of EvWaCo's capability to change the mask size, there is a possibility that it is less sensitive to stellar angular radius if coupled with state-of-the-art wavefront control techniques.

7.2 Adaptation to big telescopes

Unlike other coronagraphs, such as the vector vortex and FQPM, which can be put on a wheel to alternate the active coronagraph design, EvWaCo takes up space. This is because of the angle of incidence used and may require a careful design if the beam aperture number needed to optimize achromatic rejection is unavailable with off-the-shelf components.

Since the performance depends on the air gap, a good focal plane mask actuator calibration is needed. In the case of the EvWaCo prototype, its optical design gained insights from the results obtained from the EvWaCo testbed. It uses the same beam aperture number, but the angle of incidence is currently set at 45° due to space allocation. Since

central obscurations and spiders degrade the coronagraphic performance, the EvWaCo prototype will use an elliptical unobscured sub-aperture. The elliptical aperture is due to the asymmetry of the mask at the FPM plane.

Most of the critical components for the EvWaCo prototype were already procured and under test. Results of the characterization of the AO components can be found in (Berdeu et al., 2022). Figure 7.1 shows the first results of the alignment of the off-axis parabolas for the prototype—preliminary results show the presence of coma and astigmatism.

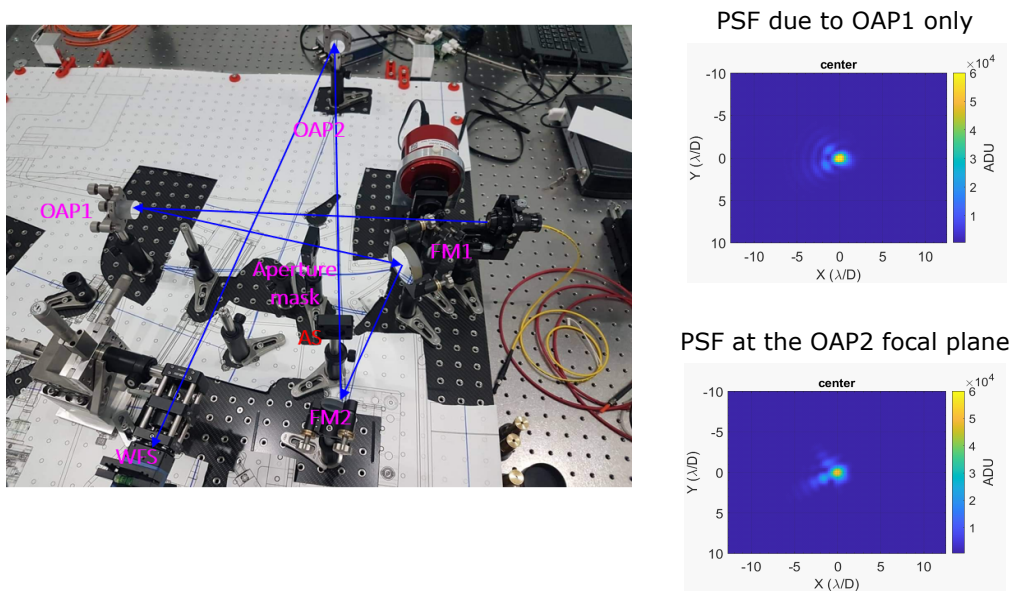


Figure 7.1: Preliminary results of the EvWaCo prototype alignment in the lab.

7.3 Wavefront control and coupling to high-resolution spectrograph

The newly upgraded setup equipped with a deformable mirror will be used to assess the performance of the EvWaCo after implementing wavefront control and focal plane mask actuator control. As mentioned in the previous chapter, the long depth of focus used adds uncertainty to whether the PSF is focused on the prism hypotenuse. Using the deformable mirror, we can measure the coronagraphic performance when a certain amount of defocus is induced in the setup. The current angle of incidence used in this testbed is

45 °, which is the same as the current optical design of the EvWaCo prototype. Using this testbed, the smallest IWA that can be achieved with EvWaCo can be tested by replacing the current actuator with a well-calibrated nano-piezo actuator (with a precision of 10 nm). In addition, the effect of polarization can also be studied. Although the deformable mirror used is not the same as the one from the EvWaCo prototype, the tests done in this testbed can complement the experiments for the EvWaCo prototype and verify numerical simulation results.

The last of the initial objectives of my Ph.D. research is to couple a high-resolution spectrograph at EvWaCo's star channel. The EXOplanet high-resolution SPECTrograph (EXOhSPEC) developed by our center is aligned beside this coronagraph (Lhospice et al., 2017). EXOhSPEC works in the visible band with a throughput of 4%. During our preliminary tests with the currently upgraded testbed, we used a multi-mode fiber instead of a single-mode fiber due to the lack of flux detected on EXOhSPEC. This is expected because the fiber used does not match the PSF core, and EvWaCo operates in the I-band. The first tests produced a noisy image and some stray light, as shown in Figure 7.3. The entire EvWaCo testbed is now enclosed in a black box to prevent stray light from contaminating the setup. Our future work on this testbed includes determining the appropriate size of the EvWaCo mask that allows enough photons for EXOhSPEC to achieve an SNR > 5.

In closing, EvWaCo's main capabilities, especially its achromaticity, offer an interesting area of investigation to the scientific community in response to the technological gaps in coronagraphy. I wonder how much the EvWaCo performance can be improved with state-of-the-art wavefront control and apodization techniques.

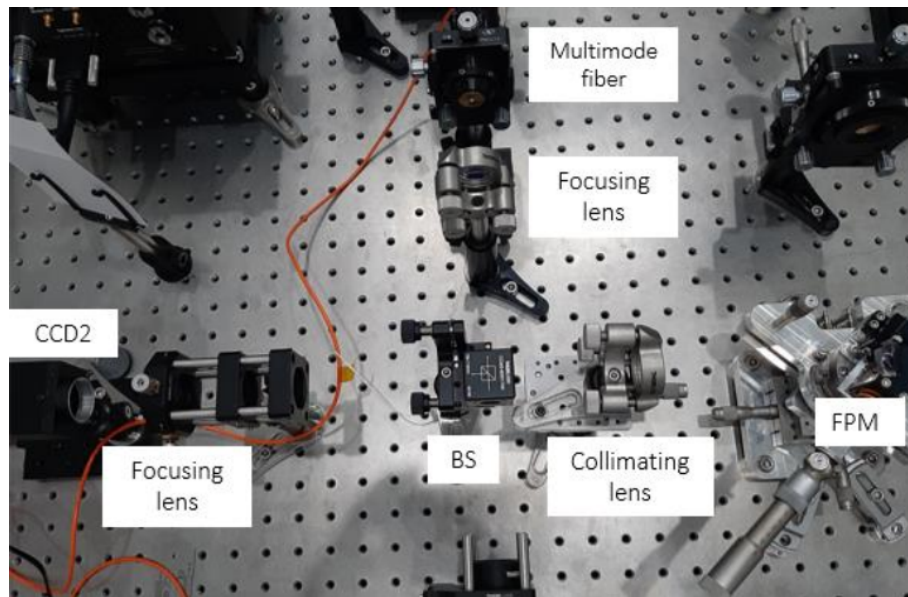


Figure 7.2: At the EvWaCo star channel, the transmitted light is split in half: one goes to the CCD to see the image of the star PSF, and another is reflected to a lens that focuses the light to a multi-mode fiber. This output end of this fiber serves as the light source for the EXOhSPEC.

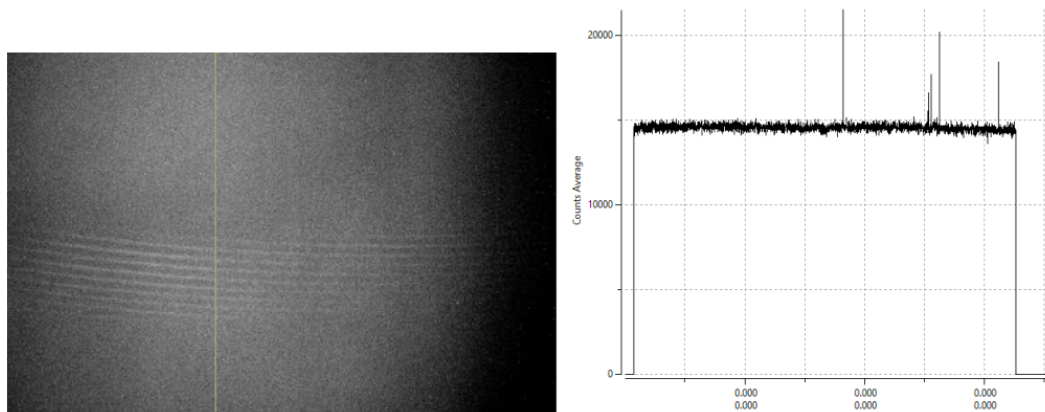


Figure 7.3: The first successful image, obtained at an exposure time of 60 s and an inner working angle $IWA_y \approx 3 \lambda/D$ over the full I-band. The figure on the right shows a cross-section of the image. The resulting image is noisy and shows some stray light.

Bibliography

- Aime, C. (2005). Principle of an Achromatic Prolate Apodized Lyot Coronagraph. *PASP*, 117.
- Alagao, M., Buisset, C., Kawinkij, K., Prasit, A., Lepine, T., Rabbia, Y., Berdeu, A., Thiebaut, E., Langlois, M., Tallon, M., Awiphan, S., Semenko, E., Rittipruk, P., Mkr-tichian, D., Poshyachinda, S., and Soonthornthum, B. (2021a). Design, performance, and potential scientific applications of the evanescent wave coronagraph with an adjustable inner working angle. *Proceedings International Conference on Space Optics*, 11852.
- Alagao, M., Buisset, C., Rabbia, Y., Lepine, T., Poshyachinda, S., and Soonthornthum, B. (2017). Development status and performance of the evanescent wave coronagraph testbed. In Shaklan, S., editor, *Techniques and Instrumentation for Detection of Exoplanets VIII*, volume 10400 of *Proc. SPIE*.
- Alagao, M., Kawinkij, K., Buisset, C., Prasit, A., Lepine, T., Rabbia, Y., Berdeu, A., Thiebaut, E., Langlois, M., Tallon, M., Awiphan, S., Semenko, E., Rittipruk, P., Mkr-tichian, D., Leckngam, A., Thuammasorn, G., Kaewsamoeta, P., Inpan, A., Kuha, T., Laoyang, A., Somboonchai, W., Kanthum, S., Poshyachinda, S., and Soonthornthum, B. (2021b). Deep contrast and companion detection using the EvWaCo testbed equipped with an achromatic focal plane mask and an adjustable inner working angle. *Astronomical Journal*, 161(5).
- Arenberg, J. and Harness, J. (2011). Solar Adaptive Optics. *Living Reviews in Solar Physics*, 8.
- Batalha, N. (2014). Exploring exoplanet populations with NASA's Kepler Mission. *PNAS*, 111:12647–12654.

- Berdeu, A., Sukpholtham, S., Kongkaew, P., Kawinkij, A., Ridsdill-Smith, M., Tallon, M., Thiebaut, E., Langlois, M., and Alagao, M. (2022). Adaptive Optics system of the Evanescent Wave Coronagraph (EvWaCo) – optimised phase plate and DM characterisation. In *Adaptive Optics VIII*, SPIE. International Society for Optics and Photonics.
- Bessel, M. (1990). UBVRI Passbands. *Publications of the Astronomical Society of the Pacific*, 102.
- Beuzit, J. L., Vigan, A., Mouillet, D., Dohlen, K., Gratton, R., and et al (2019). SPHERE: the exoplanet imager for the Very Large Telescope. *Astronomy & Astrophysics*, 631.
- Biller, B. and Bonnefoy, M. (2018). *Exoplanet Atmosphere Measurements from Direct Imaging*. Springer International Publishing.
- Born, M. and Wolf, E. (2002). *Principles of Optics*. Cambridge University Press, 7th edition.
- Bracewell, R. (1978). Detecting nonsolar planets by spinning infrared interferometer. *Nature*, 274:780–781.
- Budynas, R. and Nisbett, K. (2014). *Shigley's Mechanical Engineering*. McGraw Hill, 10th edition.
- Buisset, C., Rabbia, Y., Lepine, T., Alagao, M., Ducrot, E., Poshyachinda, S., and Soonthornthum, B. (2017). Study of a coronagraphic mask using evanescent waves. *Optics Express*, 25:7273–7287.
- Cash, W. (2006). Detection of Earth-like planets around nearby stars using a petal-shaped occulter. *Nature*, 442:51–53.
- Cash, W., Kasdin, J., Seager, S., and Arenberg, J. (2005). Direct studies of exo-planets with the New Worlds Observer. In *Techniques and Instrumentation for Detection of Exoplanets IV*, SPIE. International Society for Optics and Photonics.
- Chauvin, G., Lagrange, A.-M., Dumas, C., Zuckerman, B., Mouillet, D., Song, I., Beuzit, J.-L., and Lowrance, P. (2004). A giant planet candidate near a young brown dwarf:

- Direct VLT/NACO observations using IR wavefront sensing. *Astronomy and Astrophysics*, 425:29–32.
- Chauvin, G., Lagrange, A.-M., Dumas, C., Zuckerman, B., Mouillet, D., Song, I., Beuzit, J.-L., and Lowrance, P. (2005). Giant planet companion to 2MASSW J1207334-393254*. *Astronomy and Astrophysics*, 438:25–28.
- Crill, B. (2022). Progress in Technology for Exoplanet Missions 2022.
- Currie, T., Biller, B., Lagrange, A., Marois, C., Guyon, O., Nielsen, E., Bonnefoy, M., and De Rosa, R. (2022). Direct Imaging and Spectroscopy of Extrasolar Planets. *Review of the Direct Imaging field in Protostars and Planets VII*.
- Debes, J., Ge, J., Mandelowitz, C., and Watson, A. (2002). High-contrast imaging with Gaussian-shaped pupils. In *High-Contrast Imaging for Exo-planet Detection*, SPIE. International Society for Optics and Photonics.
- Encrenaz, T., Bibring, J., and Blanc, M. (2013). *The Solar System*. Springer Science & Business Media.
- Fischer, D., Howard, A., Laughlin, G., Macintosh, B., Mahadevan, S., Sahlmann, J., and Yee, J. (2014). *Exoplanet Detection Techniques*. The University of Arizona Press.
- Galicher, R. and Mazoyer, J. (2023). Imaging exoplanets with coronagraphic instruments. In *Exoplanets*.
- Gay, J. and Rabbia, Y. (1996). an interferometric method for coronagraphy. *Comptes Rendus de l'Academie des Sciences, Sér. II, Fasc. b,*, 322:265–271.
- Ge, J., Debes, J., Watson, A., and Chakraborty, A. (2004). Imaging Survey for faint companions with shaped pupil masks. In *Future Research Direction and Visions for Astronomy*, SPIE. International Society for Optics and Photonics, 4835.
- Goodman, J. (2005). *Introduction to Fourier Optics*. Roberts & Company, 3rd edition.
- Grady, C., Profitt, C., Malumuth, E., and et al (2003). Coronagraphic Imaging with the Hubble Space Telescope and the Space Telescope Imaging Spectrograph. *PASP*, 115.

- Gross, H. (2005). *Handbook of Optical Systems: Volume 1: Fundamentals of Technical Optics*. Wiley-VCH Verlag GmbH.
- Guerra, G., Daban, J., Robbe-Dubois, S., Douet, R., Abe, L., and et al (2011). Apodized Lyot Coronagraph for SPHERE/VLT: II. Laboratory tests and performance. *Experimental Astronomy*.
- Guyon, O. (2003). Phase-induced amplitude apodization of telescope pupils for extrasolar terrestrial planet imaging. *Astronomy & Astrophysics*, 404:379–387.
- Guyon, O. (2017). Habitable exoplanets detection: overview of challenges and current state-of-the-art. *Optics Express*, 25(23):2885–28837.
- Guyon, O. (2018). Extreme Adaptive Optics. *Annual Review of Astronomy and Astrophysics*, 56:315–355.
- Guyon, O., Pluzhnik, E., Kuchner, M., Collins, B., and Ridgway, S. (2006). Theoretical Limits on Extrasolar Terrestrial Planet Detection with Coronagraphs. *APJ*, 167(81).
- Hecht, E. (2017). *Optics Fifth Edition*. Pearson Education Limited.
- Howell, S., Sobeck, C., Haas, M., Still, M., Barclay, T., and et al (2014). The K2 Mission: Characterization and Early Results. *PASP*, 126(398).
- Jovanovic, N., Martinache, F., Guyon, O., Clergeon, C., Singh, G., and et al (2015). The Subaru Coronagraphic Extreme Adaptive Optics Systems: Enabling High-Contrast Imaging on Solar-System Scales. *PASP*, 127:890–910.
- Kasdin, J., Vanderbei, R., and Littman, M. (2003). Extrasolar Planet Finding via Optimal Apodized-Pupil and Shaped-Pupil Coronagraphs. *APJ*, 528.
- Kasdin, J., Vanderbei, R., Littman, M., and Spergel, D. (2005). Extrasolar Planet Finding via Optimal Apodized-Pupil and Shaped-Pupil Coronagraphs. *Applied Optics*, 44.
- Kasting, J., Traub, W., Leger, A., Wooten, A., and et al (2010). Exoplanet Characterization and the Search for Life. In *astro2010: The Astronomy and Astrophysics Decadal Survey*.

- Kuchner, M. and Traub, W. (2002). A coronagraph with a band-limited mask for finding terrestrial planets. *APJ*, 570:900–908.
- Lagarias, J., Reeds, J. A., Wright, M., and Wright, P. (1998). Convergence Properties of the Nelder–Mead Simplex Method in Low Dimensions. *SIAM Journal on Optimization*, 9.
- Lagrange, A., Gratadour, D., Chauvin, G., Fusco, T., Ehrenreich, D., Mouillet, D., and et al (2008). A probable giant planet imaged in the β Pictoris disk. *Astronomy and Astrophysics*, 493:21–25.
- Leger, A., Mariotti, J., Mennesson, B., Ollivier, M., Puget, J. L., Rouan, D., and Schneider, J. (1996). Could We Search for Primitive Life on Extrasolar Planets in the Near Future? *Icarus*, 123:249–255.
- Lhospice, E., Buisset, C., Jones, H., Martin, W., Errmann, R., Sithajan, S., Boonsri, C., and et al (2017). EXOhSPEC folded design optimization and performance optimization. volume 153.
- Liot, B. (1939). A Study of the Solar Corona and Prominences Without Eclipses. *MNRAS*, 99:538.
- Macintosh, B., Graham, J., Ingraham, P., Konopacky, Q., Marois, C., and et al (2014). First light of the Gemini Planet Imager. *PNAS*, 111:12661–12666.
- Macintosh, B., Graham, J. R., and Barman, T. (2015). Discovery and Spectroscopy of the Young Jovian Planet 51 Eri b with the Gemini Planet Imager. *Science*, 350:64–67.
- Marois, C., Macintosh, B., Barman, T., Zuckerman, B., Song, I., Patience, J., Lafreniere, D., and Doyon, R. (2008). Direct Imaging of Multiple Planets Orbiting the Star HR 8799. *Science*, 322:1348–1352.
- Marois, C., Zuckerman, B., Konopacky, Q., Macintosh, B., and Barman, T. (2010). Images of a fourth planet orbiting HR 8799. *Nature*, 468:1080–1083.
- Mawet, D., Pueyo, L., Lawson, P., and et al (2012). Review of small-angle coronagraphic techniques in the wake of ground-based second-generation adaptive optics

- systems. In *Space Telescopes and Instrumentation: Optical, Infrared, and Millimeter Wave*, 844204, SPIE. International Society for Optics and Photonics.
- Mawet, D., Riaud, P., Baudrand, J., Baudoz, P., Boccaletti, A., and et al (2006). The four-quadrant phase-mask coronagraph white light laboratory results with an achromatic device. *Astronomy & Astrophysics*, 448(2).
- Mawet, D., Ruane, G., Xuan, W., Echeverri, D., Klimovich, N., and et al (2017). Observing Exoplanets with High Dispersion Coronagraphy. II. Demonstration of an Active Single-Mode Fiber Injection Unit. *ApJ*, 838(2).
- Mawet, D., Serabyn, E., Liewer, K., Buruss, R., Hickey, J., and Shemo, D. (2010). The vector vortex coronagraph: Laboratory results and first light at Palomar Observatory. *ApJ*, 709:53–57.
- Mayor, M. and Queloz, D. (1995). A Jupiter-mass companion to a solar-type star. *Nature*, 378:355–359.
- Morley, C., Fortney, J., Marley, M., Zahnle, K., and et al (2015). Thermal Emission and Albedo Spectra of Super Earths with Flat Transmission Spectra. *APJ*, 815.
- Morris, E., Wang, J., Ruffio, J., Delorme, J., Pezzato, J., and et al (2020). The Keck Planet Imager and Characterizer: Phase 1 fiber injection unit early performance and commissioning. In *Ground-based and Airborne Instrumentation for Astronomy VIII*, volume 11447 of *Proc. SPIE*.
- Mouillet, D., Lagrange, A., Augereau, J., and Menard, F. (2001). Asymmetries in the HD 141569 circumstellar disk. *Astronomy & Astrophysics*, 372.
- Nemati, B., Stahl, P., Stahl, M., Ruane, G., and Sheldon, L. (2020). Method for deriving optical telescope performance specifications for Earth-detecting coronagraphs. *Journal of Astronomical Telescopes, Instruments, and Systems*, 6.
- Powell, M. (2006). *The NEWUOA software for unconstrained optimization without derivatives*. Springer.

- Rabbia, Y. (2003). Shared constraints and specific characters in Very High Dynamics Imaging. In Aime, C. and Soummer, R., editors, *EAS Publications Series*, volume 8 of *Proceedings in Astronomy with High Contrast Imaging*, pages 65–78.
- Riaud, P. and Schneider, J. (2015). Improving Earth-like planets detection with an ELT: the differential radial velocity experiment. *Astronomy & Astrophysics*, 576:56–59.
- Ricker, G., Winn, J., Vanderspek, R., Latham, D., Bakos, G., and et al (2015). The Transiting Exoplanet Survey Satellite. *JATIS*, 1.
- Ridsdill-Smith, M., Berdeu, A., Alagao, M., Buisset, C., and Awiphan, S. (2023). The Scientific Capabilities of the Evanescent Wave Coronagraph. In *Journal of Physica: Conference Series*, volume 2431 of *Siam Physics Congress*.
- Roddier, F. and Roddier, C. (1997). Stellar Coronagraph with a Phase Mask. *PASP*, 109.
- Rouan, D., Riaud, D., Boccaletti, A., Clenet, Y., and Labeyrie, A. (2000a). The Four-Quadrant Phase-Mask Coronagraph. I. Principle. *Publications of the Astronomical Society of the Pacific*, 112.
- Rouan, D., Riaud, P., Boccaletti, A., Clenet, Y., and Labeyrie, A. (2000b). The Four-Quadrant Phase-Mask Coronagraph. *PASP*, 112.
- Ruane, G., Riggs, A., Mazoyer, J., Por, E. H., N’Diaye, M., Huby, E., and et al (2018). Review of high-contrast imaging systems for current and future ground- and space-based telescopes I. Coronagraph design methods and optical performance metrics. In M. Lystrup and H. MacEwen and G. Fazio and N. Batalha and N. Siegler and E. Tong, editor, *Space Telescopes and Instrumentation 2018: Optical, Infrared and Millimeter Wave*, volume 10698 of *Proc. SPIE*.
- Seager, S. (2010). *Exoplanets*. The University of Arizona Press.
- Shao, M., Levine, B., Wallace, J., Orton, G., Schmidlin, E., and et al (2006). A Nulling Coronagraph for TPF-C. In *Ground-based and Airborne Instrumentation for Astronomy VIII*, volume 6265 of *Proc. SPIE*.

- Sivaramakrishnan, A., Koresko, C., Makidon, R., Berkefeld, T., and Kuchner, M. (2001). Ground-based Coronagraphy with High-Order Adaptive Optics. *APJ*, 552:397–408.
- Slepian, D. (1965). Analytic Solution Two Apodization Problems. *Journal of the Optical Society of America*, 55:1110–1115.
- Snellen, I., Snik, F., Kenworthy, M., and et al (2015). Discovery and Spectroscopy of the Young Jovian Planet 51 Eri b with the Gemini Planet Imager. *Science*, 350:64–67.
- Soummer, D. (2005). Apodized Pupil Lyot Coronagraphs for Arbitrary Telescope Apertures. *ApJ*, 618(2).
- Soummer, R., Sivaramakrishnan, A., Oppenheimer, B., and et al (2009). The Gemini Planet Imager coronagraph testbed. In *Future Research Direction and Visions for Astronomy*, SPIE. International Society for Optics and Photonics, 4835.
- Spergel, D. (2001). A New Pupil for Detecting Extrasolar Planets. *Applied Optics*.
- Traub, W. and Oppenheimer, B. (2010). *Direct Imaging of Exoplanets*. The University of Arizona Press.
- Vigan, A., Gry, C., Salter, G., Mesa, D., Homeier, C., and Allard, F. (2015). High-contrast imaging of Sirius A with VLT/SPHERE: Looking for giant planets down to one astronomical unit. *MNRAS*, 000:1–16.
- Wang, J., Mawet, D., Ruane, G., Hu, R., and Benneke, B. (2017). Observing Exoplanets with High Dispersion Coronagraphy. I. The Scientific Potential of Current and Next-Generation Large Ground and Space Telescopes. *ApJ*, 153(4).
- Zhu, S., Yu, A., Hawley, D., and Roy, R. (1986). Frustrated total internal reflection: A demonstration and review. *American Journal of Physics*, 54.

Appendix A

Aligning the EvWaCo

A.1 Aligning an EvWaCo setup

There are two imaging modes in the testbed. One is dedicated to imaging the PSF to measure the raw contrast of the system and another one is for the pupil image to ensure the alignment of the aperture stop and the Lyot stop. It is important to easily access these modes to properly align the coronagraph testbed. Figure A.1 shows a simplified diagram of the location of the optical components in PSF imaging mode. Outlined below is the procedure to align the PSF imaging mode from scratch.

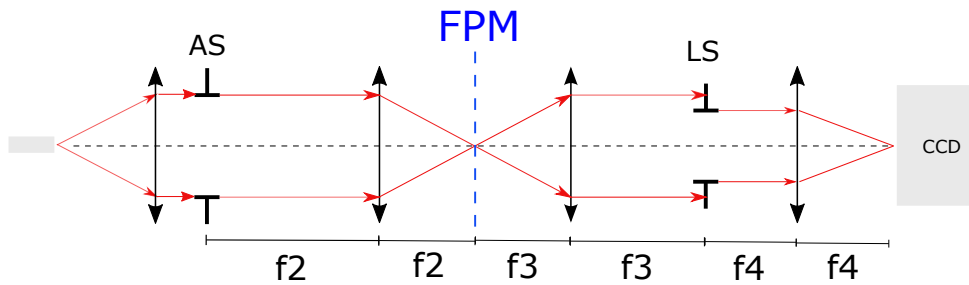


Figure A.1: Schematic diagram of the PSF imaging mode.

1. The laser source serves as a reference and is aligned such that the height of the beam remains consistent throughout the intended space. At the minimum, the distance covered is until the position of the focal plane mask. Usually, the determining factor for the optical height is the center of the science camera, including its mount on the testbed.



Figure A.2: Reference setting using the laser.

2. Place the focal plane mask at the optical path. Roughly position the mask such that the beam passes through the center of the prism. Slightly place the lens and the prism in

contact. Put just enough pressure on the mask to observe the transmitted beam. Use the micrometers on the focal plane mask to finely position the mask such that the laser beam passes through the hole.



Figure A.3: The laser beam must pass through the hole of the FPM mask.

3. Place a flat mirror in front of the FPM and adjust the tilt such that the beam reflects back to the laser. Install the aperture stop at twice the focal length of the lens L2. Use a 1 mm diameter pinhole and adjust the lateral position of the aperture stop to make sure that the beam passes through its center.

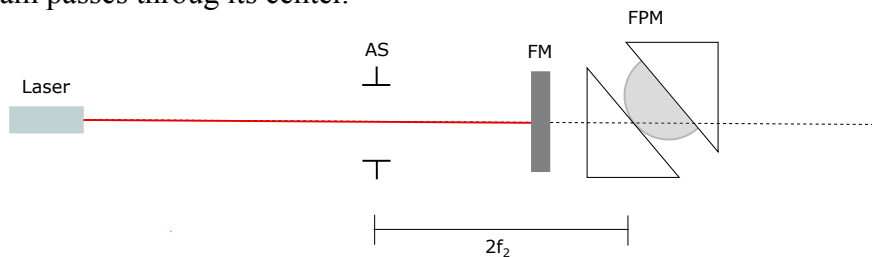


Figure A.4: If the beam is properly centered, the shape of the beam transmitted through the aperture stop must also be circular.

4. Place the achromatic doublet lens L1 in the optical path and ensure the orientation is correct. The lens must be properly centered, and check that the lens face is perpendicular to the optical axis (no tilt). Install the optical fiber at one focal length before the lens L1. Due to the presence of the flat mirror, a focused spot can also be observed at the face of the entrance fiber. Adjust the XY position of the optical fiber to center this focused spot on the entrance fiber. The alignment is correct if the beam after L1 is properly collimated: the size of the beam remains consistent along the optical axis, and the circular area is uniformly illuminated.

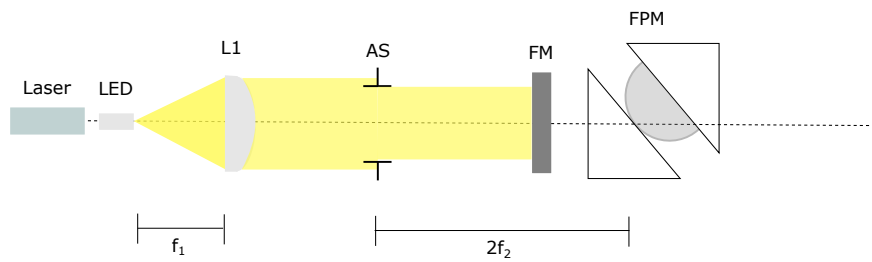


Figure A.5: The beam passing through the lens L1 must be collimated: uniformly illuminated and consistent size along the optical path

5. Place the achromatic doublet lens L2 in the optical path and follow the correct orientation as shown in the diagram below. Follow the same lens positioning procedure as L1. Adjust the position of the lens along the optical axis to ensure that the beam's size at the prism's entrance face and exit face are roughly the same. During this procedure, remove the contact between the lens and the prism.

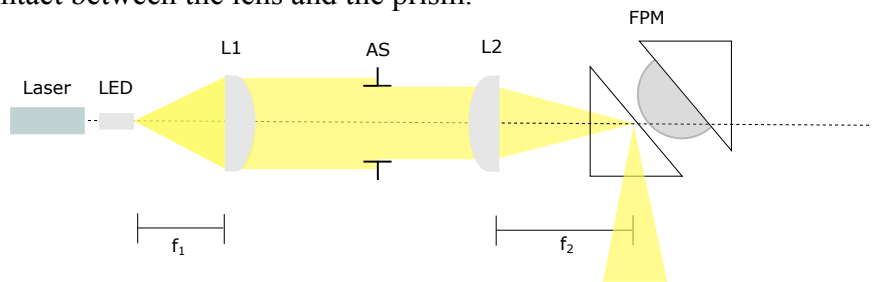


Figure A.6: The beam passing through the lens L1 must be collimated: uniformly illuminated and consistent size along the optical path

6. Temporarily remove the aperture stop but keep its adapter in place to avoid distorting its alignment. Place a detector at the reflected arm of the FPM. Orient the FPM until the dark area is close to the edge. This dark area corresponds to the bundle of rays with angles of incidence greater than the critical angle. This procedure is only when the angle of incidence is approximately 42° .

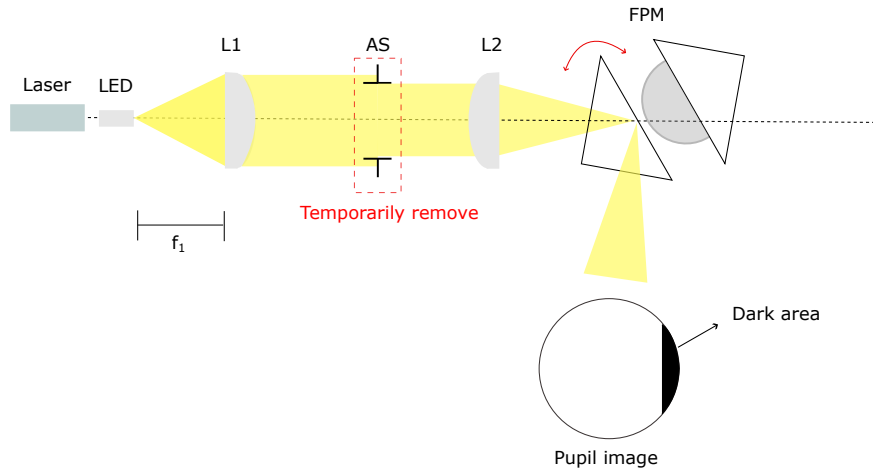


Figure A.7: Adjust the orientation of the FPM so that the angle of incidence is approximately 42° .

7. Install the achromatic doublet lens L3. Adjust its position along the optical axis until a collimated beam is observed.

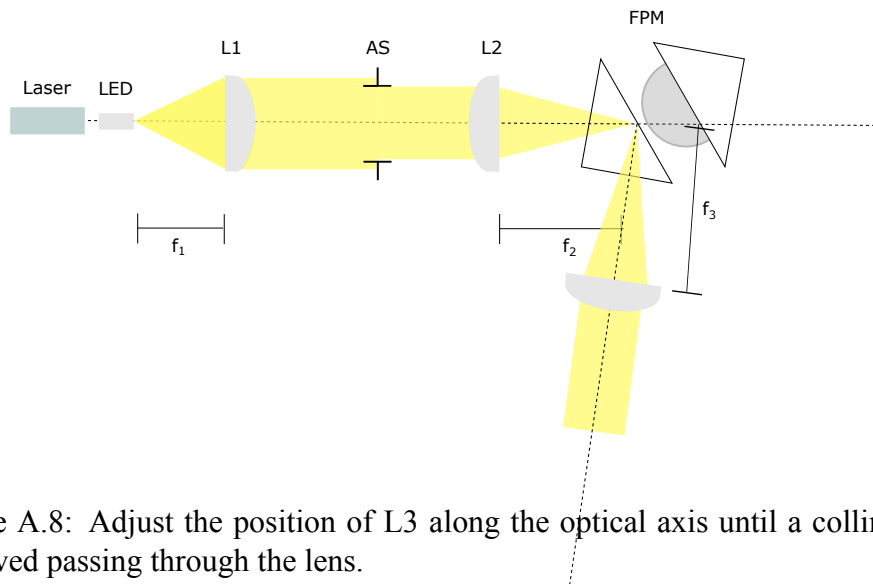


Figure A.8: Adjust the position of L3 along the optical axis until a collimated beam is observed passing through the lens.

8. Install the Lyot stop after the lens L3. Place it at roughly a distance of f_3 from the lens. The Lyot stop is circular and smaller than the aperture stop. The beam must pass through the center of the Lyot stop. For alignment purposes, replace the Lyot stop first with a 1-mm diameter pinhole to properly center the beam. Remove the small pinhole after securing the alignment.

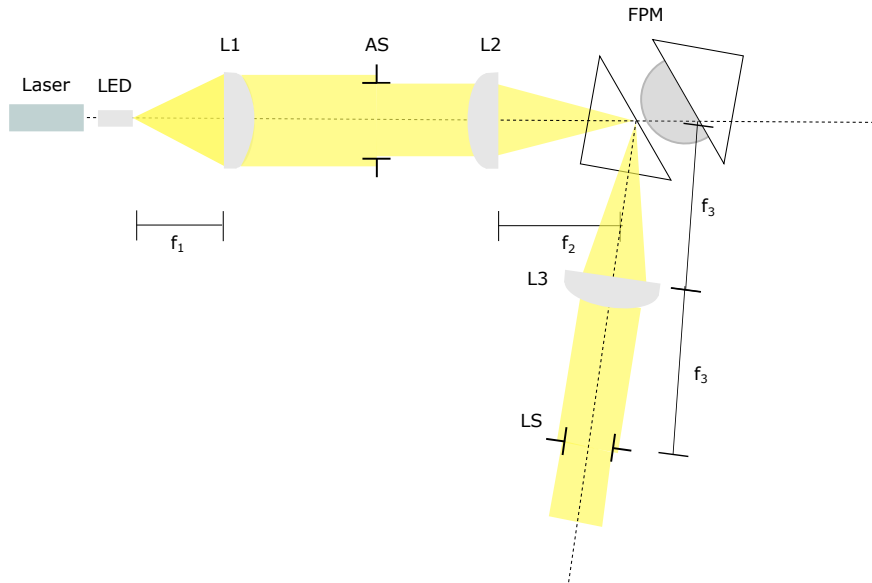


Figure A.9: The position of the Lyot stop must be at f_3 after L3.

9. Place the lens L4 at a distance f_4 from the Lyot stop. Then, place the detector at the focal plane of L4. Make sure that the optical fiber you are using has a core diameter no greater than $50\mu\text{m}$.

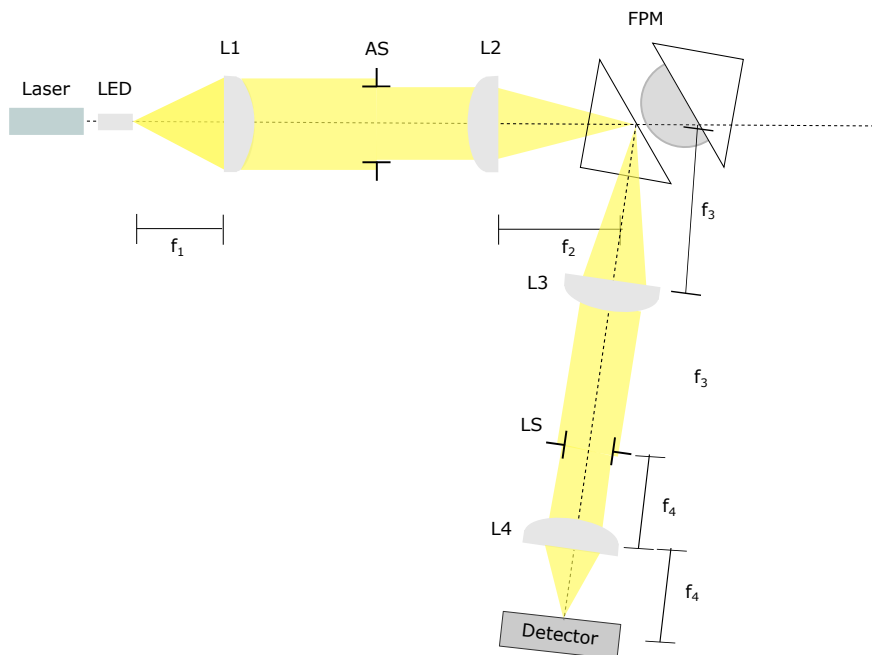


Figure A.10: Adjust the position of the detector along the optical axis to obtain a sharp image of the focused spot.

10. Place the lens L4 at a distance f_4 from the Lyot stop. Then, place the detector at the focal plane of L4. Make sure that the optical fiber you are using has a core diameter no greater than $50\mu\text{m}$.

After getting an acceptable PSF, aligning the pupil imaging path comes next, as shown in Figure A.11.

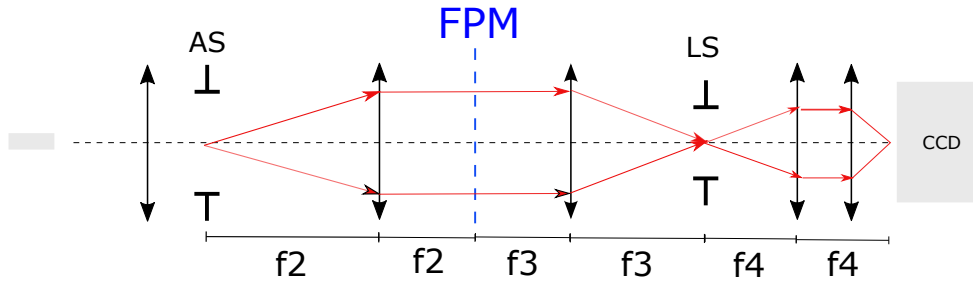


Figure A.11: Schematic diagram of the pupil imaging mode.

Remove the AS mask and replace it with an optical fiber that serves as the source. Place temporarily the pinhole in front of the mask to reduce the size of the collimated beam going into the FPM.

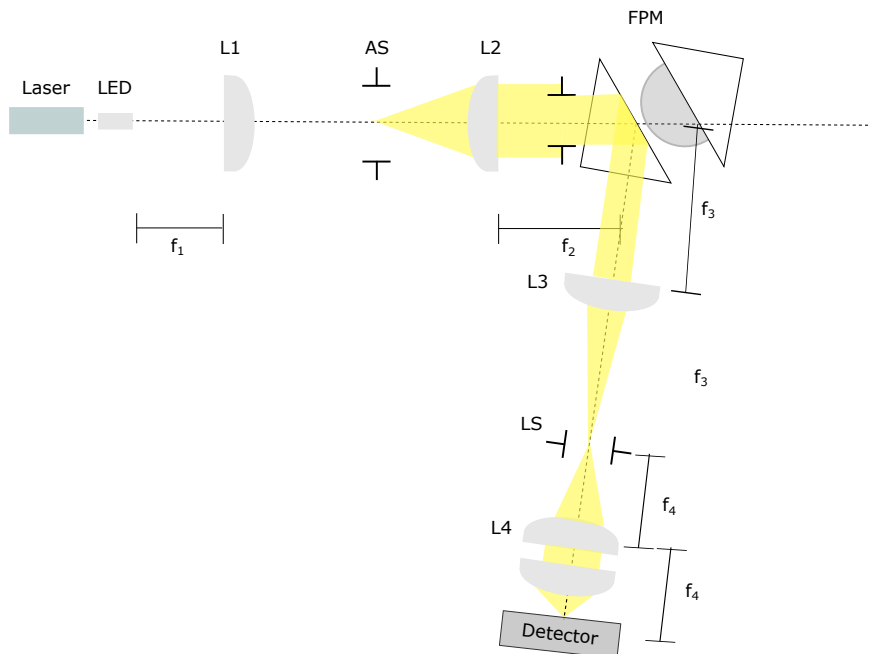


Figure A.12: Check the proper location of the LS by placing an optical fiber at the location of the aperture stop.

Appendix B

Data Acquisition Procedure

The experiment uses three PSF images to determine the normalized irradiance: unsaturated off-axis PSF, saturated off-axis PSF, and on-axis PSF. The first two sets of off-axis PSF images, $PSF_{coro}(x, x_o, \lambda)$, are both set at $x_o \approx 7\lambda/D$, where the mask transmission is equal to 1. The unsaturated off-axis PSF is obtained after installing an optical density OD2 in front of the detector with the following transmission on each bandpass: $t_{I-band} = 2.10^{-3}$ and $t_{R-band} = 1.3.10^{-3}$. The integration time, τ , for this PSF image is chosen so that the peak of the star PSF is close to the maximum dynamic range of the camera and recorded $N = 101$ frames of the same integration time. Then, eleven dark images and eleven bias images at an integration time equal the integration time set and 0 s, respectively. The master bias frame was calculated from the median of the eleven bias images while the master dark frame was calculated from the median of the eleven dark images, each subtracted from the master bias frame. Finally, for each single frame of the off-axis PSF, the master bias and master dark frame were subtracted. Then, the median of the unsaturated PSF off-axis is measured, and the image peak value, $S_{Star,peak}$, is determined from this frame.

The OD2 was uninstalled from the optical path when measuring the saturated off-axis PSF, $S_{Star}(x,y)$. All the observing conditions and pre-processing methods are followed as in the first PSF. This will result in a PSF saturated with a high signal-to-noise ratio in the PSF wings.

Finally, the on-axis PSF, $PSF_{coro}(x, 0, \lambda)$, is measured by centering the PSF on the occulting mask and recording the signal $S_{Residual}(x,y)$ at the same integration time. The resulting normalized irradiance is calculated using Equation B.1.

$$I_{norm}(x_o, \lambda) = \frac{S_{Residual} T_{OD2}}{S_{Star, Peak}} \quad (\text{B.1})$$

To calculate the raw contrast, the normalized irradiance, I_{norm} , is divided by the mask transmission obtained from the experiment. For example, from Figure 10, at $3 \lambda/D$, the normalized irradiance is approximately at $I_{norm} \approx 1.10^{-4}$ in the I-band. Thus, the corresponding raw contrast at this location equals 2.10^{-4} .

Appendix C

Numerical Modelling in Broadband Light

The numerical model in EvWaCo uses the Fourier transform to compute the electric field amplitude at the image planes, given the characteristics of the pupil planes.

This model takes the following inputs:

- Spectral flux incident on the detector
- Air Gap profile
- Diameters of the aperture stop and the Lyot
- Focal lengths of the lenses
- Angle of incidence

There are four important planes: the entrance pupil (aperture stop), the focal plane, the exit pupil plane, and the detector plane.

For each wavelength, the procedure is as follows:

- 1) Indicate the properties of the entrance pupil $P_1(\xi, \eta)$, where ξ and η represent the coordinates of the pupil plane, expressed in meters. The entrance pupil plane may be circular or elliptical, with or without Gaussian apodization, with Central obscuration (with four spider vanes or not).
- 2) Take the Fourier transform of the entrance pupil denoted by $F_2(x, y)$, where the coordinates (x,y) are spatial frequencies given by $x = \xi/\lambda f$ and $y = \eta/\lambda f$ with f as the focal length of the focusing lens.

- 3) Multiply the amplitude at the focal plane by the mask transmission $M(x,y)$: $F_{2+} = M(x,y) \times F_2(x,y)$, where $M(x,y)$ is the reflection coefficient given by the expression:

$$r_{13} = \frac{r_{12} + r_{23}e^{-2\delta'}}{1 + r_{12}r_{23}e^{-2\delta'}}, \quad (\text{C.1})$$

where

$$\delta' = \frac{2\pi}{\lambda}d \left[n_1^2 \sin^2 \theta_i - 1 \right]^{\frac{1}{2}}. \quad (\text{C.2})$$

Note: From this point, the electric field amplitude is calculated and propagated per polarization.

- 4) Take the Fourier transform of F_{2+} to calculate the electric field at the exit pupil, $P_2(\xi, \eta)$
- 5) Multiply it by the transmission of the Lyot stop, $T_{LS}(\xi, \eta)$ such that the electric field after the exit pupil is given by: $P_{2+}(\xi, \eta) = P_2(\xi, \eta) \times T_{LS}(\xi, \eta)$.
- 6) The electric field at the detector plane takes the Fourier transform of $P_{2+}(\xi, \eta)$.

The intensities calculated per wavelength at the detector plane are added when considering the numerical modeling in polychromatic (broadband) light. Since the sampling at the focal plane depends on the wavelength, the size of the grid at the image planes is interpolated so that the size of the grid at the focal planes of the broadband model assumes that of the size for the longest wavelength.

CURRICULUM VITAE

Full Name Mary Angelie Alagao

Date of Birth November 9, 1991

Education 2016 Master in Physics - University of the Philippines-Diliman

2013 Bachelor in Applied Physics (Instrumentation) - University of the Philippines-Diliman

2008 Sacred Heart College Tacloban City

Publications

- 1) M.A. Alagao, A. Kawinkij,, C. Buisset, A. Prasit, T. Lepine, Y. Rabbia, et. al., “Deep contrast and companion detection using the EvWaCo testbed equipped with an achromatic focal plane mask and an adjustable inner working angle,” *Astronomical Journal, Volume 161, Number 208*, March 2021, doi:10.3847/1538-3881/abe709
- 2) Buisset, C., Rabbia, Y., Lepine, T., Alagao, M.A., Ducrot, E., Poshyachinda, S., Soonthornthum, B., Study of a coronagraphic mask using evanescent waves, *Optics Express*, pp. 7273-7287, March 2017

Conference Proceedings

- 1) Kawinkij, A., Buisset, C., Prasit, A., Alagao, M.A., et al., “EvWaCo Prototype Athermal Mechanical Design”, Proceedings Volume 12188, *Advances in Optical Mechanical Technologies for Telescopes and Instrumentation*, 2022.
- 2) Ridsdill-Smith M., Berdeu, A., Alagao, M.A., Buisset, C., Awiphan, S, “The scientific capabilities of the Evanescent Wave Coronagraph” (2023), *Journal of Physics: Conference Series*, Volume 2431, Issue 1, id.012098, 9 pp.
- 3) Berdeu, A., Sukpholtham, S., Kongkaew, P., Kawinkij, A., Ridsdill-Smith, M., Tallon, M., Thiébaud, E., Langlois, M., Alagao, M. A. (2022). Adaptive Optics system of the Evanescent Wave Coronagraph (EvWaCo): optimised phase plate and DM characterization, *daptive Optics Systems VIII*, Proc. SPIE 12185 (2022).
- 4) Berdeu, A., Tallon, M., Thiebaut, E., Alagao, M.A., et. al. (2022). Inverse problem approach in Extreme Adaptive Optics: analytical model of the fitting error and lowering of the aliasing, *daptive Optics Systems VIII*, Proc. SPIE 12185 (2022).
- 5) M.A. Alagao, C. Buisset, A. Kawinkij, A. Prasit, T. Lepine, Y. Rabbia, et. al. “Design, performance and scientific applications of the Evanescent Wave Coronagraph with an adjustable inner working angle” *International Conference on Space Optics, Proceedings SPIE*, 11852, 2021. <https://doi.org/10.1117/12.2599626>
- 6) Buisset, C., Lepine, T., Thiebaut, E., Langlois, M., Tallon, M., Alagao, M.A., Tallon-Bosc, I., Rabbia, Y., Poshyachinda, S., and Soonthornthum, B., Ducrot, E., “The evanescent wave coronagraph project: setup results and demonstrator preliminary design,” *Advances in Optical and Mechanical Technologies for Telescopes and Instrumentation III*, Proc. SPIE 2018.
- 7) Alagao, M.A., Buisset, C., Rabbia, Y., Lepine, T., Poshyachinda, S., Soonthornthum, B., Development status and performance of the evanescent wave coronagraph testbed,

Techniques and Instrumentations for Detection of Exoplanets VIII, *SPIE Optical Engineering and Applications*, San Diego, August 2017. (Poster Presenter)

8) Alagao, M.A., Go, M.A., Soriano, M., Tapang, G., Improving the Point Spread Function of an Aberrated 7-Mirror Segmented Reflecting Telescope, *4th International Conference on Optics, Photonics and Laser Technology (PHOTOPTICS)*, Rome, Italy, February 27-29, 2016. (Oral Presenter)

9) Alagao, M. A., Tapang, G., Effective Diameter of an $N + 1$ -Mirror Segmented Telescope, *4th Southeast Asian Young Astronomers Meeting*, Krabi, Thailand, December 3-4, 2015. (Oral Presenter)

10) Mascarinas, N. D.F., Alagao, M. A., Tapang, G., Low-cost spectrometer using light emitting diode array, *Samahang Pisika ng Pilipinas Conference Proceedings* (2015).

11) Alagao, M. A., Tapang, G., Simulation of Theoretical Light Curves During an Asteroid Occultation, *Samahang Pisika ng Pilipinas Conference Proceedings* (2015).

12) Alagao, M.A., Bruzon, D.A., Martinez-Su, I., Tapang, G., LED-based Spectrometer for Advanced Chemistry Laboratory Experiments, *ASEAN Conference on Science and Technology*, Bogor, Indonesia, August 18-20, 2014. (Oral Presenter)

13) Alagao, M.A, Cabangon, R.J., Tapang, G., Construction of the Calibration Curve for Sugar Concentration Determination using an LED-based Spectrometer, *Samahang Pisika ng Pilipinas Conference Proceedings* (2014).

14) Alagao, M. A., Soriano, M., Netbook-based Distortion Product Otoacoustic Emission Detector, *Samahang Pisika ng Pilipinas Conference Proceedings* (2011).